Title
RESONANT PRODUCTION IN TWO PHOTON COLLISIONS

Author
Butter, Frederick

Publication Date
1988-12-01

LBL-26465

Lawrence Berkeley Laboratory
UNIVERSITY OF CALIFORNIA

Physics Division

Resonant Production in Two Photon Collisions

F. Butler
(Ph.D. Thesis)

December 1988

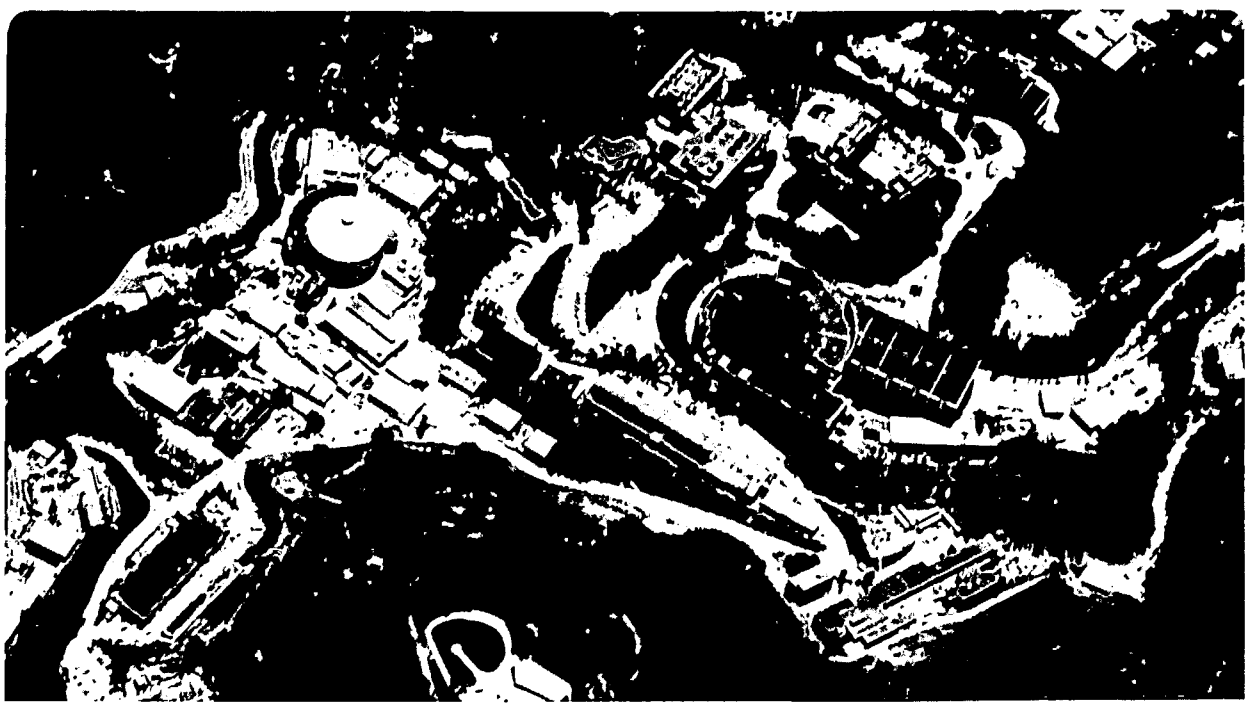

Prepared for the U.S. Department of Energy under Contract Number DE-AC03-76SF00098.

DISCLAIMER

RESONANT PRODUCTION IN TWO PHOTON COLLISIONS

Frederick Butler
(Ph.D. Thesis)

Department of Physics
University of California
and
Physics Division
Lawrence Berkeley Laboratory
1 Cyclotron Road
Berkeley, California 94720

December 1988

This work was supported by the Director, Office of Energy Research, Office of High Energy and Nuclear Physics, Division of High Energy Physics of the U.S. Department of Energy under Contract Number DE-AC03-76SF00098.

RESONANT PRODUCTION IN TWO PHOTON COLLISIONS

Frederick Butler

Abstract

Using 220 $picobarn^{-1}$ of data collected by the Mark II detector at PEP,we have measured the width of the η' for quasi real photons. The width is separately measured in the three reactions $e^+e^- \to e^+e^-\eta^0\pi^+\pi^-;\eta^0 \to \gamma\gamma$, $e^+e^- \to e^+e^-\eta^0\pi^+\pi^-;\eta^0 \to \pi^+\pi^-(\pi^0,\gamma)$ and $e^+e^- \to e^+e^-\rho^0\gamma$, giving a statistically weighted average two-photon width of $\Gamma_{\eta'\to\gamma\gamma} = 5.21\pm0.28$ keV. As a by-product of the measurement of $\Gamma_{\eta'\to\gamma\gamma}$ using the decay mode $\eta' \to \rho\gamma$, we also measured a two-photon decay width for the $a_2(1320)$ of $\Gamma_{a_2(1320)\to\gamma\gamma} = 1.17 \pm0.15 \pm0.25$ keV .

Table of Contents

Chapter 1. Introduction

Two-photon interactions provide a valuable experimental probe of the structure of elementary particles. The Mark II experiment at the PEP storage ring was used primarily to study produced particle states in e^+e^- annihilation. Figure 1.1 shows the lowest order Feynman diagram for production by e^+e^- annihilation. Since all states produced are coupled to a single time like virtual photon the states must have a charge conjugation quantum number of C=-1. The electromagnetic coupling conserves the charge conjugation quantum number of the virtual photon. The two-photon interactions involves the coupling of 2 virtual photons to a final state and so must produce C= (-1)(-1)=+1 charge conjugation states. (See Figure 1.2) The two-photon production mechanism complements the annihilation production mechanism for resonance formation. Two-photon production has the added advantage, that the states produced need not have the total beam energy, since most of the energy is carried away by the outgoing scattered beam electrons. If one or both of the outgoing beam electrons is detected, additional information is available about the two-photon interaction kinematics. To efficiently form a resonance state by annihilation the beam energy must be adjusted to be near the desired resonance's mass.

The two-photon production cross sections arising from the diagram in Figure 1.2 increase with beam energy like $(\log E/m_e)^2$, while the annihilation cross sections of Figure 1.1 decrease by $\frac{1}{E^2}$. In fact the two-photon cross sections become larger than the annihilation cross sections at beam energies of a few GeV. The energy in the $\gamma\gamma$ center of mass typically remains small however.

In this thesis we will be measuring the two photon partial widths of the η' and $a_2(1320)$ hadrons. The two-photon width we measure will tell us something about the quark content of the η' and $a_2(1320)$.

The coupling of two photons to a meson is diagrammed in Figure 1.3 . The coupling diagram is of order α^4 so that the strength of the coupling is proportional

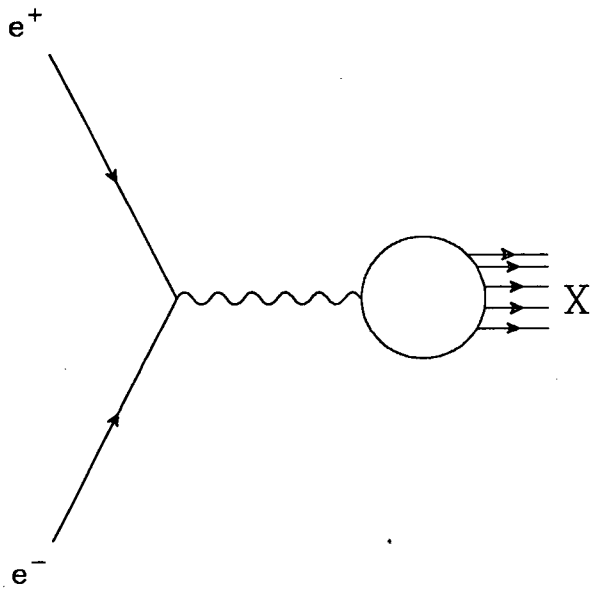

Figure 1.1 *Production of a final state X by e^+e^- annihilation*

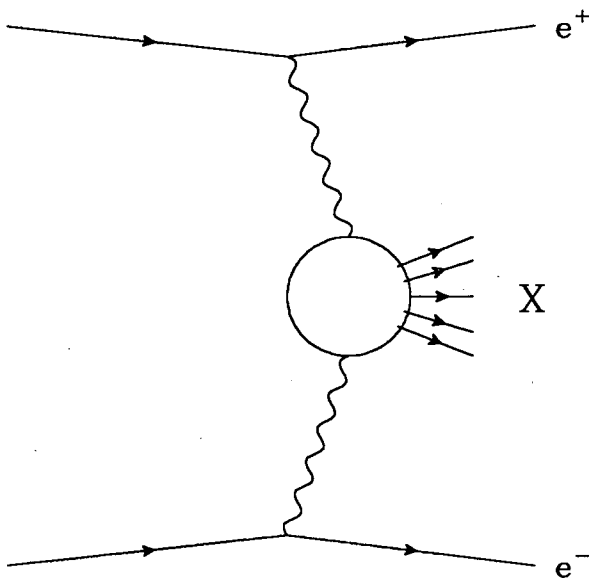

Figure 1.2 *Production of a final state X by two photons*

to the square of the quark charge and the production cross section is proportional to the 4th power of the quark charges. If we assume that the meson is a coherent mixture of quark-antiquark pairs, the size of the coupling is very sensitive to the quark charge, and therefore very sensitive to the mixture of quark flavors. The meson

may be decomposed as the sum of quark anti-quark bound states as:

$$|Meson>=\sum_q c_q|q\bar{q}> \tag{1.1}$$

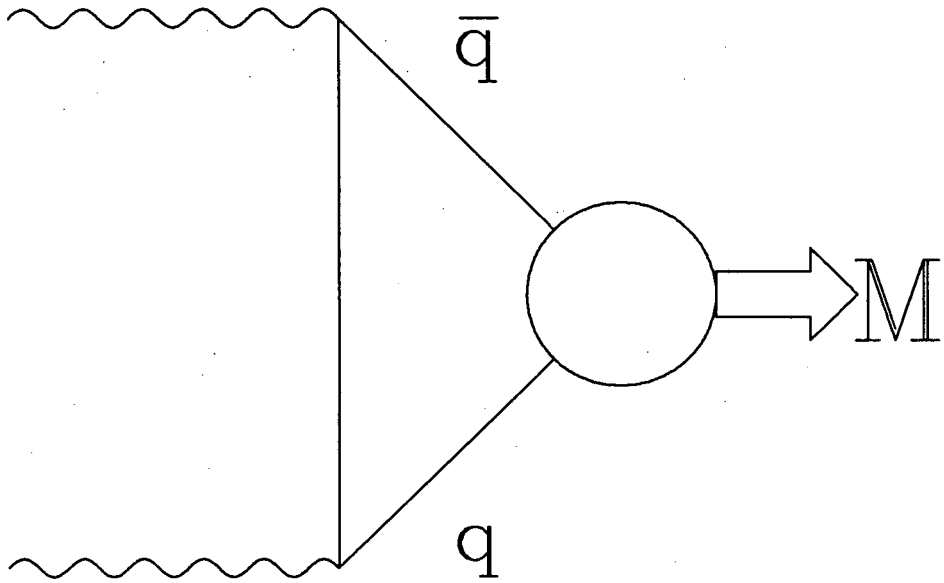

Figure 1.3 *The coupling of two photons to a meson*

Meson states have been grouped together into families with the same spin and parity J^P. The η' was placed into a nonet of pseudo scalars. The bound states of quark-antiquark pairs are assigned to locations in the octet and singlet representations of the $SU(3)$ flavor symmetry group. The $SU(3)$ symmetry group is thought to approximately describe the bound state dynamics of u, d, and s quark combinations.

$$3 \otimes \bar{3} \rightarrow 8 \oplus 1 \tag{1.2}$$

If the quark radial wave function at the origin is independent of the quark flavor the two-photon coupling constant ($g_{M_{\gamma\gamma}}$) for Meson (M) can be found as the expectation value of the quark charges squared.

$$g_{M_{\gamma\gamma}} \sim < M|\gamma\gamma > \sim \sum_q c_q \cdot e_q^2 = < e_q^2 > \tag{1.3}$$

Making particle assignments based only on the SU(3) group generators we would have the assignments given in Table 1.1 . Since the SU(3) flavor symmetry is broken by the large mass of the strange quark, the observable isoscalars η and η' are mixtures of the SU(3) singlet (η_1) and octet (η_8) states (here we have neglected admixtures of heavy quarks or possible gluon bound states). We can parameterize the mixing in terms of one angle Θ :

$$\begin{aligned} \eta_1 &= (d\bar{d} + u\bar{u} + s\bar{s})/\sqrt{3} \\ \eta_8 &= (d\bar{d} + u\bar{u} - 2s\bar{s})/\sqrt{6} \\ \eta(549) &= \cos\Theta\eta_8 - \sin\Theta\eta_1 \\ \eta'(958) &= \sin\Theta\eta_8 + \cos\Theta\eta_1 \end{aligned} \tag{1.4}$$

If we neglect any possible mass dependence the ratios of the coupling constants within the SU(3) nonet depend only on the quark charges and on the mixing angle:

$$\begin{aligned} g_{\pi^0_{\gamma\gamma}} \;:\; g_{\eta_{\gamma\gamma}} \;:\; g_{\eta'_{\gamma\gamma}} \;=& \\ < e_q^2 >_{\pi^0} \;:\; \cos\Theta < e_q^2 >_8 - \sin\Theta < e_q^2 >_1 \;:\; & \sin\Theta < e_q^2 >_8 + \cos\Theta < e_q^2 >_1 \end{aligned} \tag{1.5}$$

The subscripts 8 and 1 in Equation 1.5 refer to the octet and singlet parts of the flavor SU(3) group space respectively.

The two-photon coupling constants for the Pseudoscalar-meson are related to their two-photon widths by: [1] , [2]

$$\Gamma_{M\to\gamma\gamma} = \frac{m_M^3}{16\pi}\, g^2_{M_{\gamma\gamma}} \tag{1.6}$$

In Reference 2 the two-photon width of the π^0 is calculated rigorously using the concept of partially conserved axial vector currents together with the axial anomaly which is connected to the triangle diagram in Figure 1.4 . The rigorous calculation of the π^0 two-photon width gives a value (7.63 eV) that matches well with the experimental value (7.85$\pm$0.54 eV) when 3 color degrees of freedom are assumed for

Table 1.1 *Pseudoscalar-meson states as quark-antiquark combinations*

I	I_3	S	Meson	Quark combination	Decay	Mass, MeV
			SU(3) octet			
1	1	0	π^+	$u\bar{d}$	$\pi^\pm \to \mu\nu$	140
1	-1	0	π^-	$d\bar{u}$		
1	0	0	π^0	$(d\bar{d} - u\bar{u})/\sqrt{2}$	$\pi^0 \to \gamma\gamma$	135
$\frac{1}{2}$	$\frac{1}{2}$	+1	K^+	$u\bar{s}$	$K^+ \to \mu\nu$	494
$\frac{1}{2}$	$-\frac{1}{2}$	+1	K^0	$d\bar{s}$	$K^0 \to \pi^+\pi^-$	498
$\frac{1}{2}$	$-\frac{1}{2}$	-1	K^-	$\bar{u}s$	$K^- \to \mu\nu$	494
$\frac{1}{2}$	$\frac{1}{2}$	-1	$\bar{K}^0$	$\bar{d}s$	$\bar{K}^0 \to \pi^+\pi^-$	498
0	0	0	η_8	$(d\bar{d} + u\bar{u} - 2s\bar{s})/\sqrt{6}$	$\eta \to \gamma\gamma$	549
			SU(3) singlet			
0	0	0	η_1	$(d\bar{d} + u\bar{u} + s\bar{s})/\sqrt{3}$	$\eta' \to \eta\pi\pi$ $\to \gamma\gamma$	958

the constituent quarks. The calculated value (0.85 eV) clearly disagrees with experiment when only one color degree of freedom is assumed. This method of finding $\Gamma_{\pi^0 \to \gamma\gamma}$ requires that we assume that the width is not changed significantly in the soft pion limit $m_{\pi^0} \to 0$. It is also necessary to use the pion decay constant f_π which is measured from the process $\pi \to \mu\nu$. N_c is the number of color degrees of freedom.

$$g_{\pi^0_{\gamma\gamma}} = \frac{\sqrt{2}\alpha}{\pi f_{\pi^0}} N_c \; < e_q^2 >_{\pi^0} \tag{1.7}$$

If we assume SU(3) flavor symmetry, then we can assume the equality of the pseudoscalar decay constants, $f_\pi = f_{\eta_8} = f_{\eta_1}$. The two-photon width of the π^0 can then be used to find the widths of the η and η' as a function of mixing angle Θ. This

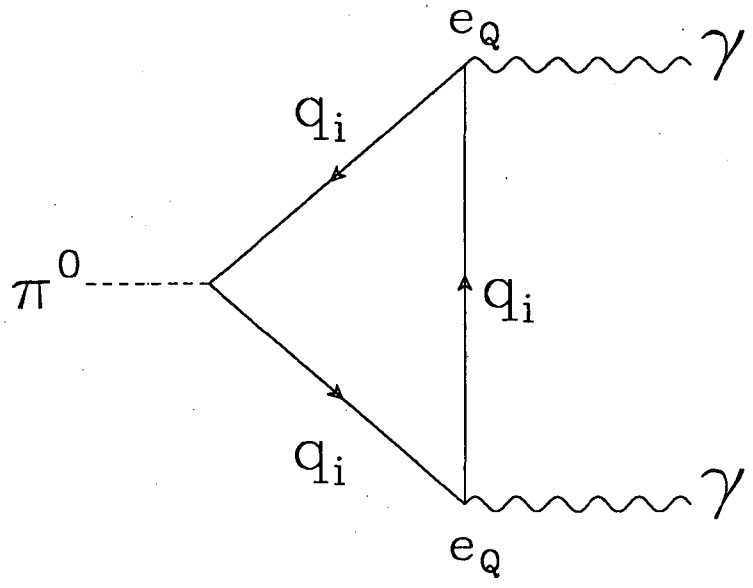

Figure 1.4 *Triangle diagram of the π^0 decay*

allows us to write Equation 1.5 in the form:

$$\frac{\Gamma_{\pi^0\to\gamma\gamma}}{m^3_{\pi^0}} : \frac{\Gamma_{\eta\to\gamma\gamma}}{m^3_{\eta}} : \frac{\Gamma_{\eta'\to\gamma\gamma}}{m^3_{\eta'}} = 3 : (\cos\Theta - \sin\Theta 2\sqrt{2})^2 : (\sin\Theta + \cos\Theta 2\sqrt{2})^2 \tag{1.8}$$

There is some controversy as to the validity of Equation 1.8 (See Chanowitz Reference 3). Chanowitz points out that the assumption that $f_{\eta_8} = f_{\eta_1}$ may not be justified by SU(3) flavor symmetry. He says the assumption that $f_{\eta_8} = f_{\eta_1}$ is really equivalent to the assumption that the wave functions of flavor octet and singlet are the same, an assumption that can not be rigorously justified.

The gauge theory of strong interactions, quantum chromodynamics (QCD), predicts that the gluons that mediate the color force interactions between quarks, can also form gluonic bound states that can be expected to mix with quark-antiquark bound states. Such gluonic mixing may be present in the η and η' [4].

Further weight is given to the hypothesis of gluon mixing in the Pseudoscalar mesons by the existence of the $\iota(1440)$ which is thought to have a spin parity of 0^-. The $\iota(1440)$'s large production in radiative ψ decay could be explained by the "glue

ball" favored channel. [5]

In Reference 4, Rosner assumes that the η and η' bound states are mixtures of gluon-gluon bound states and quark-antiquark states. The gluons, having no electric charge, do not couple to two photons. The two-photon width is thus effected by the degree of gluon mixing. Rosner defines this possible mixing as:

$$\begin{aligned} |N> &\equiv \frac{1}{\sqrt{2}}|u\bar{u} + d\bar{d}> \\ |S> &\equiv |s\bar{s}> \\ |G> &\equiv |gluonium> \end{aligned} \tag{1.9}$$

$$|\eta> = X_\eta|N> + Y_\eta|S> + Z_\eta|G> \tag{1.10}$$

$$|\eta'> = X_{\eta'}|N> + Y_{\eta'}|S> + Z_{\eta'}|G> \tag{1.11}$$

$$X^2 + Y^2 + Z^2 = 1 \tag{1.12}$$

Since Z is dependent on X and Y through normalization condition Equation 1.12 the ratio of the two-photon width of the η and η' with the two-photon width of the π^0 can be written as: [4]

$$\frac{\Gamma_{\eta\to\gamma\gamma}}{\Gamma_{\pi^0\to\gamma\gamma}} = \frac{1}{9}[\frac{m_\eta}{m_{\pi^0}}]^3(5X_\eta + \sqrt{2}Y_\eta)^2 \tag{1.13}$$

$$\frac{\Gamma_{\eta'\to\gamma\gamma}}{\Gamma_{\pi^0\to\gamma\gamma}} = \frac{1}{9}[\frac{m_{\eta'}}{m_{\pi^0}}]^3(5X_{\eta'} + \sqrt{2}Y_{\eta'})^2 \tag{1.14}$$

Equation 1.13 and Equation 1.14 constrain the region of the X-Y parameter plane within which the actual values of X and Y for the η and η' can lie.

Additional constraints on the allowed X-Y regions come from measurements of other decay widths. More will be said in the last chapter, when we evaluate the measured values of the η' two-photon width found using the 3 decay modes considered in

this thesis:

(1) $\eta' \rightarrow \rho\gamma$

(2) $\eta' \rightarrow \eta\pi^+\pi^-; \eta \rightarrow \gamma\gamma$

(3) $\eta' \rightarrow \eta\pi^+\pi^-; \eta \rightarrow \pi^+\pi^-\pi^0\ , \pi^+\pi^-\gamma$

Chapter 2. The Mark II at PEP

PEP is a large positron-electron storage ring, 2.2 km in circumference with 6 interaction regions. (See Figure 2.1) Three bunches each of positrons and electrons circulate, colliding every 2.4 μsec at each interaction region. The beams interact in a region with an effective RMS width of 480 μm in the horizontal (x) direction, 60 μm in the vertical (y) direction and 1.5 cm along the beam (z) direction.

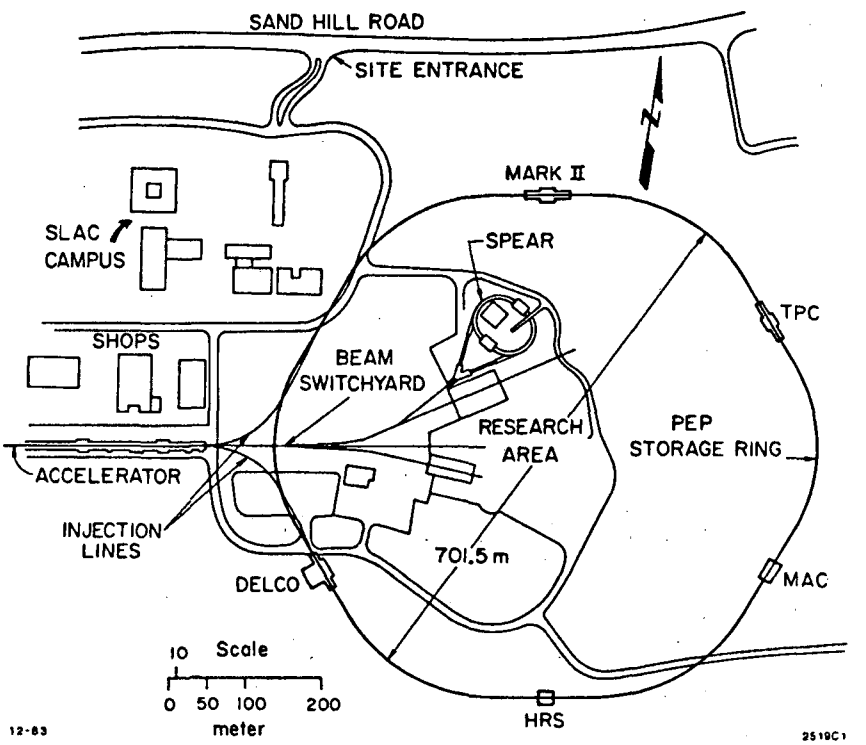

Figure 2.1 *An overview of the SLAC site and PEP ring*

The Mark II at PEP was a general purpose magnetic spectrometer designed to

detect the charged and neutral particles resulting from high energy e^+e^- annihilation and the collision of virtual photons associated with the electric fields surrounding the electrically charged positrons and electrons in the beam bunches. [6] [7] The detector's various components provided both particle tracking and electromagnetic calorimetry as well as limited particle identification capability. In the central two thirds of the solid angle there are drift chambers for momentum determination, a Time of Flight (TOF) system for identifying slow moving hadrons, a Liquid Argon electromagnetic calorimeter for electron and photon identification and 4 layers of steel and proportional tubes for muon identification. In addition,at smaller polar angles there are lead proportional chamber endcaps and a Small Angle Tagger system used for identifying small angle electrons and for luminosity determination. (See Figure 2.2 , Figure 2.3 and Figure 2.4)

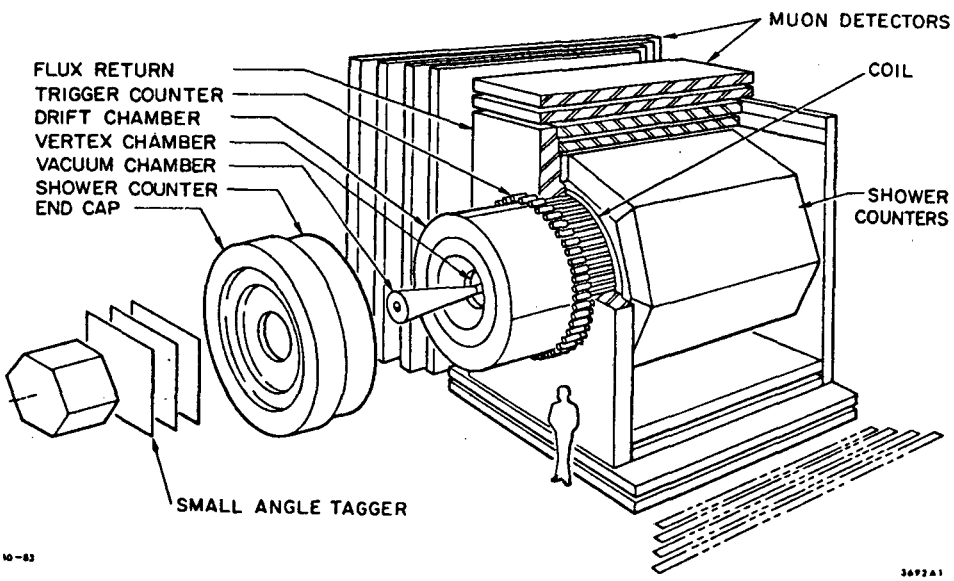

Figure 2.2 *A cutaway side view of the Mark II PEP5 detector*

The Mark II was moved from the SPEAR e^+e^- storage ring at the Stanford Linear Accelerator Center (SLAC) during the summer of 1979. A total of approximately 220 pb^{-1} of data at a center of mass energy of 29 GeV were collected at PEP by of the end of the experiment in the spring of 1984. During the Mark II's history at PEP,

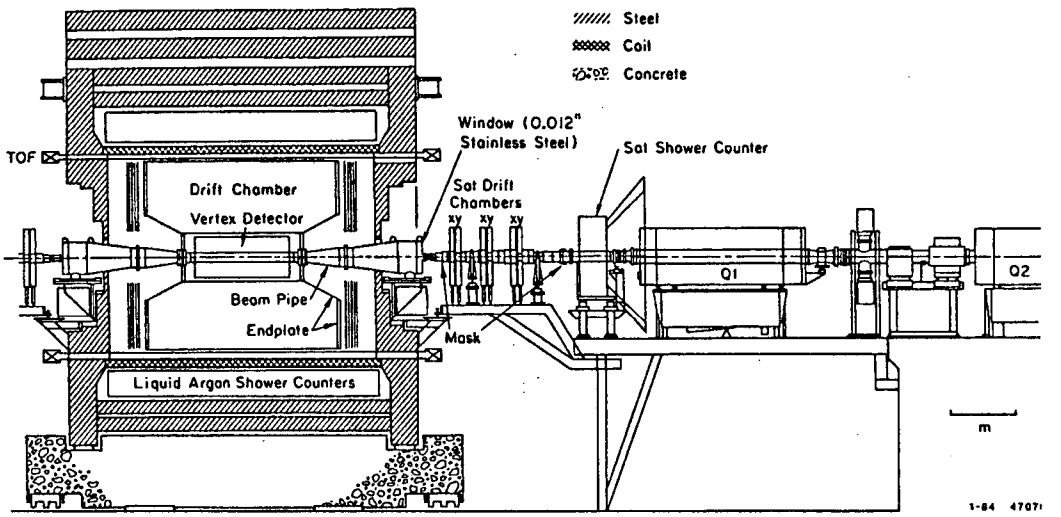

Figure 2.3 *An isometric view of the Mark II PEP5 detector*

several detector configurations were used. We will be using only data collected after the Drift Chamber magnetic field strength was reduced to 2.35 kG by a partial lost of magnetic coil windings.

2.1 The Vertex Chamber

The Vertex Chamber (VC) was a high resolution drift chamber designed to reconstruct secondary vertices due to particle decays. (See Figure 2.5) This capability also allowed accurate extrapolation of tracks to the beam interaction point. The VC consisted of seven axial wire layers that were separated into two groups to optimize the extrapolation measurement: an inner band of four layers of 60-70 sense wires at a mean radius of $\approx$ 10 cm, and an outer band of three layers of 180-190 sense wires at a mean radius of $\approx$ 30 cm. The tracking data at small radii provided by the VC significantly improved the overall momentum resolution of the combined VC and Main Drift Chamber tracking system.

In order to minimize multiple coulomb scattering errors, the beam pipe doubled as the VC inner wall and was constructed from Beryllium, a low Z material. The 1.4 mm thick beam pipe totaled $\approx$ 0.6% of a radiation length and had a radius of 7.8 cm. With a measured spatial resolution of about 100 μm per layer, the VC had an RMS

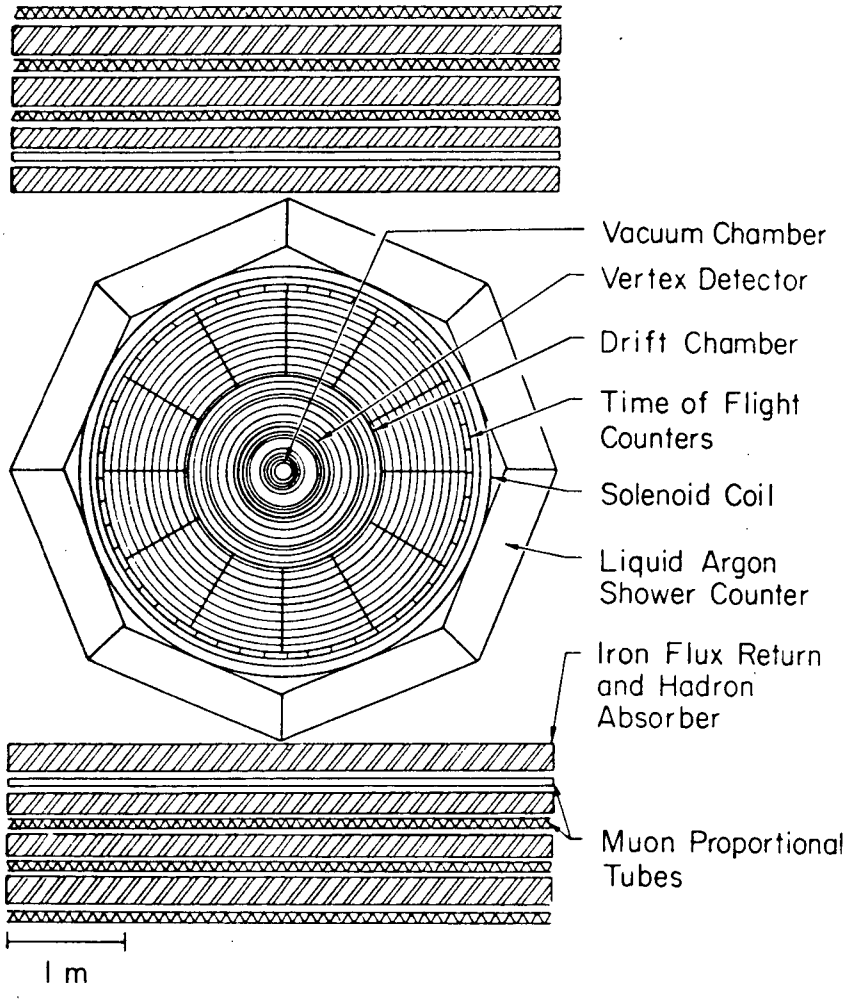

Figure 2.4 *The Mark II detector viewed along the beam axis.*

error of extrapolation to the origin given by

$$\sigma_{ex}^2 = (95\mu m)^2 + (\frac{95\mu m}{p})^2 \tag{2.1}$$

where the second term is due to multiple scattering with momentum p measured in GeV/c. The Vertex Chamber is also important to measuring the distance of closest approach (DOCA) used to reduce background events and assess the trigger efficiency corrections.

2.2 The Main Drift Chamber

The Main Drift Chamber (DC) was the heart of the Mark II tracking system.

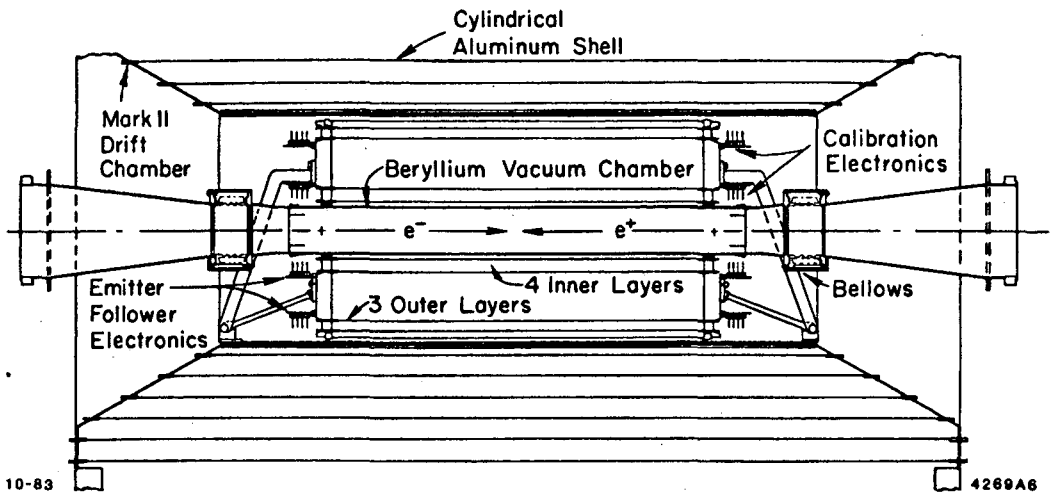

Figure 2.5 *The PEP5 vertex chamber cell configuration*

Sixteen equally spaced concentric sense wire layers covering radii between 41 cm and 145 cm, were contained within a common gas volume. Six layers were axial, while the remaining ten were skewed at ±3 deg to the beam axis to provide stereo information used to obtain a z position measurement. The spatial resolution per layer was typically 200 μm. With the nominal 2.35 kG magnetic field, the momentum resolution of the DC and VC combined was

$$(\frac{\delta p_{xy}}{p_{xy}})^2 = (0.025)^2 + (0.011 p_{xy})^2 \tag{2.2}$$

where p_{xy} is in units of GeV/c, and the first term is due to the contribution of multiple scattering.

The momentum measurement provided by the Drift Chamber is combined with information from the liquid argon calorimeter to identify electrons, and with muon system data to identify muons.

2.3 The Time of Flight System

The Time of Flight (TOF) system surrounded the Main Drift Chamber gas can at a radius of 1.5 m and consisted of 48 longitudinal plastic scintillator strips, each 3.4 m long and instrumented at both ends with photomultiplier tubes. Both

timing and pulse height information from each phototube pair were digitized and used to obtain a slewing corrected time of flight measurement for a track traversing the corresponding scintillator strip. The overall resolution of the TOF system for single hits was approximately 360 psec.

While useful for particle identification during the early days at SPEAR, in the higher energy PEP environment the TOF has been less useful generally since identification is more difficult as the track momentum increases. Fortunately the particles arising from two-photon produced resonance interactions have much less total energy than those produced in e^+e^- annihilation and so the TOF system is still useful for particle identification.

2.4 The Magnet Coil

The aluminum solenoidal magnet coil lies beyond the TOF system at a radius of 1.6 m. The coil was double layered, and water cooled through a conduit that ran inside the conductor. Originally, the magnet provided an axial magnetic field of 4.64 kG, but due to a short that developed between the inner and outer winding, only the outer conductor was powered during all the data collected for this analysis. With one solenoid loop, the nominal magnetic field was 2.35 kG, and was uniform to within 0.5% within the tracking volume. The coil thickness was 1.3 radiation lengths.

2.5 The Liquid Argon Electromagnetic Calorimeter

The primary function of the Liquid Argon Electromagnetic Calorimeter system (LA) was the detection of electromagnetic showers due to photons or electrons. The total solid angular coverage of the LA was about 64% of the 4π solid angle. The eight LA modules encircled the magnet coil in an octagonal array, each module a self contained unit approximately 3.8 m long, 1.8 m wide, and 0.3 m thick. Within each module, separated by 3 mm and immersed in liquid argon, were 37 planes of 2 mm lead/antimony used for both signal collection and as a shower medium. The front of each module (the side closest to the magnet) was used for a trigger gap, consisting of three aluminum planes separated by 8 mm with the middle plane longitudinally

segmented into 3.8 cm wide signal strips. The trigger gap was designed to identify showers that had originated in the magnet coil.

The lead readout planes were at high voltage and were arranged in strips: "F" strips parallel to the beam line that measured azimuth (ϕ), "T" strips perpendicular to the F strips for polar angle (θ) determination, and "U" strips at 45 deg to the F and T directions for ambiguity resolution. (See Figure 2.6) Figure 2.7 schematically shows the alternating high voltage and ground planes, as well as the ganging pattern employed to reduce readout electronics while maximizing front to back shower information. The total calorimeter thickness was $\approx$ 14.5 radiation lengths, with roughly 20% of the shower energy deposited in the Liquid Argon .

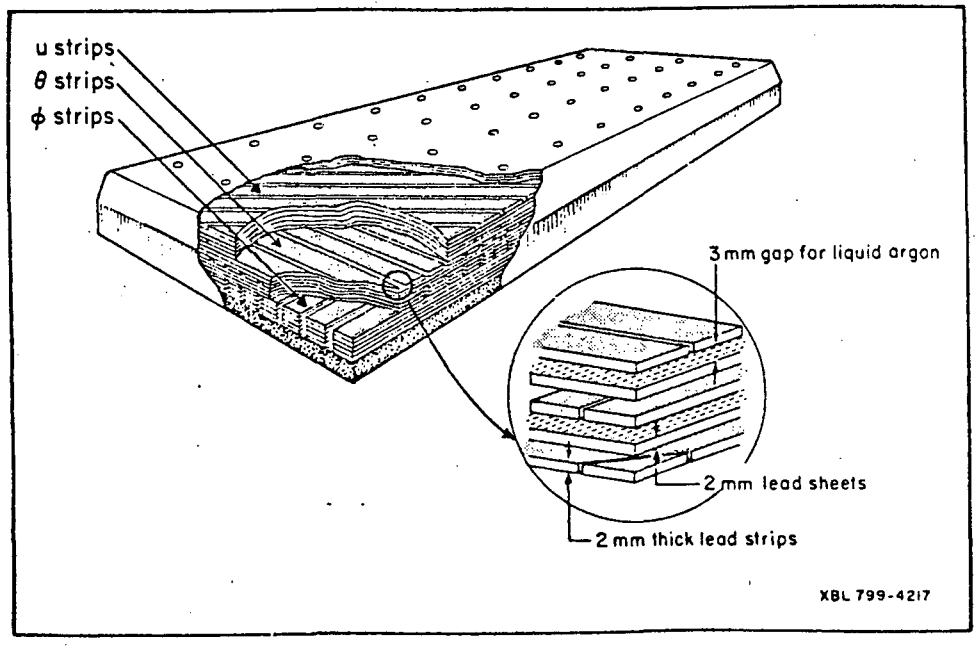

Figure 2.6 *The Liquid Argon module construction*

The LA system achieved an overall RMS energy resolution of $\sigma(E)/E = 13\%/\sqrt{E}$, with a spatial resolution for Bhabha electrons that allowed for the localization of the incident track to within σ =7 mm.

2.6 The EndCap Calorimeter

At each end of the detector, covering polar angles of $15^o \leq \theta \leq 40^o$ are the endcap

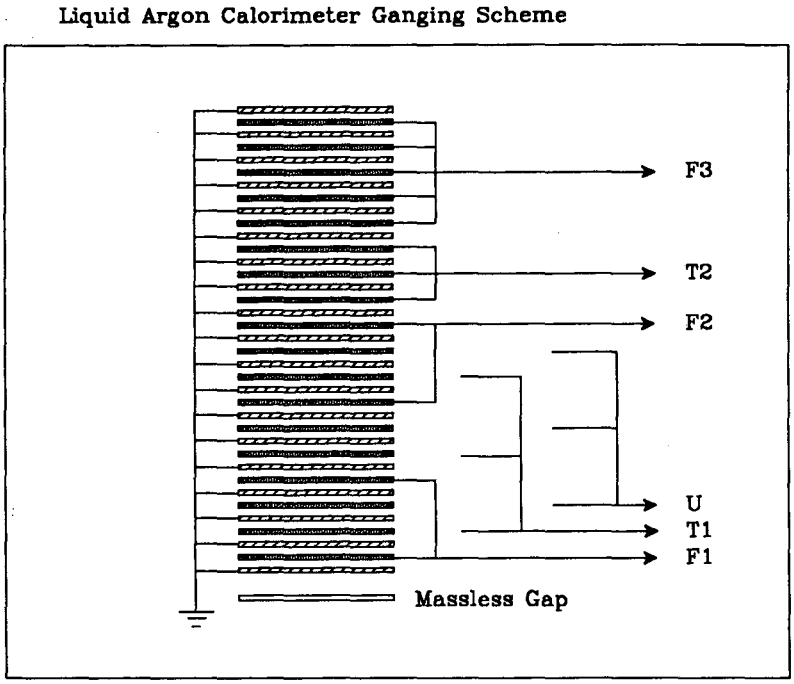

Figure 2.7 *The Liquid Argon module ganging scheme*

(EC) calorimeters. Each endcap consists of 2.3 radiation lengths of lead followed by 2 layers of proportional chambers with an energy resolution given by

$$\frac{\sigma(E)}{E} \sim \frac{60\%}{\sqrt{E}} \tag{2.3}$$

with E in GeV. The EC provides trigger information and limited tagging of small angle events.

2.7 The Muon System

Four muon walls surrounded the Mark II central detector: above, below and on both sides. (See Figure 2.2) Each wall consisted of four layers of steel hadron absorber alternating with layers of extruded aluminum proportional tubes. The first layer measured the polar angle, while the remaining three were oriented for azimuthal discrimination. The overall angular acceptance of the full system was only $\approx 45\%$ of the total 4π solid angle. The muon system and the Liquid Argon account for about

7.4 interaction lengths; a muon typically requires a momentum of at least 1.8 GeV/c to penetrate all four layers.

2.8 The Small Angle Tagging System

A set of tracking and calorimetric devices were symmetrically placed at both ends of the Mark II, covering the angular region of 21 to 82 milliradians with respect to the beamline. The Small Angle Tagger (SAT) consisted of (proceeding outward along the beamline from the interaction point) 3 layers of planar drift chambers with a spatial resolution in the transverse plane of ≈ 300 μm per layer, 3 layers of acceptance defining scintillator, and a lead-scintillator shower counter consisting of $\approx$20 radiation lengths of 18 layers of alternating $\frac{1}{4}$ inch lead and $\frac{1}{2}$ inch plastic scintillator capable of an energy resolution of $\sigma(E)/E = 15\%/\sqrt{E}$. (See Figure2.3) The system was designed to tag small angle Bhabha scattered electrons, as well as the scattered electrons due to two-photon interactions. For the two-photon interactions we will be looking at in this thesis we require that no tagging electrons be observed. These are so called "untagged events". The combination of the acceptance defining scintillator and the shower counters were used to detect Bhabha events to measure the luminosity to a precision of about 5%.

2.9 The Trigger System

The beam crossing rate at PEP of approximately 400 kHz, once every 2.4 μsec, necessitated a selective electronic trigger system. [8] The Mark II two-level trigger was able to hold the event acquisition rate to a few Hertz. The principle employed combined a fast ($\approx$ 1 μsec) and relatively simple primary trigger, with a more sophisticated pattern recognizing secondary trigger that used data from the two drift chambers to find charged tracks. A Master Interrupt Controller (MIC) orchestrated the two-tiered system.

Various primary triggers were employed. The "Charged Trigger" required coincidence of a delayed beam crossing signal, a TOF hit signal and the satisfaction of a DC and VC layer hit pattern criterion. A programmable Memory Logic Module

(MLM) stored the valid tracking system hit patterns. The Neutral Trigger fired if a threshold was exceeded in the front section of any two of the eight Liquid Argon calorimeter modules, or if the total calorimetric energy deposit (including the Endcap Proportional tube calorimeters) exceeded a higher threshold. A "Bhabha Trigger " used the SAT system to trigger on small angle Bhabha scattering events.

Following a primary trigger, the primary electronics sent a signal to MIC that in turn issued a WAIT flag halting data collection. The secondary trigger track finding cycle was initiated by a simultaneous START pulse from the primary trigger. The Master Clock (MC) received the START SIGNAL, sent a BUSY flag to MIC, and oversaw the operation of the trackfinding microprocessors at 10 MHz for 34 μsec. A deadtime of about 3% per kHz of primary trigger rate resulted from the MC cycle delay. The MIC received all secondary trigger data, from the trackfinding electronics as well as from electronics associated with detector components other than the drift chambers, and arbitrated the final trigger decision.

The criteria used by MIC for selecting events to be logged were easily programmable on-line, and several trigger formats were used during the experiment to accommodate short term hardware problems, PEP running conditions and test modes using cosmic rays. If a secondary trigger passed, MIC would interrupt the Mark II Vax 11/780 computer to initiate data transfer and subsequent logging to tape. The process was completed by MIC, whether or not a secondary trigger had occurred, by the lifting of the WAIT flag, and a system RESET.

A selected subset of twelve of the twenty four logical ORs from all of the tracking layers plus the TOF system were available to the secondary trigger, and were used to define two types of legal tracks:

1) A-tracks: those tracks passing through the entire tracking system, required typically 2 of 4 inner VC layers hit, 4 of 8 selected DC layers hit where 2 of these 4 hits were in the outer 6 DC layers, and a TOF hit.

2)B-tracks: More steeply dipped tracks are called B-tracks and usually only required 3 of 4 inner VC hits.

These two track categories are not mutually exclusive; most A-tracks also satisfy the

B-track requirements.

The layers included in the trigger were changed occasionally: the outermost layer was removed from the trigger when its efficiency was seen to deteriorate, and during periods of high PEP beam noise it was sometimes necessary to remove a few inner VC layers to reduce excessive trigger rates.

The principle behind the operation of the secondary trigger track finding was the mapping of the twelve trigger layers into shift registers which were then fed into specialized coincidence modules called Curvature Modules. A device known as the Test and Pickoff Module transferred the tracking chamber shift register bits onto a dedicated trigger system bus. Twenty four programmable Curvature Modules were tied to this dataway, to allow for two sets of twelve different coincidence masks, one for each sign (clockwise or counterclockwise) of track curvature. The Master Clock provided 10 MHz clock pulses that served to rotate each shift register layer at a constant angular speed while the 24 Curvature Modules operated in parallel Figure 2.8 shows schematically how the programmable Curvature Module delays d_i and widths w_i enabled the system to find curved tracks. Track Counters were used to tally the results of the search, and to forward these results to MIC for a final secondary trigger decision. A block diagram of the track finding system is given in Figure 2.9

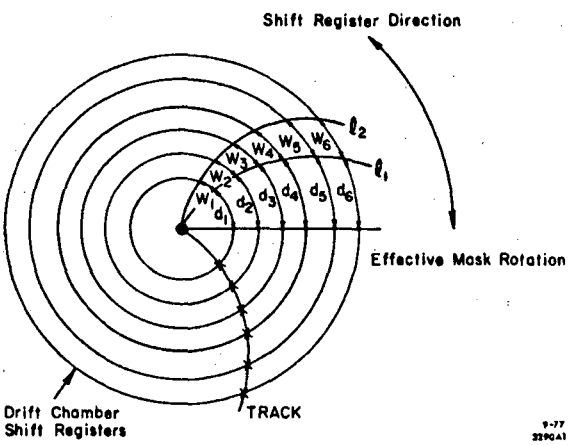

Figure 2.8 *The Mark II trigger road definitions*

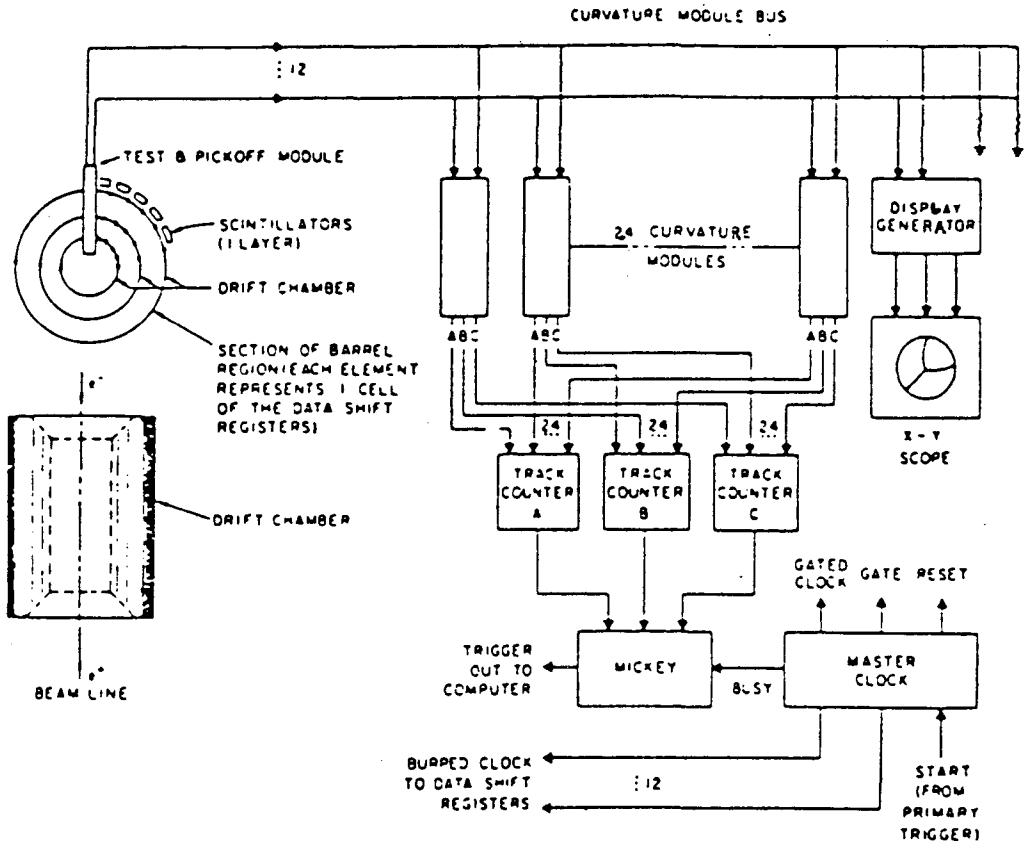

Figure 2.9 *Block diagram of the secondary trigger system.*

The secondary charged trigger was typically satisfied if at least two tracks which satisfy the A-track criteria were found by the pattern recognition hardware. Valid neutral triggers were the TED (Total Energy Deposit) trigger which required at least 1 GeV of energy in the front section of at least two of the eight Liquid Argon calorimeter modules, and the SED (Single Energy Deposit) trigger which was satisfied if the total calorimetric energy exceeded 4 GeV. The Bhabha trigger was scaled by a factor of 16 due to high rates for this trigger mode. The resulting secondary trigger rate rarely exceeded 4 Hz.

2.10 Two Photon event Summary tapes

For reasons of practicality the data collected by the Mark II during its years at

PEP needed to be reduced to a smaller class of events that contained most of the types of events we are interested in. For a large part of the data it was also necessary to reverse the effects of a subroutine called "CHUKIT", added to the Detector tracking program (PASS2), to help reduce the use of computer time. While CHUKIT reduced computer time, it also tended to discard a large part of the two-photon events we were interested in.

"KEEPASS2" recovery of lost events

A program called "KEEPASS2" was used to recover events lost by CHUKIT from the Raw Data tapes. Ideally "KEEPASS2" would be a program that retracks all events that were discarded by "CHUKIT", but in practice compromises were made in order to reduce the volume of output data and computer time used to a manageable level. In addition to the requirement that an event be discarded by CHUKIT an initial cut was made, that required very little computer time, using information for the Hardware Trigger logic. The cuts made were :

1) The trigger hardware must find 1 or more "A tracks".

2) The Hardware curvature modules that fired must have a ϕ separation that indicates that the tracks are not colinear. This cut applies only to two prong events and helps reduce QED background.

3) The event must have been discarded by CHUKIT.

After these initial cuts, a fast tracking routine called "TLTRKR" was used, then another set of cuts was done on track quality:

4) The Distance of Closest Approach (DOCA) of the track in the radial direction of both tracks in 2 charged prong events is required to be less than 2 cm. The Z position of the point of closest approach is required to be less than 10 cm from the interaction point . The track fit used did not include the primary vertex as part of the fit. For four or more charged prong events no DOCA cut was done.

5) The charges of tracks in 2 prong events must be opposite.

After the above cuts the full tracking program is used to reconstruct the event and log it to tape. (See Figure 2.10)

The "2PHOTSUM" summary tape program

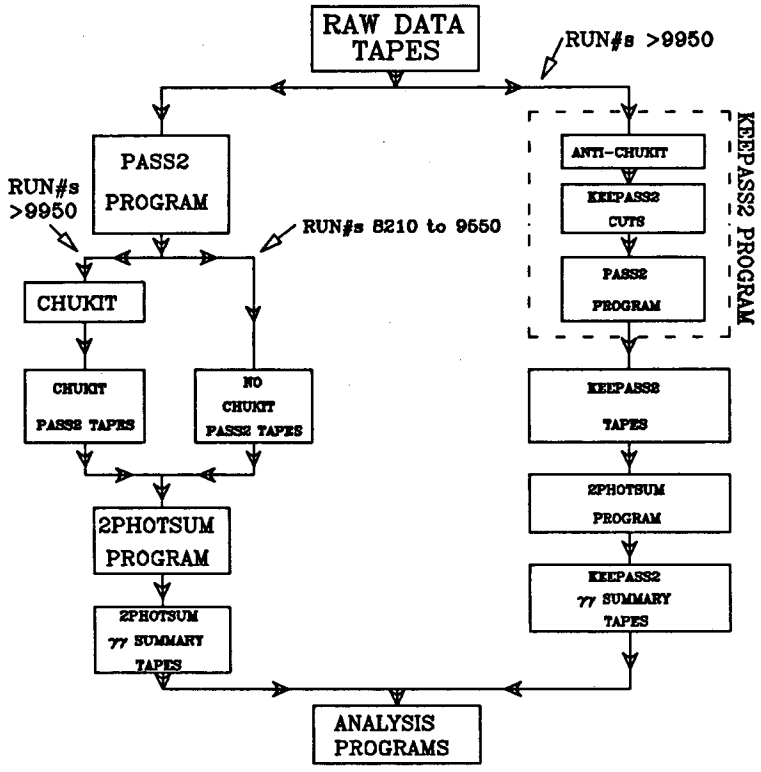

Figure 2.10 *A flow chart representing the way raw output data logged by the experiment is processed before use by the Data Analysis programs*

The "2PHOTSUM" data summary tape program is used to further reduce the number of data tapes necessary to hold events of interest to the two-photon interaction data analysis programs. Reduction was achieved by requiring that an event fall into one of a number of interesting event types before it is written to tape. Some initial quality cuts were also made. The full set of cuts used by the 2PHOTSUM program are outlined in Appendix A.

Chapter 3. $\gamma\gamma$ Kinematics and Luminosity Functions

Two-photon interactions are produced in e^+e^- storage rings when virtual photons associated with the charged particles in each counter-rotating bunch collide. The lowest order diagram dominates this interaction, except under unusual kinematic conditions. [9] Figure 3.1 shows the lowest order Feynman diagram. The two-photon interaction can be visualized as the independent emission of virtual photons which then interact with each other, independent of the electrons that radiated them. In other words the production amplitude for photons can be assumed to be a multiplicative factor in the overall amplitude for producing the final state we are interested in. Thus the transition matrix for producing a resonance R can
be written as: [10]

$$T = \frac{e^4}{q_1^2 q_2^2}[\bar{u}(p_1', \sigma_1')\gamma^{\mu_1} u(p_1, \sigma_1)][\bar{v}(p_2', \sigma_2')\gamma^{\mu_2} v(p_2, \sigma_2)]A^R_{\mu_1\mu_2} \tag{3.1}$$

Where:
e = the electric charge normalized so that $\alpha = e^2/4\pi \approx \frac{1}{137}$
u and $\bar{u}$= the free electron Dirac spinors
v and $\bar{v}$= the free positron Dirac spinors

The tensor $A^R_{\mu_1\mu_2}$ describes the physics we are interested in, $\gamma_1^*\gamma_2^* \rightarrow R$. The two-photon transition matrix is then:

$$< R|T|\gamma_1^*\gamma_2^* >= \epsilon_1^{\mu_1}\epsilon_2^{\mu_2}A^R_{\mu_1\mu_2} \tag{3.2}$$

Where $\epsilon_1^{\mu_1}$ and $\epsilon_2^{\mu_2}$ are the polarization four-vectors of the two photons. The kinematic variables are defined in Figure 3.2, for any produced final X. For our case final state X is a resonance R.

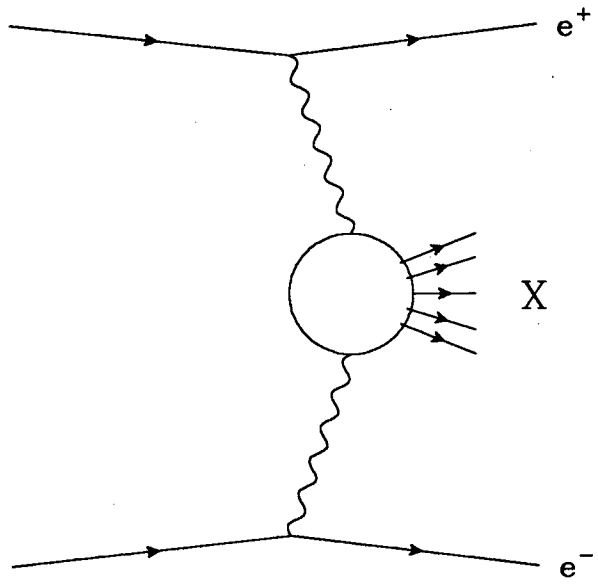

Figure 3.1 *The Principal Feynman diagram for two-photon interactions*

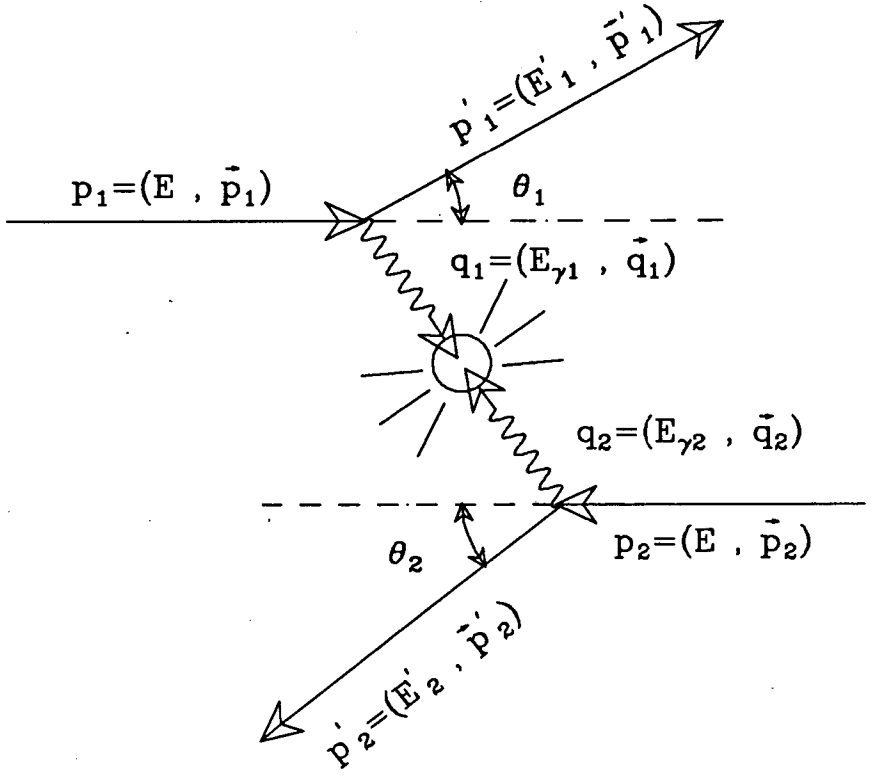

Figure 3.2 *Kinematics of the two-photon reaction* $e^+e^- \rightarrow e^+e^-X$

Equation 3.1 can be used to find the $e^+e^- \rightarrow e^+e^-R$ differential cross-section

as the sum of structure functions. The structure functions assume that the $e^+e^- \rightarrow e^+e^-R$ cross-section obeys the conservation laws :Lorentz covariance, Parity, conservation of Electromagnetic Current and Time-reversal symmetry. The hermiticity of the interaction matrix is also assumed. Keeping only those terms in the structure function expansion involving transverse photons, we have:

$$\frac{d\sigma(e^+e^- \rightarrow e^+e^-R)}{dp_1' dp_2'} = \frac{\alpha^2}{16\pi^4 E_1' E_2'} \frac{1}{q_1^2 q_2^2} \sqrt{\frac{(q_1 q_2)^2 - q_1^2 q_2^2}{(p_1 p_2)^2 - m^4}} \{4\rho_1^{++}\rho_2^{++}\sigma_{TT} + 2|\rho_1^{+-}\rho_2^{+-}| \tau_{TT} \cos 2\varphi \} \tag{3.3}$$

Where:

m= rest mass of an electron

σ_{TT}= cross section for the collision of two transverse photons.

$\tau_{TT} = \sigma_{\parallel} - \sigma_{\perp}$

$\sigma_{\parallel}$= cross section for the collision of two transverse photons with parallel linear polarizations.

$\sigma_{\perp}$= cross section for the collision of two transverse photons with orthogonal linear polarizations.

ρ_i^{ab}= elements of the photon density matrix for a photon produced by the ith particle; a,b = ± 1, 0.

φ= angle between the scattering planes of colliding particles in c.m.s. of the virtual photons.

The full structure function expression which contains the non-transverse terms as well as the transverse terms can be found in Reference 11. The last term in Equation 3.3 disappears when the φ angle is integrated over to find the luminosity for transverse photons.

Due to the photon propagators in Figure 3.1 the photons are emitted predominantly at small angles, of the order m/E. The $\gamma\gamma$ system invariant mass tends to be small, since the photon energies follow roughly the characteristic Bremsstrahlung spectrum of $\sim 1/E_\gamma$.

Assumptions must be made in order to define a single luminosity function. These assumptions are:

1) Only transverse virtual photons are considered. This assumption is reasonable for the untagged cross-section since for cases where both tagging electrons are not detected, the photon flux is dominated by nearly real photons (low Q^2). Real photons must have only transverse components.

The Q^2 is defined for each virtual photon as:

$$Q^2 = -q^2 = -(p - p')^2 \tag{3.4}$$

For $\theta >> m/E$ Equation3.4 reduces to:

$$Q^2 \approx 2EE'(1 - \cos\theta) \tag{3.5}$$

Equation 3.5 gives $Q^2 \approx 10GeV^2$ for a beam electron scattered at θ= 22 mrad, the smallest tagging angle. Reference 10 gives the soft photon limit as :

$$Q^2 = m\ W \tag{3.6}$$

Where $W^2 \equiv -(q_1 + q_2)^2$. About 90% of all the photons have Q^2's below the value given by Equation 3.6, which for a $\gamma\gamma$ mass equal to the η' mass is $4.9 \times 10^{-4}GeV^2$. The kinematic lower limit on Q^2 is :[10]

$$Q^2_{min} = m^2 \frac{W^4}{s(s - W^2)} \tag{3.7}$$

For the η' mass $Q^2_{min} = 3.1 \times 10^{-13}GeV^2$.

2) The photon mass dependence of σ_{TT} is neglected:

$$\sigma_{TT}(W^2, q_1^2, q_2^2) = \sigma_{TT}(W^2, 0, 0) \equiv \sigma(W^2)$$

3) The azimuthal angles of the scattered electrons are, in all cases, integrated over. Terms proportional to the relative polarization of the transverse photons are neglected.

The luminosity function used in this thesis comes from J.H. Field (Reference 12) and is superior to the usual "equivalent photon approximation" (EPA) form of the two-photon luminosity function since it does not assume that the luminosity function can factorized as the product of two independent photon flux factors.

The luminosity as a function of the ratio of the $\gamma\gamma$ invariant mass to the total beam energy is shown in Figure 3.3 for a sample range of energies and tagging angles. Figure 3.3 shows that the two-photon flux drops rapidly with the increasing mass of the $\gamma\gamma$ system. In addition if one or more of the beam electrons is observed within the acceptance of the Small Angle Tagger (SAT), one or both virtual photons have a large Q^2 and so the two-photon luminosity is greatly reduced. It must be kept in mind that the luminosity expression that is commonly used is for transverse-transverse photons only. If tagging electrons are observed other structure functions can become important.

Since the η' is a pseudoscalar only the transverse-transverse structure function can contribute. This can be shown by arguments involving the spin, Parity and Bose symmetry of the two-photon wave function. This argument also shows that the net helicity along the collision axis must be zero ($\lambda = 0$) for the production of pseudoscalars.

For a pseudoscalar we must have J=0 and negative parity. To have negative parity the spatial part of the two photon wave function must have a negative parity, the photons have the same intrinsic parity. Only a spatial L=1 state can give the right parity and still form a J=0 state when combined with the spin of the photons. In addition if we quantize spin and angular momentum along the collision axis only states with spatial m_L=0 can be produced in a two body collision. To satisfy Bose statistics the total wave function must be symmetric under particle interchange. Since the L=1 spatial state is anti-symmetric the total spin of the two photons must be

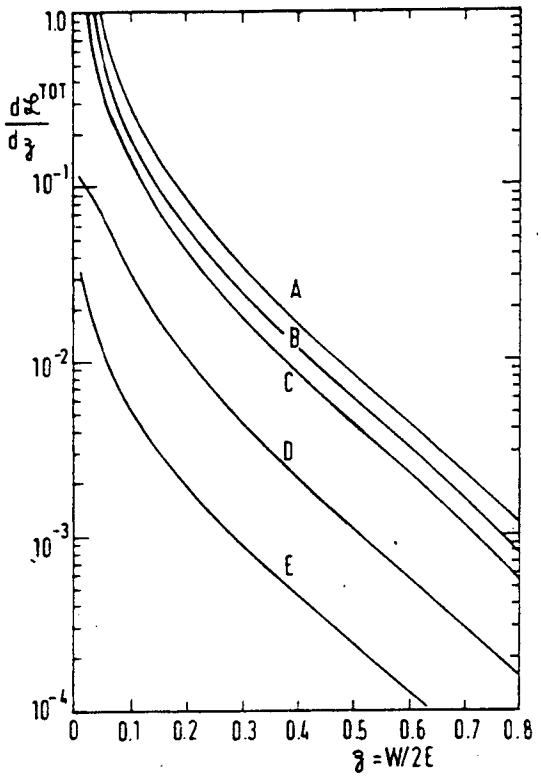

Figure 3.3 *Two-photon differential luminosity curves. Curves A, B, C: Total luminosity for E=1000, 100, 15 GeV. Curve D: Single tagged luminosity for tagging in* $0 < \phi < 2\pi, 20 < \theta < 200$ *mrad, E=15 GeV. Curve E: Double tagged luminosity for tagging in* $0 < \phi < 2\pi, 20 < \theta < 200$ *mrad, E=15 GeV.*

anti-symmetric and so S=1. We now have only 3 candidate total wave functions: $m_L = 0\ m_S = 0$, $m_L = 0\ m_S = +1$ and $m_L = 0\ m_S = -1$. Only the $m_L = 0\ m_S = 0$ state has a J=0 component. The total spin state S=1 $m_S = 0$ can be decomposed into the sum of products of the photon spins as:

$$|S = 1, m_S = 0 > = \frac{1}{\sqrt{2}}[\ |\Rightarrow \Leftarrow> - |\Leftarrow \Rightarrow>\ ] \tag{3.8}$$

So only net helicity zero transverse photon states contribute to the production of pseudoscalars.

Chapter 4. Event Simulation

In order to calculate the actual number of events produced while knowing only the observed number of events we must know the efficiency for finding events. This is why the simulation of events by Monte Carlo programs is vital to a $\Gamma_{\gamma\gamma}$ measurement. Monte Carlo programs randomly generate events based on an assumed knowledge of the probability distributions connected with an event's production and then simulate the detector's response to the particles coming from the event.

In this chapter we look at the assumed matrix elements for each of the decay modes simulated. We also independently verify that the Monte Carlo generated $\mid \Sigma\overrightarrow{P_t} \mid$ distribution is correct. In the chapters that follow the parts of the Monte Carlo simulation that may cause the largest errors to the given two-photon width measurement are discussed on a case by case basis.

4.1 Tagging angles and generated event normalization

The distribution of transverse momentum relative to the beam direction, of events generated by the Monte Carlo program is important to the correct determination of the efficiency for finding an event. Those events with larger $\mid \Sigma\overrightarrow{P_t} \mid$'s tend to have their decay products boosted in the transverse direction, where they can be more readily found by the detector. Thus the overall efficiency for finding events is a function of the Monte Carlo 's generated P_t distribution.

The $\mid \Sigma\overrightarrow{P_t} \mid$ distribution assumed by our particular two-photon Monte Carlo generator used to simulate all decay modes is a distribution based on empirical data gleaned from real events and as such should be checked. Fortunately the P_t distribution can be found directly from theory. [10]In Reference 10 a general covariant formalism for the reaction $e^+e^- \rightarrow e^+e^-(resonance)$ is derived.

Using the kinematic expressions in Ref. 10, I produced a Monte Carlo program whose sole purpose was to simulate two-photon interaction kinematics, using expressions that are valid in all regions of Q^2. This required a program that could handle

equations whose numerical values vary over many orders of magnitude. The difficult problems in correctly handling round off errors for these expressions had to be overcome in order that the result not be dominated by round off errors. The choice of parameter space Jacobians was also vital. Without a reasonable Jacobian the amount of computer time used becomes impractically large per event generated. (See Figure 4.1)

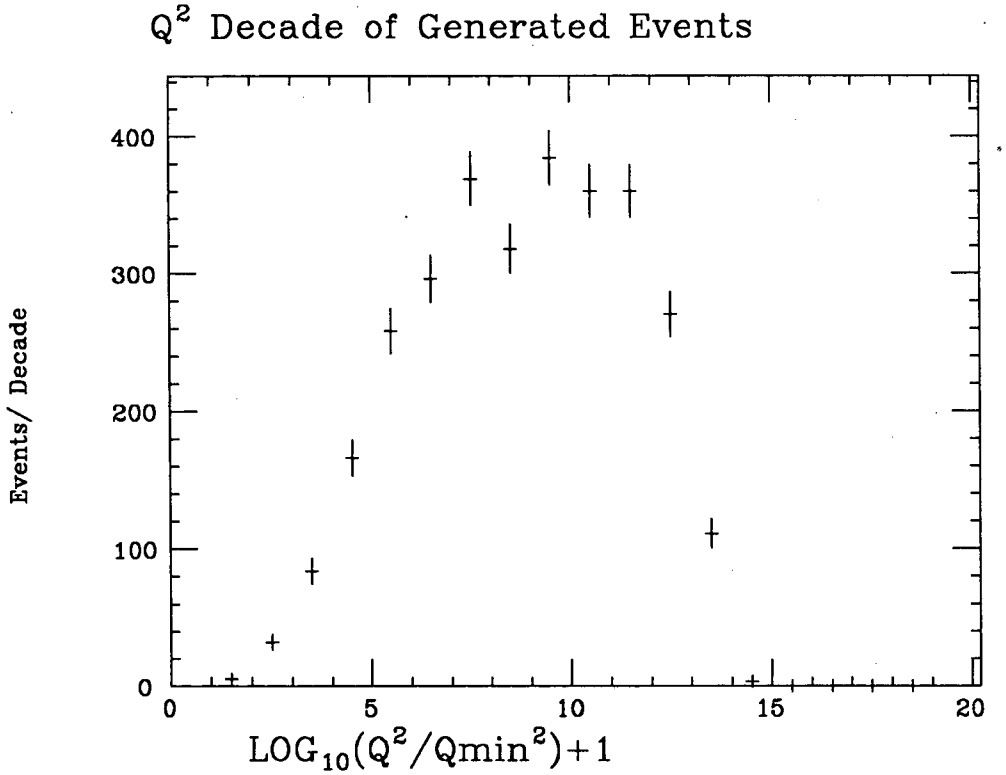

Figure 4.1 *The Q^2 distribution of photons producing a resonance at 958 MeV/c^2 . The SAT2 program was used to find this distribution.*

The name of the Monte Carlo program based on Reference 10 is "SAT2". The SAT2 P_t distribution was compared to the nominal Monte Carlo for untagged and anti-tagged events. Untagged events are those for which the angles of the scattered electrons are ignored. For the anti-tagging case *both* scattered beam electrons were required to have angles outside of the tagging range $21mrad < \theta < 82mrad$.

In Table 4.1 we have a good correspondence between the theoretically based SAT2 Monte Carlo calculation and the empirically based nominal Monte Carlo calculation.

Table 4.1 *A comparison of* $|\Sigma\overrightarrow{P_t}|$ *of events based on theory and* $|\Sigma\overrightarrow{P_t}|$ *of events from the nominal Monte Carlo program. SAT2 is the Monte Carlo program based on theory alone*

event P_t range	Nominal M.C. untagged	SAT2 M.C. untagged	SAT2 M.C. anti-tagged
P_t <10 MeV/c	38.2% ± .30%	34.7% ± 2.0%	34.6% ± 1.5%
P_t <50 MeV/c	60.0% ± .36%	58.0% ± 2.0%	57.7% ± 2.0%
P_t <200 MeV/c	78.9% ± .40%	80.7% ± 2.3%	79.2% ± 2.3%

To see how much of a difference the use of the theoretically based Monte Carlo calculation makes to the overall efficiency, I looked at a decay mode whose overall efficiency is sensitive to this P_t distribution. The decay mode $\eta' \rightarrow \eta\pi^+\pi^-; \eta \rightarrow \gamma\gamma$ has the lowest momentum pions of any decay mode we will consider. The efficiency was found for 50 MeV/c wide bins using the nominal Monte Carlo program and then the anti-tagged P_t distribution generated by SAT2 was substituted. When this was done the overall efficiency changed by only 1%.

4.2 Matrix Elements Used For Event Generation

For two of the decay modes we will be considering, no special attention to the matrix element for their decay was required by spin parity considerations. The two decays :

$\eta' \rightarrow \eta\pi^+\pi^-; \eta \rightarrow \gamma\gamma$ and $\eta' \rightarrow \eta\pi^+\pi^-; \eta \rightarrow \pi^+\pi^-\pi^0$, $\pi^+\pi^-\gamma$ both have spin parity: $J^P : 0^- \rightarrow 0^-0^-0^-$. Only a phase space weighting is assumed for these decay modes. [13] But for the two decay modes $\eta' \rightarrow \rho\gamma$ and $a_2 \rightarrow \rho\pi$ the spin parity must be taken into account when the Monte Carlo events are generated, in order that the correct angular distribution of final state particles be produced.

The Monte Carlo calculation Matrix Element for $\eta' \rightarrow \rho^0\gamma; \rho^0 \rightarrow \pi^+\pi^-$

For the $\eta' \rightarrow \rho\gamma$ decay mode the spin parity of $0^- \rightarrow 1^-1^-$ implies an M1 magnetic dipole transition for which Reference 13 gives :

$$|M|^2 \sim q_{\pi+}^2 k_\gamma^2 M_{\pi+\pi-}^2 \sin^2\theta_{helicity} \tag{4.1}$$

Where:

$q_{\pi+}$= The momentum of the π^+ in the $\pi^+\pi^-$ center of mass frame.

k_γ= The momentum of the γ in the $\pi^+\pi^-$ center of mass frame.

$M_{\pi+\pi-}$= The invariant mass of the $\pi^+\pi^-$ system.

$\theta_{helicity}$= The helicity angle, defined as the angle that the 3-momenta of the π^+ and γ make with each other in the $\pi^+\pi^-$ center of mass frame.

The weight to phase space due to the $\rho^0 \rightarrow \pi^+\pi^-$ resonance. (Reference 14 equation 11).

$$(\rho^0 \textit{ decay phase space weight}) = \frac{M_{\pi+\pi-}}{q_{\pi+}} \frac{\Gamma(M_{\pi+\pi-})}{(M_\rho^2 - M_{\pi+\pi-}^2)^2 + M_\rho^2\Gamma^2(M_{\pi+\pi-})} \tag{4.2}$$

The decay width of the ρ^0 resonance is parameterized in Reference 15 as :

$$\Gamma(M_{\pi+\pi-}) = \Gamma(M_\rho)\frac{2q_{\pi+}^3}{q_\rho(q_\rho^2 + q_{\pi+}^2)} \tag{4.3}$$

Where:

M_ρ= The nominal ρ^0 mass.

$\Gamma(M_\rho)$= The nominal decay width of the ρ^0 resonance

q_ρ=The momentum in the $\pi^+\pi^-$ center of mass when the invariant mass of the $\pi^+\pi^-$ is equal to the ρ^0 mass.

The Monte Carlo calculation Matrix Element for $a_2(1320) \rightarrow \rho^{\pm}\pi^{\mp}; \rho^{\pm} \rightarrow \pi^{\pm}\pi^0$

The $a_2 \rightarrow \rho\pi$ decay mode is a background to the decay mode $\eta' \rightarrow \rho\gamma$. The $a_2(1320)$, being a spin-2 particle, can be produced in two-photon interactions with total helicity 2 or 0. The Monte Carlo program used here assumes that the helicity 2 production mode dominates. [16]

The matrix element for production of $a_2(1320)$ with helicity 2 is proportional to : [14 , 17]

$$|M|^2 \sim \Big| P^2_{\rho+} P_{\pi^0} \sin\theta_{\rho+} \sin\theta_{\pi^0} \sqrt{\cos^2\theta_{\rho+} \sin^2\phi_{\pi^0} + \cos^2\phi_{\pi^0}} \sqrt{\frac{M_{\pi+\pi^0}}{P_{\pi+}}} \frac{\sqrt{\Gamma(M_{\pi+\pi^0})}}{(M^2_\rho - M^2_{\pi+\pi^0}) - i\, M_\rho \Gamma(M_{\pi+\pi^0})} + P^2_{\rho-} P_{\pi^0} \sin\theta_{\rho-} \sin\theta_{\pi^0} \sqrt{\cos^2\theta_{\rho-} \sin^2\phi_{\pi^0} + \cos^2\phi_{\pi^0}} \sqrt{\frac{M_{\pi-\pi^0}}{P_{\pi-}}} \frac{\sqrt{\Gamma(M_{\pi-\pi^0})}}{(M^2_\rho - M^2_{\pi-\pi^0}) - i\, M_\rho \Gamma(M_{\pi-\pi^0})} \Big|^2 \tag{4.4}$$

The parameterized decay width for the $\rho^{\pm}$ decay is given by:

$$\Gamma(M_{\pi^{\pm}\pi^0}) = \Gamma(M_\rho) \frac{2P^3_{\pi^{\pm}}}{P_\rho (P^2_\rho + P^2_{\pi^{\pm}})} \tag{4.5}$$

Where:

$P_{\rho^{\pm}}$= The momentum of the $\rho^{\pm}$ in the $\gamma\gamma$ center of mass frame.

P_{π^0}= The π^0 momentum in the $\pi^0\pi^{\pm}$ center of mass frame.

$P_{\pi^{\pm}}$= The momentum of the $\pi^{\pm}$ in the $\pi^0\pi^{\pm}$ center of mass frame.

$\theta_{\rho^{\pm}}$= The angle that the $\rho^{\pm}$ momentum makes with the axis of collision of the colliding gammas in the $\gamma\gamma$ center of mass frame.

θ_{π^0}= The angle between the π^0 momentum in the ρ center of mass frame and the direction of the ρ in the $\gamma\gamma$ center of mass frame.

ϕ_{π^0}= The polar ϕ angle measured with respect to the plane defined by the $\gamma\gamma$ collision axis and the direction of the ρ. The Z axis is the direction of flight of the ρ.

It is important to note that for the above angles to be well defined, Lorentz boosts of the coordinate system must be done in the order: Lab frame to $\gamma\gamma$ center of mass along the $\gamma\gamma$ collision axis in the Lab frame, $\gamma\gamma$ center of mass to the ρ center of mass along the ρ direction in the $\gamma\gamma$ center of mass frame.

Equation 4.4 contains the amplitude for the ρ resonance to be formed by either a $\pi^+\pi^0$ pair or a $\pi^-\pi^0$ pair. Since the final state is $\pi^+\pi^-\pi^0$, the intermediate ρ resonance is not directly observed, so that there is interference between the amplitudes for the ρ^+ and ρ^- intermediate states. All the final state particles are bosons so a constructive interference is assumed. Such an interference is observed in the $a_2^\pm \rightarrow \rho^0\pi^\pm$ decay, where the ρ^0 can be explicitly reconstructed.

Equation 4.4 also includes the weight to phase space terms from Reference 14 that take account of the ρ decay. Thus Equation 4.4 includes the weighting factors used to weight the 3 body phase space distribution generated by the Monte Carlo program. The weighting of 3 body phase space for the $\eta' \rightarrow \rho\gamma$ decay mode may be done separately (Equation 4.2) since no interference between intermediate states is present. This makes Equation 4.4 slightly different from the usual definition of a matrix element of a decay, but this is necessary for practical programming reasons.

Chapter 5. Event reconstruction for $\eta' \to \rho\gamma$ and $a_2 \to \rho\pi$

This chapter will describe the reconstruction of two-photon events with the final observed particles $\pi^+\pi^-\gamma$.

5.1 THE RECONSTRUCTION OF η' AND $a_2(1320)$

In reconstructing resonances produced in two-photon interactions a common set of initial cuts on neutral and charged tracks is used.

5.1.1 General two-photon track cuts

Charged track cuts

The charges of the tracks must be well defined and the tracking program must be able to find a vertex constrained fit to all charged tracks.

The reconstructed track vertices must not be too far from the interaction point. This helps reduce any events coming from interactions of the beam with residual gas particles. These interactions can occur any place along the beams length, while the beam bunches can only interact with each other in the beam crossing region at the interaction point or IP.

We require that the charged tracks hit the Liquid Argon calorimeter and Time of Flight counters within a fiducial region ($|Z| < 1.9$ Meters). This insures that for both real events and Monte Carlo events, that the tracks satisfy the trigger requirements. This is important to finding the correct acceptance, since the detector simulation program does not simulate the trigger completely.

Events with collinear charged tracks are removed to help reduce annihilation background. In annihilation events the system of produced particles is created at rest in the Lab frame. For two-photon events the products are generally boosted along the beam axis making it less likely that two-photon events will be collinear in the Lab frame. For events with charged tracks whose lab frame momenta make an angle relative to each other of θ, we require that $\cos\theta < -0.9$.

We also require that the total energy of all charged tracks seen, be less that 40% of the total available energy from the e^+e^- collision. In a two-photon interaction most of the energy is carried away, unseen, by the outgoing beam electrons.

Neutral track cuts

Fake gammas are sometimes reconstructed near the position of a charged track's entry into a calorimeter. This is due mainly to energy deposited at some distance from the path of the charged track by interactions in the calorimeter. To insure that such gammas are not counted, all gammas within a given radius (defined below) of a charged track are ignored.

There is also a cut made on the detected gamma energy of 150 MeV for the LA and 200 MeV for the Endcaps. The energy cuts reduce background fake gammas due to electronic noise and real low energy backgrounds.

If two showers in a calorimeter share a number of strips then the tracking program must decide how to divide up the energy shared between them. We require that the tracking program not share more that 50% of the gamma's energy with any other gammas in the same module.

The eight Liquid Argon modules are separated from each other by dead regions where the efficiency for finding electromagnetic showers is low. We make a cut that avoids using gammas in these "cracks" between modules by requiring that $|\Delta\phi| > 0.9^o$ from the crack centers.

SAT cuts

Because we are interested only in quasi-real photons we require that no scattered beam electrons are detected by the small angle tagger (SAT). This limits the Q^2 of the interacting virtual photons to small values. (See chapter 3)

5.1.2 Cuts and reconstruction used for $\eta' \rightarrow \rho\gamma$

Events are discarded if more that one bona fide gamma is found in the event. For the reconstruction of $\eta' \rightarrow \rho\gamma$ the distance between charged and neutral tracks is required to be 35cm. This cut is used to discard fake photons in real events. The gamma charged track spacing is shown in Figure 5.1 . The cut is large enough to

avoid the uncertainties in the Monte Carlo simulation due to the use of a routine called HINT that models the interactions of pions within the Liquid Argon calorimeter and so simulates one class of fake photons. Gammas from real $\eta' \rightarrow \rho\gamma$ events tend to be in the opposite direction in the X-Y plane than the charged tracks since they are recoiling against the $\pi^+\pi^-$ system. Since a real gamma coming from $\eta' \rightarrow \rho\gamma$ is not likely to be near the charged tracks, the overall efficiency is actually improved by the reduction of extra gamma vetoes.

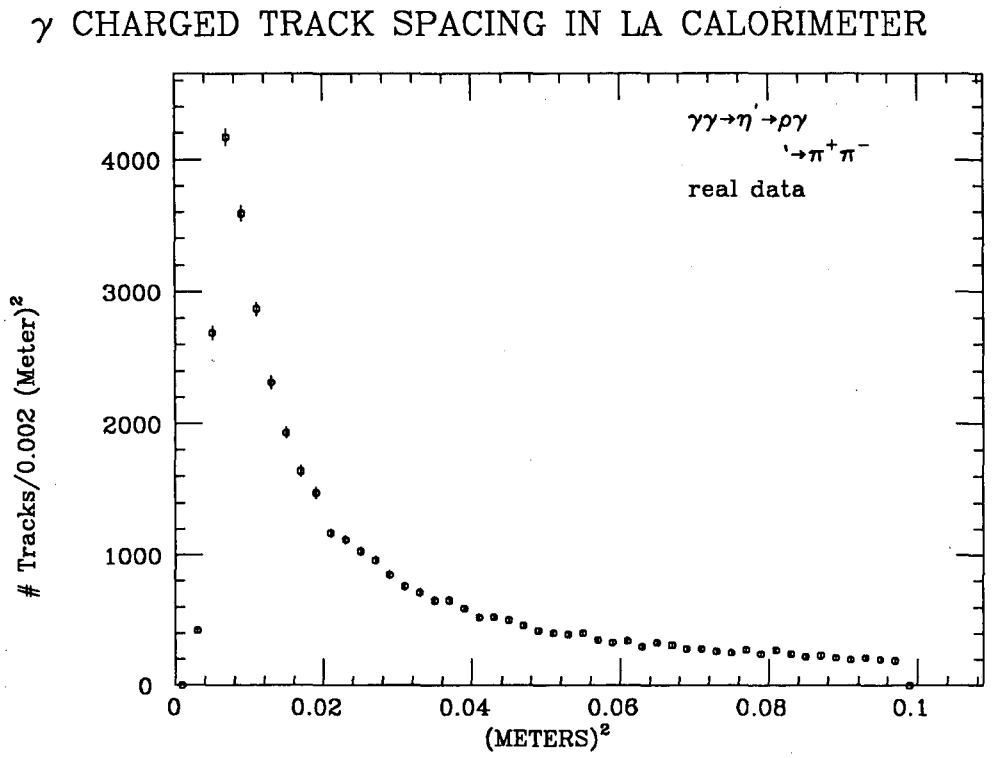

Figure 5.1 *Gamma charged track spacing in Liquid Argon calorimeter*

Since we are interested in finding the π^+ and π^- momenta at the interaction point of the e^+e^- bunches and since the drift chamber and vertex chambers measure the π momentum after traversing material in the detector, we need to correct for the energy and momentum loss in this material. When this momentum correction is made, the change in $\frac{dE}{dx}$ with the change in β of the particle as its energy is lost is correctly accounted for. For pions whose paths are at right angles with respect to the

beam axis the $\frac{dE}{dx}$ correction is 13.6 Mev/c for a measured momentum of 100 Mev/c and 6.1 Mev/c for a measured momentum of 200 Mev/c. The size of this correction is roughly proportional to $\frac{1}{\cos\theta}$ where θ is the angle the path makes with the beam axis.

To help in reducing background $\gamma\gamma \rightarrow e^+e^-\gamma$ several cuts are made. The momentum spectrum of pions from $\eta' \rightarrow \rho\gamma$;$\rho \rightarrow \pi^+\pi^-$ decays is shown in Fig. 5.2 . We discard events whose charged tracks deposit more than 600 MeV in the Liquid Argon or whose momenta are greater than 2.0 GeV/c because this results in little loss of efficiency and further reduces high energy radiative electron background. This cut also makes Time of Flight identification slightly easier, since the Time of Flight mass resolution is worse at larger momenta.

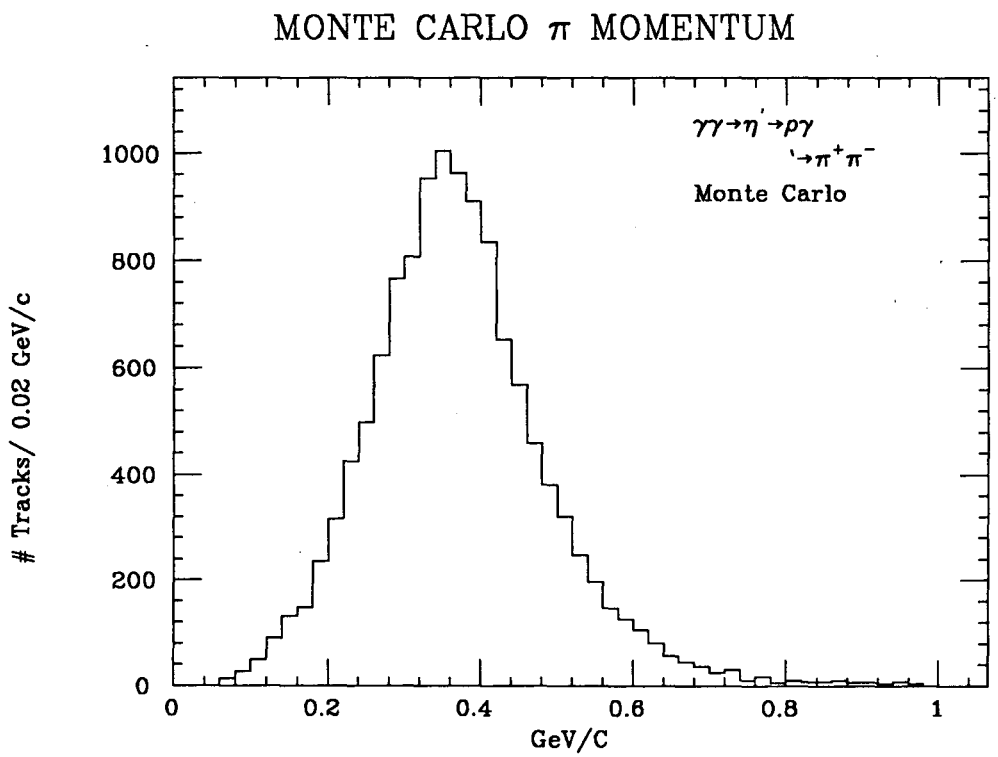

Figure 5.2 *Monte Carlo simulated $\pi^{\pm}$ momentum for $\eta' \rightarrow \rho\gamma$*

A straight line cut is made in the β vs momentum plane for each charged track with Time of Flight information to remove a low momentum high β region populated

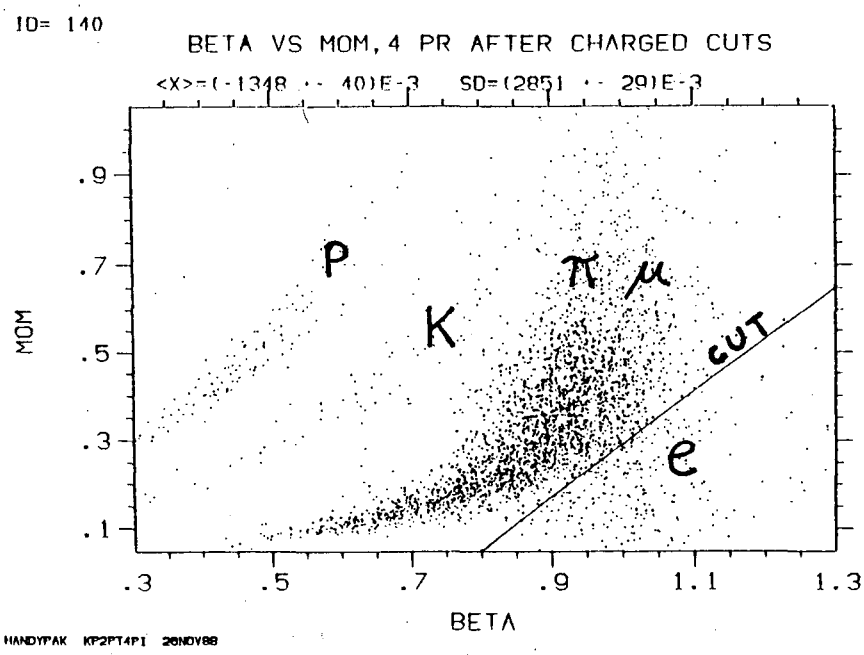

Figure 5.3 *Momentum vs β as found by Time of Flight*

by a large electron background. (see Figure 5.3)

The $\pi^+\pi^-\gamma$ mass without gamma energy correction is shown in Figure 5.4. The gamma direction is well measured while the gamma energy is not. To improve the poor energy resolution of the observed gamma in $\eta' \rightarrow \rho\gamma$ events we take advantage of the kinematics of $\gamma\gamma$ interactions. For events with no tagging electron the net transverse momentum of produced η' s is sharply peaked at zero,thus we can assume that the gamma energy can be adjusted to balance the transverse momentum of the well measured π^+ and π^- while keeping the measured γ direction fixed. The absolute transverse momentum of the gamma momentum is set equal to the absolute transverse momentum of the π^+ π^- system transverse momentum . (See Figure 5.5). The good agreement between the Monte Carlo simulation and the real event $\mid \Sigma\vec{P_t} \mid$ distribution in Figure 5.5 indicates that background events with extra neutrals are not a significant problem for events in the η' mass peak region.

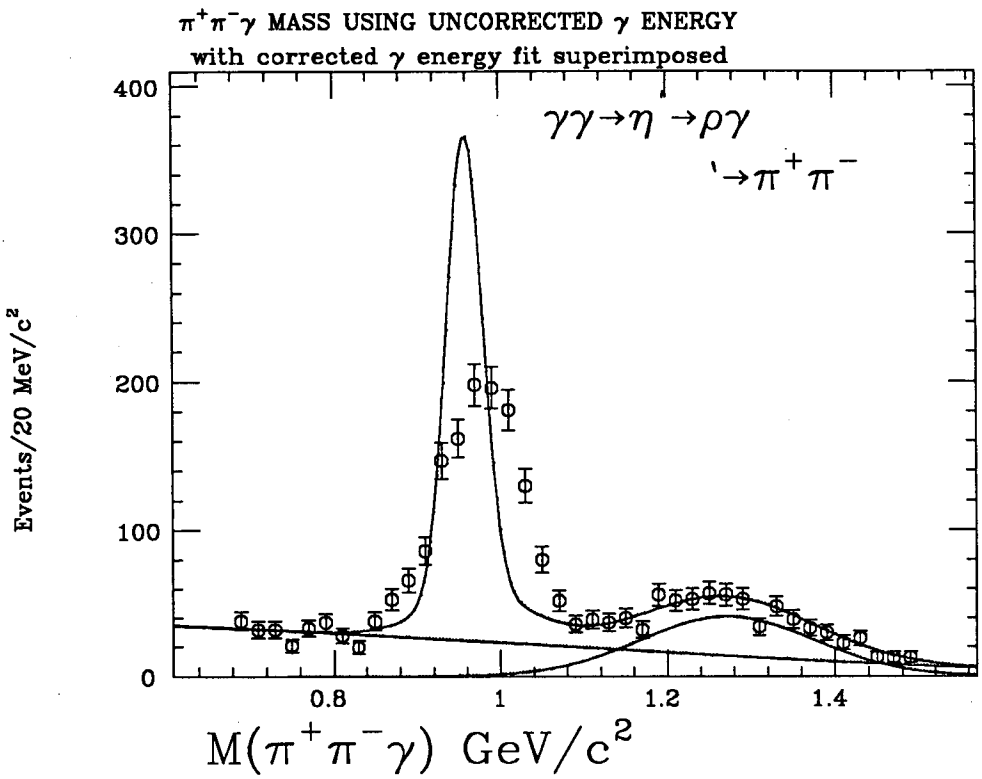

Figure 5.4 *$\pi^+\pi^-\gamma$ mass using no gamma energy correction, the fit with gamma energy correction is superimposed. The straight slanted line is a fit to the overall background, the gaussian centered at about 1250 MeV/c^2 is a fit to the $a_2(1320)$ background.*

A cut of 100 MeV/c on the net transverse momentum of the $\gamma\pi^+\pi^-$ system using the uncorrected gamma energy removes events that have large net transverse momentum (indicating that not all of the decay products were seen).

Events with a corrected gamma energy less than 150 MeV are removed. This insures that the corrected energy is consistent with the threshold energy for detecting the gamma.

Since the gamma energy correction method only requires that the magnitudes of the π^+ π^- and gamma system $\overrightarrow{P_t}$s be set equal and not there directions, it is still possible for the corrected $\mid \Sigma\overrightarrow{P_t} \mid$ to be non zero. The $\mid \Sigma\overrightarrow{P_t} \mid$ of the $\gamma\pi^+\pi^-$ system using the corrected gamma energy is required to be less than 100 MeV/c, this is a way of insuring that corrected gamma momentum and transverse $\pi^+\pi^-$ momentum are reasonably opposite in direction. If their X–Y plane momentum projections are

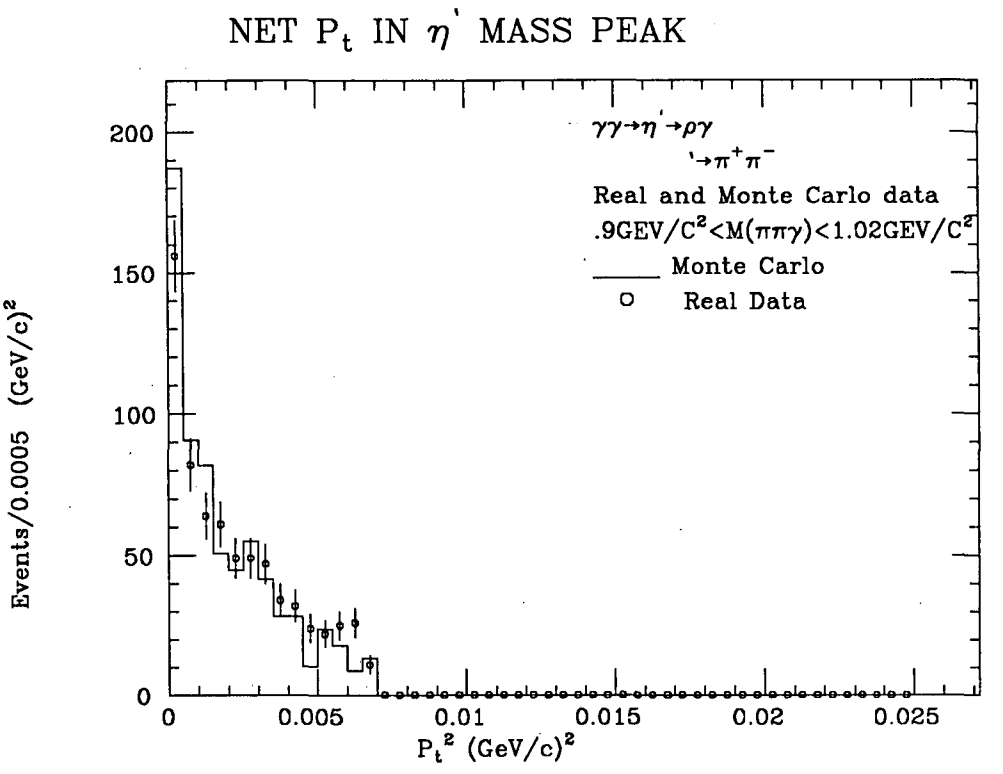

Figure 5.5 *Net P_t for $\eta' \to \rho\gamma$ Monte Carlo and Real events, after gamma energy correction*

collinear the gamma energy correction will give a zero $|\Sigma\overrightarrow{P_t}|$.

A background that we must deal with is the radiative 2 prong event $\gamma\gamma \to e^+e^- \to e^+e^-\gamma$. The gamma in this type of event tends to be radiated along the direction of one of the outgoing charged particles when we boost all momenta into the rest frame of the 2 charged particles. The radiative μ background can be neglected, because the amplitude for radiating a photon drops rapidly with the increasing particle mass. The helicity angle, $\theta_{Helicity}$, is defined as the angle that the gamma momentum 3-vector makes with the π^+ 3-momentum in the π^+ π^- center of mass frame. The helicity angle distribution of the radiative background leads us to make a cut on the cosine of the helicity angle, requiring that $|\cos\theta_{Helicity}|$ be greater than .8 . It is fortunate that the spin parity of the decay $\eta' \to \rho\gamma$; $\rho \to \pi^+\pi^-$: J^P $0^- \to 1^-1^-; 1^- \to 0^-0^-$ leads to a matrix element squared for this decay proportional to $sin^2\theta$ (see Figure 5.6) because for this decay mode the radiative

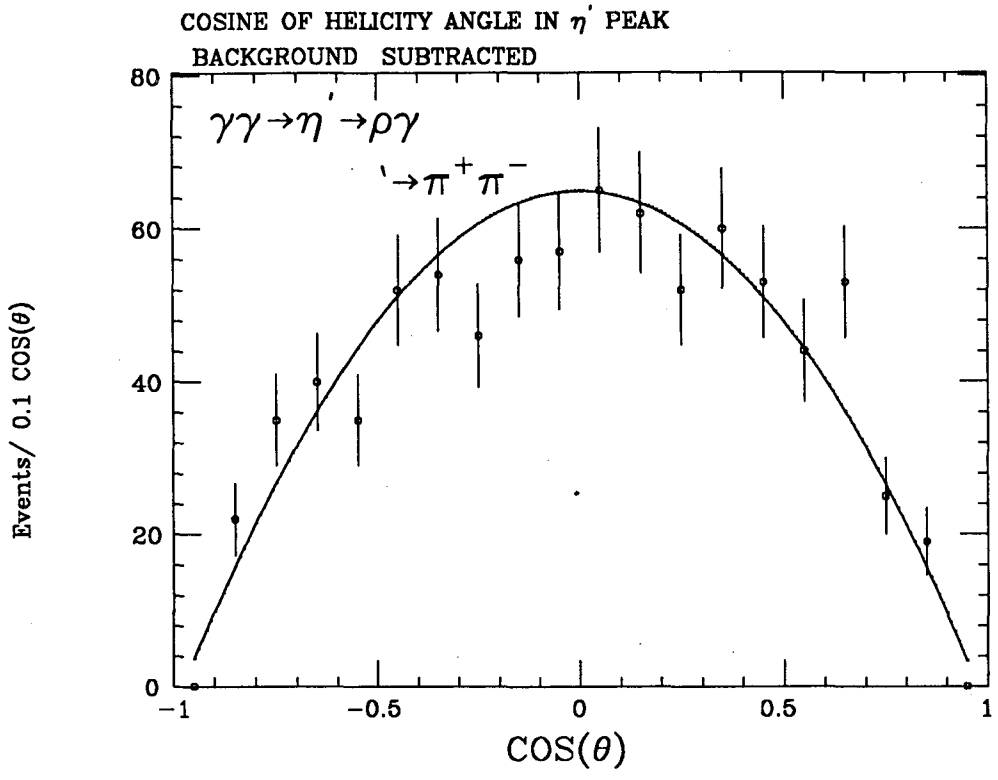

Figure 5.6 *Cosine of helicity angle of events in the η' mass peak, background subtracted*

background is strongest where the desired signal is weakest.

The result of the above cuts is shown in Figure 5.7. The fit to the $\pi^+\pi^-\gamma$ mass was done using 4 fitting functions. The $a_2(1320)$ background peak (described below) was fit with a single gaussian whose mean and width were set by a fit to Monte Carlo simulated events. It was found that for the η' a single gaussian could not give a fit to the Monte Carlo simulated data with a reasonable confidence level. So the η' peak was fit with two gaussians, whose width and mean also were fixed by a fit to Monte Carlo data. The volume of Monte Carlo data generated for $\eta' \rightarrow \rho\gamma$ gave about 5 times the number of events in the peak as the real data, putting tight constraints on the fitting function widths and positions. The fitting program constrained the ratio of the heights of the two gaussians used in the η' fit to be fixed by Monte Carlo simulated data. The remaining background was fit by a 4th degree polynomial. The resulting fit to the real events gave a confidence level of about 15%.

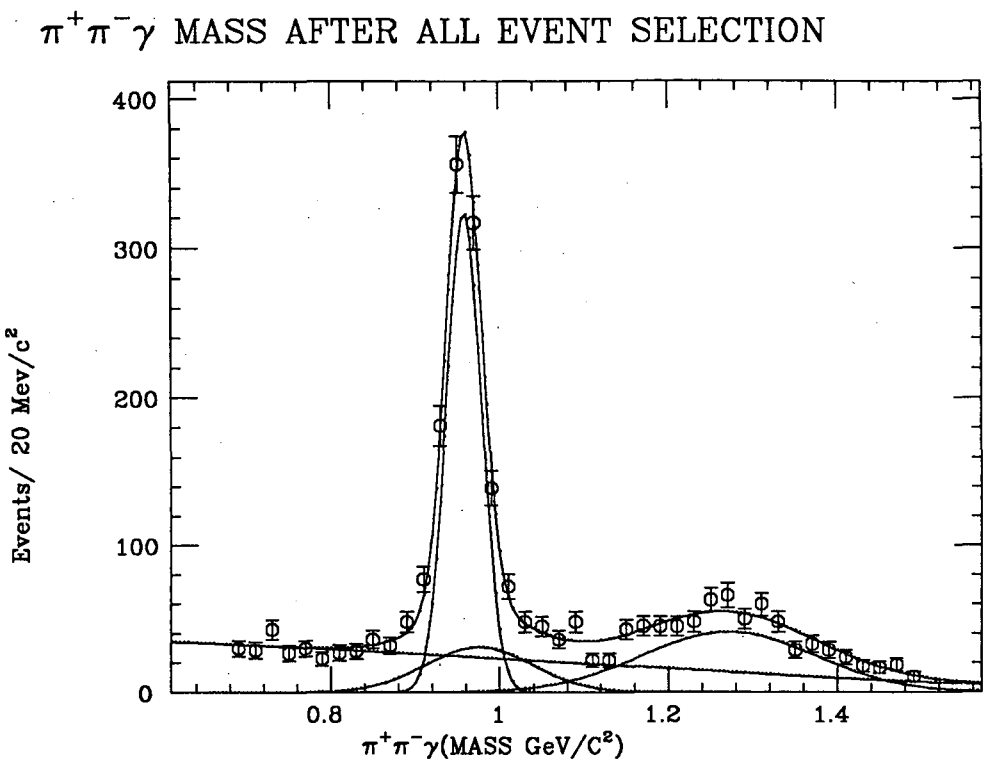

Figure 5.7 *$\pi^+\pi^-\gamma$ mass after all $\eta' \rightarrow \rho\gamma$ cuts The straight slanted line is a fit to the overall background, the gaussian centered at about 1250 MeV/c^2 is a fit to the $a_2(1320)$ part of the background. The η' mass peak is fit using two gaussians which have centers near 958 MeV/c^2 . The sum of all fitting functions is also shown*

The π^+ π^- mass for events in the η' peak region in Figure 5.8 shows a clear ρ peak. A small excess of events over the Monte Carlo simulation's prediction can be attributed to events in the background under the η' peak in Figure 5.7.

5.2 BACKGROUNDS FOR $\eta' \rightarrow \rho\gamma$ EVENTS

Events from other sources may be misidentified as $\eta' \rightarrow \rho\gamma$.

5.2.1 Background from annihilation: $e^+e^- \rightarrow \gamma^* \rightarrow$ (two prongs)

Events created by e^+e^- annihilation must be in a charge conjugation = -1 state whereas two-photon events must be in a charge conjugation + state, but annihilation events can still be a background to two-photon events, if some of the final state particles are not seen or misidentified.

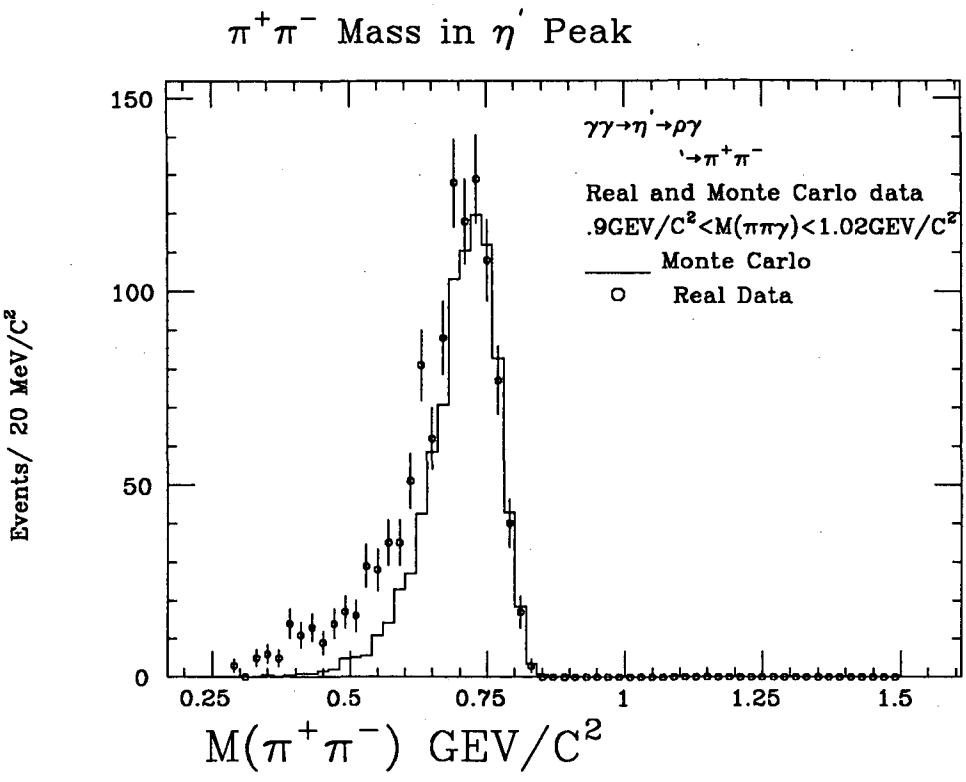

Figure 5.8 *π^+ π^- mass of events in the η' mass peak*

Fortunately there is a very effective way to reduce this annihilation background. In annihilation events the full beam energy is used to create the final state. In two-photon events the two-photon flux drops rapidly as the energy in the $\gamma\gamma$ center of mass increases. If we require that the observed energy be a small fraction of the beam energy, in this case 40%, we exclude almost all of the annihilation events.

A plot of the energy for all charged tracks in real events shows a broad peak near the available beam energy (29 Gev), this peak is the annihilation background and has a rapidly decreasing tail that extends down to energies typical of two-photon events (see Figure 5.9). The size of the annihilation tail in the two-photon energy range of interest ($W < 40\%$) indicates that this background is no larger that .4% relative to two-photon events. Additional kinematic and identification cuts reduce this even further.

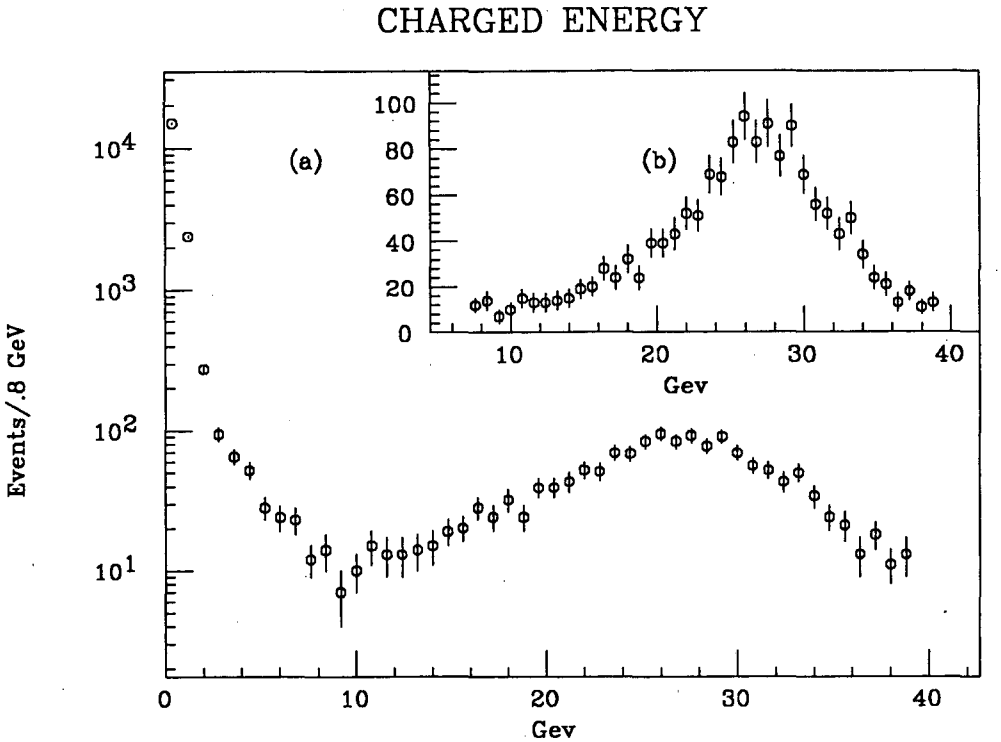

Figure 5.9 *Total energy of all charged tracks in an event after initial charged track quality cuts. (a) energy range 0 to 40 Gev (b) energy range showing the annihilation background peak*

5.2.2 *Background from Bremsstrahlung in the Detector*

Some events which have only 2 charged particles in their final state may look like they are $\pi^+\pi^-\gamma$ events when one of the charged particles undergoes a hard bremsstrahlung while traversing the material that makes up the detector. This process is dominated by events of the form $e \underbrace{\rightarrow}_{Detector} e\gamma$ since the probability of a particle bremsstrahlung increases rapidly as a particle's rest mass decreases.

It is possible to separate these background events from other events involving a single gamma by making use of the small track radius in the drift chamber of the low momentum tracks typical of two-photon events. When a charged particle radiates in a material the angle that the produced gamma makes with the initial direction of the charged particle tends to be small. The path of a charged track originating from the interaction point is bent by the detector's magnetic field so that

bremsstrahlung produced gammas tend not to point back to the interaction point . A positively charged track's path is bent clockwise around the beam axis by the magnetic field so that the bremsstrahlung gammas produced tend to have directions rotated clockwise relative to the track's momentum at the interaction point . For a negatively charged track the reverse is true, the bremsstrahlung gammas tend to be produced in a direction that is rotated counterclockwise to the track's momentum at the interaction point . If we multiply the difference in ϕ angle of the charged track momentum to the gamma's momentum times the sign of the charge of particle producing the bremsstrahlung gamma, we obtain a quantity that is negative for particles of either charge sign. If we histogram all events passing the final selection cuts except the cut on the helicity angle, the difference in angle between the gamma direction and the momentum of the closest charged track momentum in the X–Y plane times the charge of the track we see a distinct peak near zero (Fig. 5.10). The peak is not symmetrical around zero but is shifted toward negative values, proving that most of the gammas in the peak are coming from bremsstrahlung in the detector material.

It turns out that these bremsstrahlung gamma events are almost totally removed by the cut on the helicity angle designed to remove final state radiative gamma background events. This is verified in both real and Monte Carlo data by looking at the effect of the helicity cut on events in the detector bremsstrahlung peak seen in Figure 5.10 .

5.2.3 The reconstruction of $a_2 \rightarrow \rho\pi$ as a background

The decay process $\gamma\gamma \rightarrow a_2(1320) \rightarrow \rho^{\pm}\pi^{\mp}; \rho^{\pm} \rightarrow \pi^{\pm}\pi^0; \pi^0 \rightarrow \gamma\gamma$ when one of the gammas is not seen by the detector gives the observed final state of $\pi^+\pi^-\gamma$ and so is a background when looking at the decay mode $\eta' \rightarrow \rho^0\gamma; \rho^0 \rightarrow \pi^+\pi^-$.

The $a_2(1320)$ can be seen in Figure 5.7 as a broad gaussian on top of a polynomial fit to the background. The gaussian fit to the $a_2(1320)$ is centered at about 1270 MeV/c^2, considerably lower than the accepted mass of the $a_2(1320)$ of 1318 MeV/c^2. The lower mass is due to the missing gamma in the total invariant mass calculation. The Monte Carlo simulation of $a_2 \rightarrow \rho\pi$ predicts the observed broad $\pi^+\pi^-\gamma$ mass.

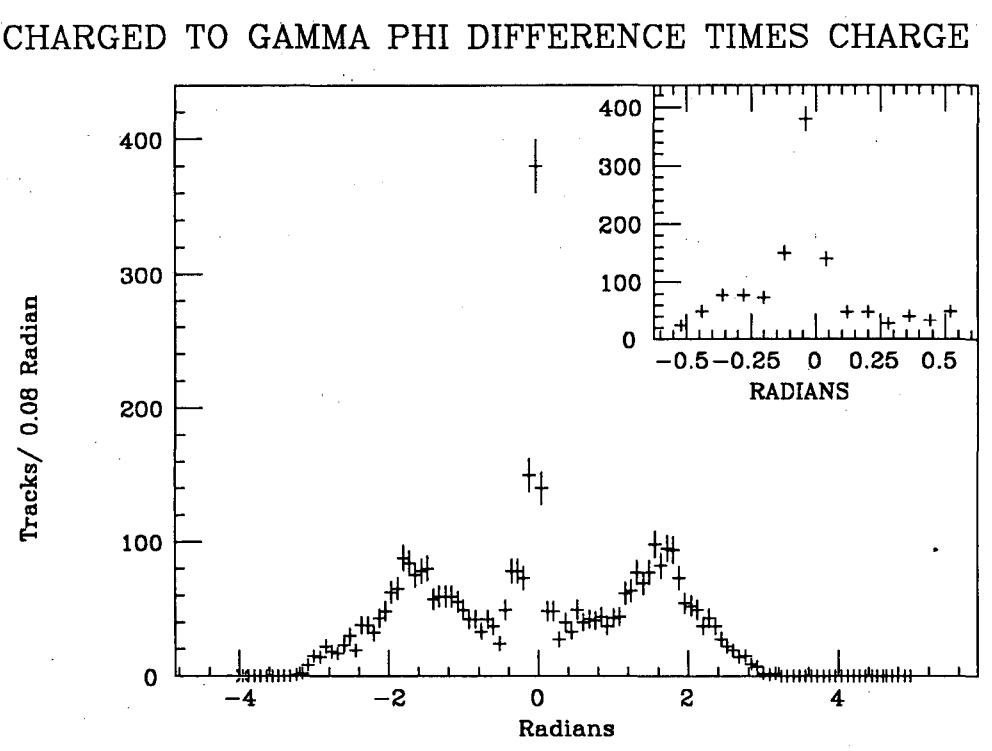

Figure 5.10 *Charged to gamma ϕ angle difference times charge, after all $\eta' \rightarrow \rho\gamma$ cuts except $|\cos\theta_{Helicity}| < .8$*

The broadness of the $a_2(1320)$ is due to the large natural full width (110 MeV/c^2) and additional smearing due to the missing gamma in the observed final state.

If one looks at the π^+ π^- mass of events in the $\pi^+\pi^-\gamma$ mass region of the $a_2(1320)$ (1200 MeV/c^2 to 1450 MeV/c^2) there is a broad but distinct peak at about 950 MeV/c^2 . The $a_2(1320)$ Monte Carlo calculation does not predict this peak (see Figure 5.11). I found that the π^+ π^- mass could be fit using a polynomial whose shape was set by a fit to the Monte Carlo simulation plus a gaussian. Because of the kinematics of the $a_2 \rightarrow \rho\pi$ decay the π^+ π^- mass is anti-correlated to the gamma energy of the observed gamma. The $a_2(1320)$ background comes form the decay $a_2(1320) \rightarrow \rho^{\pm}\pi^{\mp}; \rho^{\pm} \rightarrow \pi^{\pm}\pi^0$;$\pi^0 \rightarrow \gamma\gamma$. If the $\rho^{\pm}$ decays so that the $\pi^{\pm}$ is emitted in a direction with a momentum component opposite to the $\rho^{\pm}$ momentum in the $a_2(1320)$ center of mass (CM), the difference in momenta between the $\pi^{\pm}$ and the $\pi^{\mp}$ is smaller and so the π^+ π^- invariant mass is smaller than the case where the

$\pi^{\pm}$ is emitted in a direction with a momentum component in the direction of the $\rho^{\pm}$ momentum. The π^0 from the $\rho^{\pm}$ decay has a momentum opposite to the $\pi^{\pm}$ in the $\rho^{\pm}$ CM frame so that the π^0 momentum in the $a_2(1320)$ CM frame is larger when the π^+ π^- mass is smaller and the reverse. We only see one of the γ's from the decay $\pi^0 \rightarrow \gamma\gamma$ but the energy of the observed γ tends to be larger if the π^0 has a larger momentum in the $a_2(1320)$ CM frame.

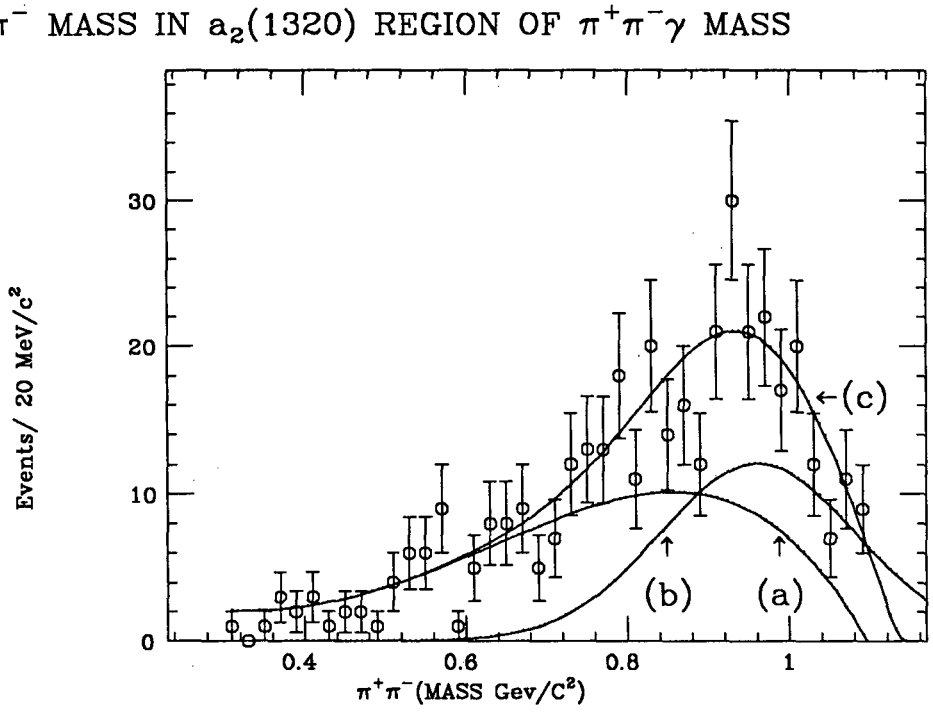

Figure 5.11 *π^+ π^- mass in $a_2(1320)$ region of the $\pi^+\pi^-\gamma$ mass (a) Fit to the Monte Carlo prediction. (b) Fit to remaining background. (c) sum of both fitting functions.*

Since there are more background gammas as gamma energy decreases, $\pi^+\pi^-\gamma$ masses in the $a_2(1320)$ region coming from background events are more likely to be formed by a low energy background gamma and a pair of charged particles whose π^+ π^- invariant mass is large (here we assume they have the rest mass of charged pions). Thus the 950 MeV/c^2 π^+ π^- mass peak is due to a low energy gamma background. The fit to signal and background for the π^+ π^- mass was consistent with the fit to the signal and background in the $a_2(1320)$ region of the $\pi^+\pi^-\gamma$ mass.

In addition to the background to the final state $\pi^+\pi^-\gamma$ from the $a_2(1320)$, the decay of the $\pi_2(1680)$ produces background to $\pi^+\pi^-\gamma$ when it decays by $\pi_2(1680) \rightarrow f^0\pi^0$; $f^0 \rightarrow \pi^+\pi^-$. The $\pi_2(1680)$ has recently been seen in two-photon collisions [18] , [19]. The fit to the $a_2(1320)$ matches well with the Monte Carlo prediction for mass and width, so that the $\pi_2(1680)$ is not a problem when measuring the $a_2(1320)$ two-photon width, but may add to the $\pi^+\pi^-\gamma$ high mass background.

5.2.4 Background reduction by particle identification

The final state of $\pi^+\pi^-\gamma$ can be simulated by other types of particle interactions that involve two charged tracks and one or more gammas.

Backgrounds other than the radiative QED $e^+e^-\gamma$ discussed in section 5.1.2 can contribute. These other background events come from a combination of feed down (not seeing all the final state particles) and particle misidentification.

In Figure 5.7 we have fit the remaining background to a polynomial. There is little problem in fitting this background since it is distributed over a large $\pi^+\pi^-\gamma$ mass range and is distinctly separable from the η' and $a_2(1320)$ peaks.

We would like to have an idea of the percentage of particle types that make up this background. The low momentum of most of these tracks makes particle identification difficult with the Liquid Argon calorimeter for momenta of below about 600 MeV/c. Only at higher momenta do electrons and pions deposit energy in the calorimeter layers in a way that allows for good pion electron particle separation using an algorithm like Mark Nelson's (Ref. 20). Also the usual way of identifying muons using the muon chambers to find particles that pass through the Liquid Argon calorimeter and the flux return iron is not useful below momenta of about 600 MeV/c, since the range of low momentum muons is limited.

Unlike the above identification methods, Time of Flight identification improves at lower momenta and is a more direct form of particle identification. The rest mass of a particle and the error in measuring this mass are given by:

$$m = \frac{p}{c}\sqrt{\frac{1}{\beta^2} - 1} \tag{5.1}$$

$$\Delta m \approx \left(\frac{2p^2}{mLc}\right) \Delta t \tag{5.2}$$

where:

L = the length of the track in the Drift Chamber

m = the rest mass of the particle

p = the momentum of the particle

Δm = the error in measuring the mass

Δt = the error in measuring the Time of Flight

An estimate of the Time of Flight resolution for the Mark II detector using Equation 5.2 gives an error in mass resolution of about 30 MeV/c^2 at p=150 MeV/c and 60 MeV/c^2 at p=200 MeV/c, this assumes a time resolution of 400 psec.

It is difficult to make much more than a crude estimate of the fractions of pions,muons and electrons in the remaining background. The pions and muons cannot be easily separated for momenta much above 200 MeV/c. A look at the Time of Flight masses in the momentum region below 150 MeV/c and at $\pi^+\pi^-\gamma$ masses below the η' peak, shows a significant fraction of muons in the back ground events (see Figure 5.12). The muon background comes predominately from two-photon QED muon events and pion decays. Figure 5.12 does not show the mass range typical of electrons, but the electron background is roughly 10%. The low fraction of remaining electron background after all cuts can be explained by the Time of Flight cut made on β vs momentum which removes the largest part of the electron background at low momentum.

A better knowledge of these background events requires the development of Monte Carlo programs to simulate them. This is not necessary for an accurate measurement of the two-photon width however.

5.3 SYSTEMATIC ERROR IN $\Gamma_{\eta'\to\gamma\gamma}$ FOR $\eta' \to \rho\gamma$

Because we cannot simulate or measure reality perfectly, systematic error is introduced into two-photon width measurements.

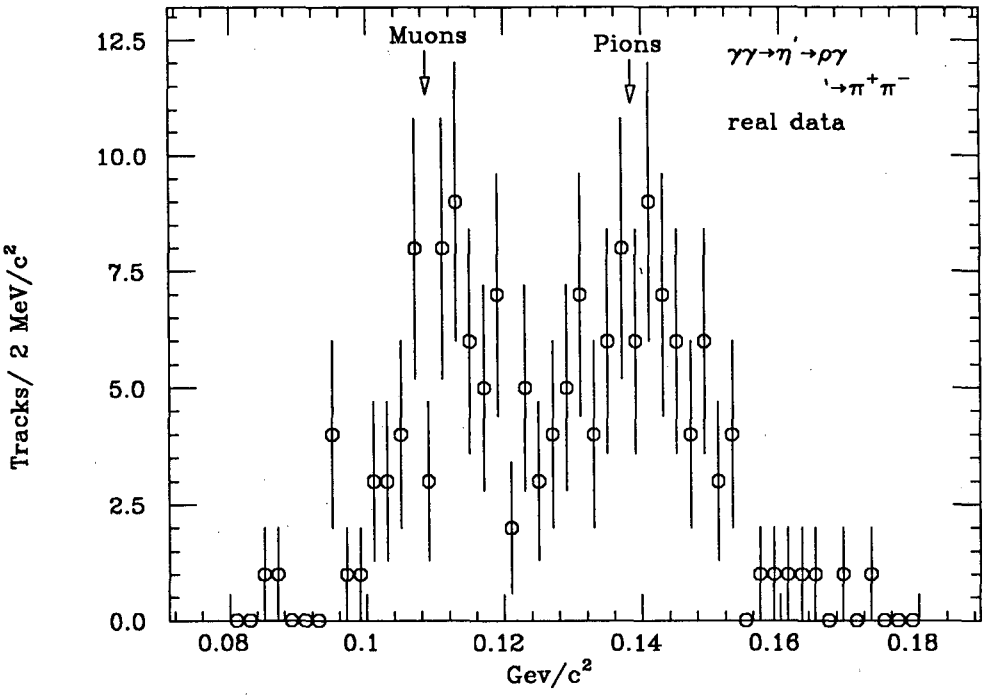

Figure 5.12 *Time of Flight mass in $\pi^+\pi^-\gamma$ mass region below η' peak for charged track momenta < 150 MeV/c*

5.3.1 Systematic error in e^+e^- Luminosity measurement

The e^+e^- luminosity is measured in the Mark II detector by observing Bhabha scattering of the electrons and positrons in the PEP storage ring, allowing us to find the integrated luminosity accumulated during each PEP run. The QED calculations necessary to convert the observed number of Bhabha scattered electrons and positrons to an integrated luminosity can be done with great precision so that the systematic error in the luminosity is almost totally due to the systematic error in the knowledge of the efficiency of the luminosity monitor.

This systematic error has been estimated at about 5%. [21] The estimate was based on a comparison of the luminosity found with wide angle bhabhas and the luminosity found by the luminosity monitor, which has an acceptance at smaller angles relative to the beam axis. The most recent work done to understand the systematic errors in the PEP luminosity claims to improve the error estimate to 1%,

by using large angle Bhabhas. [22] The corrections for the luminosity from Reference 22 are applied in calculating the two-photon widths,but to be conservative we will quote the systematic error of 5% in the integrated luminosity from Reference 21.

5.3.2 Systematic error in Drift Chamber tracking efficiency corrections

The Drift Chamber efficiency for finding single tracks has changed considerably over the PEP running from which our data is taken. Corrections for Drift Chamber efficiency have been found in connection with other data analysis. [23] The tracking efficiency was found to be independent of track momentum, angle and track multiplicity. This tracking inefficiency was found for events with a large number of charged tracks, so the trigger requirements were redundantly satisfied. The tracking efficiency is related only to Drift Chamber efficiency at different periods of the PEP data collection. The correction is estimated to introduce no more that about 3% systematic error to the two-photon width calculations done here.

5.3.3 Systematic error in the background subtraction

The number of events found in the η' and $a_2(1320)$ peaks for the $\pi^+\pi^-\gamma$ mass distribution is not only subject to statistical errors, but also changes with the fitting method.

To find the sensitivity of the width to the fit method three methods were tried. When a fit parameter is fixed it is set equal to the value found by a fit to Monte Carlo events. The fitting methods for the η' peak fitting gaussians were:

1) Fix: The ratio of heights,center positions,sigmas

2) Fix: The ratio of heights only

3) Fix: The center positions only

For the η' peak the largest variation with fitting method is 2.7%.

The height of the gaussian fitting the $a_2(1320)$ peak is effected by the fits to the background and the η' peak. The largest variation with fitting method for the $a_2(1320)$ peak is 17%.

5.3.4 Systematic error due to Monte Carlo simulation

For this decay mode the simulation of the Liquid Argon calorimeter efficiency is the most important. This is due to the low energy spectrum of gammas in the $\eta' \rightarrow \rho\gamma$ decay. About 36% of the gammas in the signal events have gammas with energies below 200 MeV (see Figure 5.13). In this energy range the detection efficiency is changing rapidly. To make the simulation of gammas as accurate as possible Monte Carlo events were generated using the EGS electromagnetic shower program.

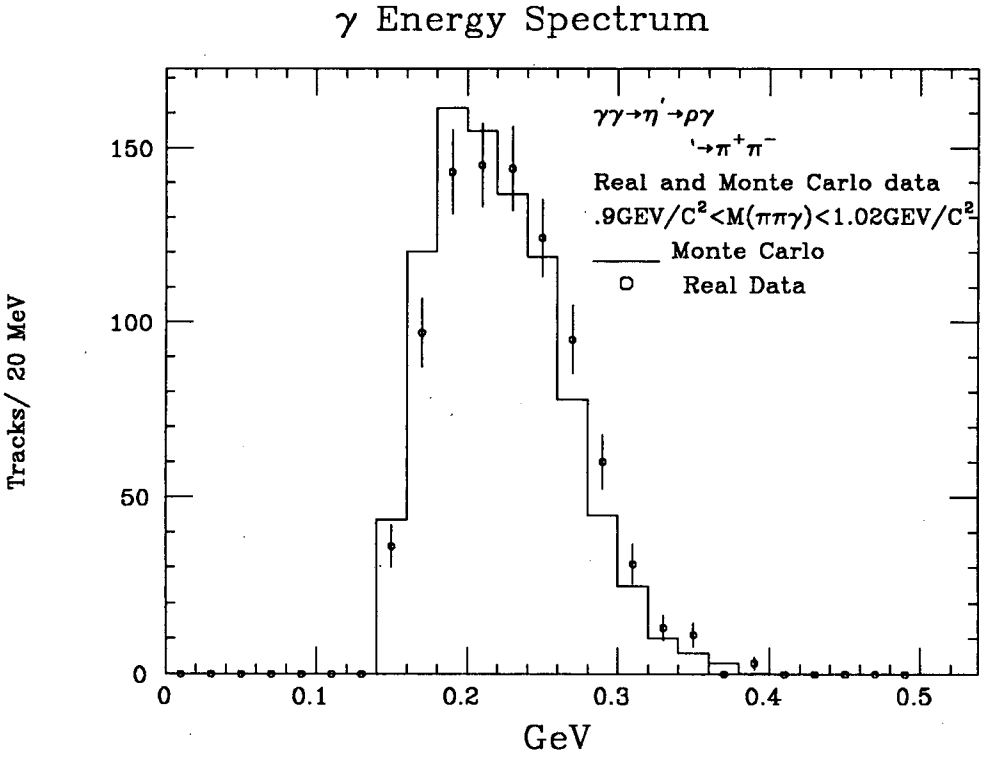

Figure 5.13 *gamma energy of $\eta' \rightarrow \rho\gamma$ Monte Carlo events and real events, in the η' peak region*

The Monte Carlo simulation's efficiency was compared to beam test data, the beam test data matches within statistical errors for gamma energies greater than 200 MeV. Comparison of efficiencies below 200 MeV suggest a systematic error of 10% in the efficiency due to Monte Carlo simulation of the Liquid Argon calorimeter.

In addition to the systematic error due to the Liquid Argon we must consider how the efficiency of the endcaps for finding gammas affects the overall width calculation.

We discard events with more than one gamma passing the initial gamma quality cuts. The Monte Carlo calculation shows that of events discarded for having more that one gamma that only 5% of the events have endcap gammas. The percentage of events having greater than one gamma is only 2.9%; thus, the endcap gammas have only a .15% effect on the width at most.

An estimate of endcap efficiency can be obtained by looking at the $cos(\theta)$ of detected gammas for events that pass all cuts to be in the η' peak, where θ is the angle the photon direction makes with the beam axis. With the assumption of continuity across the Liquid Argon to endcap transition region, the real data shows about a factor of 2 greater efficiency for detecting gammas in the endcap than the Monte Carlo calculation predicts. A factor of 2 increase in endcap efficiency would only increase the two-photon width by .15% . Rejecting events with detected photons in the endcaps is an excellent way to remove background with a systematic error of only about +.15%.

Trigger efficiency corrections

The trigger efficiency and its systematic error are discussed in section 8.2.4 . The trigger efficiency correction for the $\eta' \rightarrow \rho\gamma$ decay mode is about 8%. The systematic error introduced is estimated at no more than 5%.

5.4 Results

The results of all four width measurements are summarized in table 8.2 . The measured decay widths for these decay modes are:

$$\Gamma_{\eta' \rightarrow \gamma\gamma} = 5.26 \pm \underbrace{.37}_{statistical} \underbrace{\pm.68}_{systematic} \; KeV$$

$$\Gamma_{a_2 \rightarrow \gamma\gamma} = 1.17 \pm \underbrace{.15}_{statistical} \underbrace{\pm.25}_{systematic} \; KeV$$

Chapter 6. Event reconstruction for $\eta' \rightarrow \eta\pi^+\pi^-; \eta \rightarrow \gamma\gamma$

This chapter will describe the reconstruction of two-photon events with the final observed particles $\pi^+\pi^-\gamma\gamma$.

6.1 THE RECONSTRUCTION OF η' EVENTS

In describing the cuts used for reconstructing $\eta' \rightarrow \eta\pi^+\pi^-; \eta \rightarrow \gamma\gamma$ events we will concentrate on additional cuts and reconstruction techniques other than those general cuts already described in section 5.1.1 .

Single track P_t cut

The charged track's transverse momentum , along with the detector magnetic field strength, determines the diameter of the helical path that a charged particle follows in the detector. For an event to trigger, the diameter of this helical path must be greater than the distance from the interaction point to the Time of Flight counters, assuming that the track originated at the interaction point . The efficiency for finding tracks with P_t 's below 100 MeV/c drops rapidly, but the Monte Carlo calculation does not show the same drop in efficiency. This prompts us to require a P_t greater than 90 MeV/c for each charged track in the reconstruction program. We also explicitly correct the Monte Carlo simulation for the trigger efficiency. (See Chapter 8)

The minimum single charged track P_t cut and trigger efficiency correction are very important for this decay mode, since the decay $\eta' \rightarrow \eta\pi^+\pi^-$ has only a small amount of energy left to give momentum to its decay products after subtracting the rest mass energy of the final particles. The surplus energy or Q for this decay is only 129 MeV. This limits the momentum of any decay product to 231 MeV/c in the η' center of mass and so limits the π's P_t since most of the η' s are created with the near zero P_t characteristic of untagged two-photon events. (See Figure 6.1) The total momentum of the decay products is typically higher in the laboratory frame,

despite the low Q for the decay, because the created η' can have a large momentum along the beam axis.

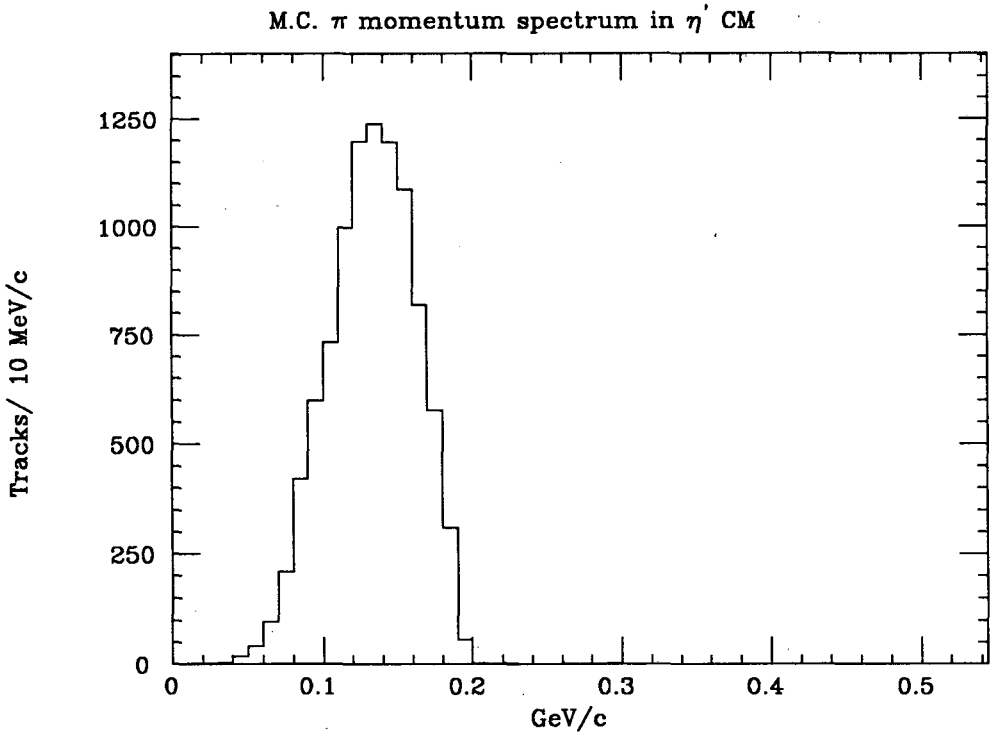

Figure 6.1 *π momentum in the η' center of mass for Monte Carlo simulated events*

For the Monte Carlo calculation to correctly find the efficiency for this decay mode it is crucial that the loss of efficiency at small P_t 's be accounted for correctly. The trigger correction to the Monte Carlo calculated efficiency for this decay mode is 33% and is the largest trigger correction for the decay modes considered in this thesis. The smaller single track P_t of the two tracks is shown for events in the η' peak region in Figure 6.2 . The Monte Carlo simulation does not match the real data well at low P_t , since the Monte Carlo prediction in the plot has not been corrected for trigger efficiency.

Particle Identification

The charged particle identification is done by the Time of Flight system, since the TOF identification is best at the low momenta typical of this decay mode. The

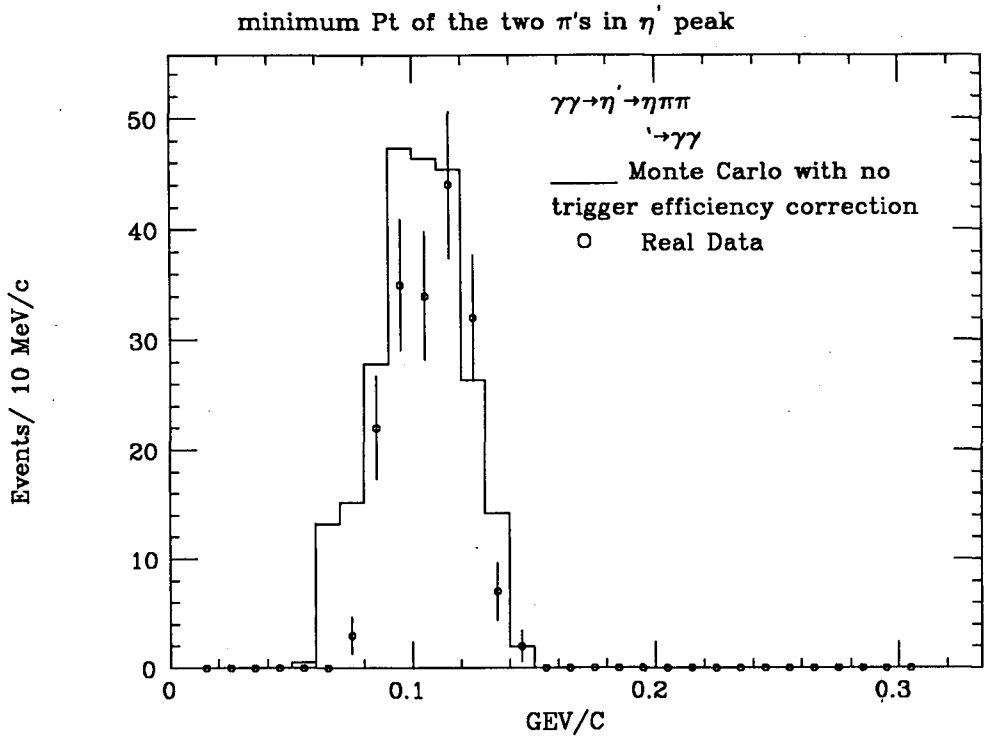

Figure 6.2 *Smallest single track P_t of the two π's for events in η' mass peak region*

other established methods of particle identification such as using the Liquid Argon calorimeter energy deposition pattern and Muon chamber identification, are not reliable at low momenta and are not modeled well by the Monte Carlo detector simulation program.

Rejection of non-pions is done by cutting on a set of Time of Flight weights that reflect the probability that a particle is a pion, kaon, proton or deuteron. The TOF identification weights are found by comparing the measured Time of Flight to the Time of Flight for a given particle mass hypotheses. The χ^2 of the fit to the mass hypothesis is converted to a weight proportional to probability that the measured Time of Flight fits the mass hypothesis. [24] The final TOF weights for each hypothesis are found by dividing the weight for the specific mass by the sum of all other weights.

The separation of pions and electrons is handled separately by finding a weight that compares the pion to the electron hypotheses only. The Fortran variable names

Table 6.1 *The TOF particle identification weight for different mass hypotheses*

Weight name	TOF Mass hypothesis
WTPI	weight for pion
WTK	weight for Kaon
WTP	weight for proton
WTEPI	weight for electron in $e - \pi$ hypothesis

given to the TOF weights are listed in Table 6.1 .

To reduce background the following event cuts are made on charged tracks:
(1) Reject event if for either track WTEPI > .9 and the track momentum greater than 280 MeV/c. This cut removes electron background at low momenta where TOF identification can easily distinguish between electrons and pions.
(2) Reject event if for either track WTK >.7,excludes Kaons
(3) Reject event if for both tracks WTP >.7,excludes Protons

6.1.1 Reconstruction of the η for $\eta \rightarrow \gamma\gamma$

While the natural width of the η is only 1.05 MeV we see in Figure 6.3 that measured $\gamma\gamma$ mass for Monte Carlo simulated events is very broadly distributed around the η mass. Most of the real events in Figure 6.3 above a $\gamma\gamma$ mass of 250 MeV/c^2 come from a combinatorial background whose peak shifts as the lowest gamma accepted cut is changed. The normalization of the Monte Carlo events in Figure 6.3 was chosen to represent the number of η's coming from our η' signal events.

If the gamma energies measured by the Liquid Argon calorimeter were used together with the measured pion momenta to find the $\pi^+\pi^-\gamma\gamma$ invariant mass, the mass resolution would be dominated by the relatively poor energy measurement made by the Liquid Argon calorimeter. To overcome the poor energy resolution we make use of the good position resolution of the calorimeters to do a fit to the measured gamma energies and directions assuming that the gammas we are considering come from an

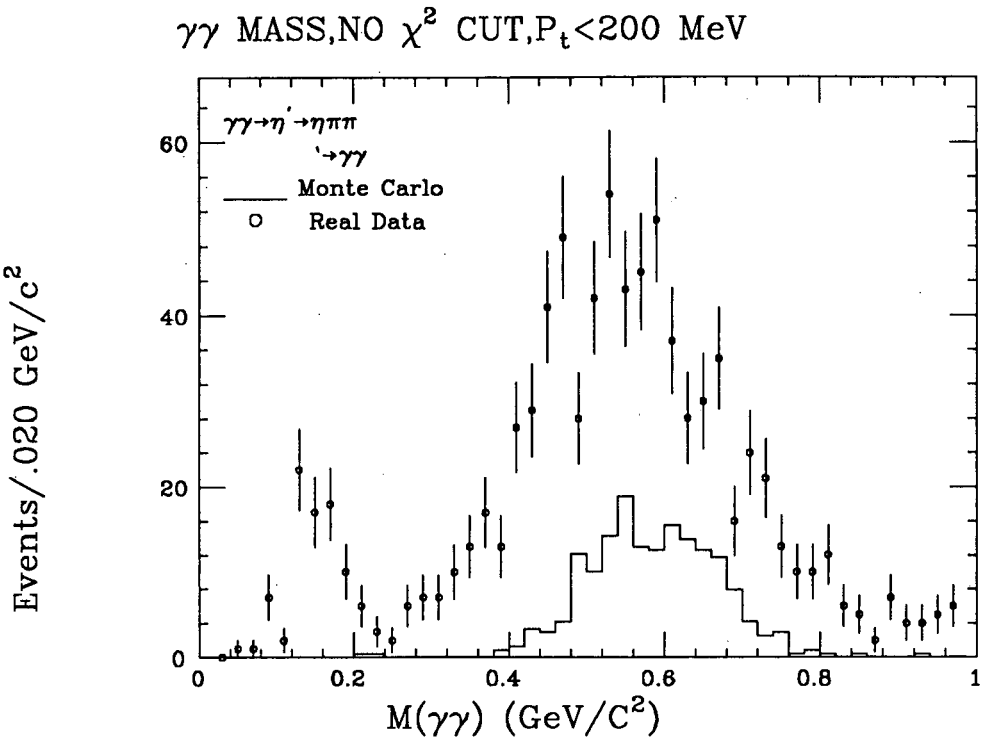

Figure 6.3 *$\gamma\gamma$ mass before fit to $\eta \rightarrow \gamma\gamma$. The Monte Carlo histogram shows expected signal contribution from real η' events*

$\eta \rightarrow \gamma\gamma$ decay. The energy of each gamma is adjusted subject to the constraint that the invariant mass of the gamma pair be equal to the mass of an η . The directions of the two gammas are not varied. The fit has one degree of freedom and is easily done using an analytic expression.

$\eta \rightarrow \gamma\gamma$ fit gamma selection

The gammas used in the fit to the η must be selected in a way that reduces backgrounds. All gammas that pass the initial gamma cuts are paired for consideration in a fit to the η .The gamma cuts used are :

(1) Reject events with endcap gammas. Events with endcap gammas are excluded because of the poor energy resolution of the endcaps.

(2) Require that the gammas in fit have an energy greater than 200 MeV.

(3) The χ^2 of the fit to the $\eta \rightarrow \gamma\gamma$ hypothesis must be less than 5.0 . This corresponds to a fit confidence level of at least 2.5%.

(4) Another visible energy cut is done to reduce annihilation background by adding the energy of the gamma pair being considered to the energy of the charged tracks. The total energy is again required to be less that 40% of the total beam energy.
(5) Both gammas in the pair must be at least 20 cm away from the nearest charged track in the Liquid Argon calorimeter to reduce fakes.
(6) No extra gammas must be present in the event. The selection criterion for extra gammas is described below.
(7) The invariant mass of the two photons in the pair must be greater than 450 MeV/c^2 and less than 750 MeV/c^2 . This cut, determined from Monte Carlo simulation, insures that gamma energies and directions are at least reasonably consistent with the hypothesis that they are form an η decay. Pathological fits that happen have a low χ^2 are thus excluded.
(8) The fit η momentum is added to the momentum of the charged tracks, the $\mid \Sigma \overrightarrow{P_t} \mid$ of the $\eta\pi\pi$ system is required to be less than 200 MeV/c. The $\mid \Sigma \overrightarrow{P_t} \mid$ cut reduces background events from "feed down" where not all the final state particles were seen.

The definition of an "extra" gamma

In deciding what is an extra gamma we do not wish to be too quick to discard events where a gamma has a high probability of being a fake. After two gammas are selected as a trial pair for a fit to the decay $\eta \rightarrow \gamma\gamma$ the remaining gammas are evaluated as to whether they count as extras. The following cuts are use to decide if a gamma is counted as "extra".

(1) A gamma is extra if its energy is greater than 150 MeV and is isolated in its own module, not sharing the same Liquid Argon module with another gamma or charged track.
(2) A gamma is extra if it is at least 20 cm away from any other gamma or charged track and has an energy greater than 200 MeV.
(3) A gamma is extra if it is at least 20 cm away from any other gamma or charged track and has an energy greater than 150 MeV and the tracking program indicates that it shares no more that 5% of its energy with any other electromagnetic shower

in the Liquid Argon calorimeter.

As a check of the effectiveness of the above cuts for extra gammas we can look at the $\mid \Sigma \overrightarrow{P_t} \mid$ of the reconstructed $\eta\pi^+\pi^-$ system, with and without extra gammas found. (See Figure 6.4) Note that Figure 6.4 shows a larger $\mid \Sigma \overrightarrow{P_t} \mid$ for events with extra gammas indicating that not all final state particles are accounted for in the extra gamma events. We may also look at the final $\eta\pi^+\pi^-$ mass distribution with and without an extra gamma found. (See Figure 6.5) Note that there is no η' mass peak for events with extra gammas.

6.2 BACKGROUNDS FOR $\eta' \rightarrow \eta\pi^+\pi^-; \eta \rightarrow \gamma\gamma$ EVENTS

We have already covered some backgrounds that are common to all two-photon events in connection with the $\eta' \rightarrow \rho\gamma$ decay mode. We will mention these again briefly. The backgrounds that are specific to $\eta' \rightarrow \eta\pi^+\pi^-; \eta \rightarrow \gamma\gamma$ will be given full attention.

6.2.1 Backgrounds common to all decay modes

The background from annihilation events is reduced by a cut on the total energy seen in the charged tracks plus the energy of the η found by fitting to the hypothesis $\eta \rightarrow \gamma\gamma$. For the η' events the total energy of the η is only about 40 MeV greater than the η rest mass. The cut is tighter that the cut on the visible charged energy alone, the cut used for the $\eta' \rightarrow \rho\gamma$ decay mode, helping to remove events with unreasonably high energy gamma pairs that happen to pass the χ^2 cut for the fit to the $\eta \rightarrow \gamma\gamma$ hypothesis.

Detector Bremsstrahlung and radiative production of final state gammas is much less of a problem for $\eta' \rightarrow \eta\pi^+\pi^-; \eta \rightarrow \gamma\gamma$ than for $\eta' \rightarrow \rho\gamma$ since two final state gammas must be produced. In order for QED backgrounds to mimic the final state particles of the $\eta' \rightarrow \eta\pi^+\pi^-; \eta \rightarrow \gamma\gamma$ decay mode, both charged particles in the final state must radiate a gamma. Assuming that the probabilities of radiating gammas for both charged tracks are independent, the probability of seeing two gamma final

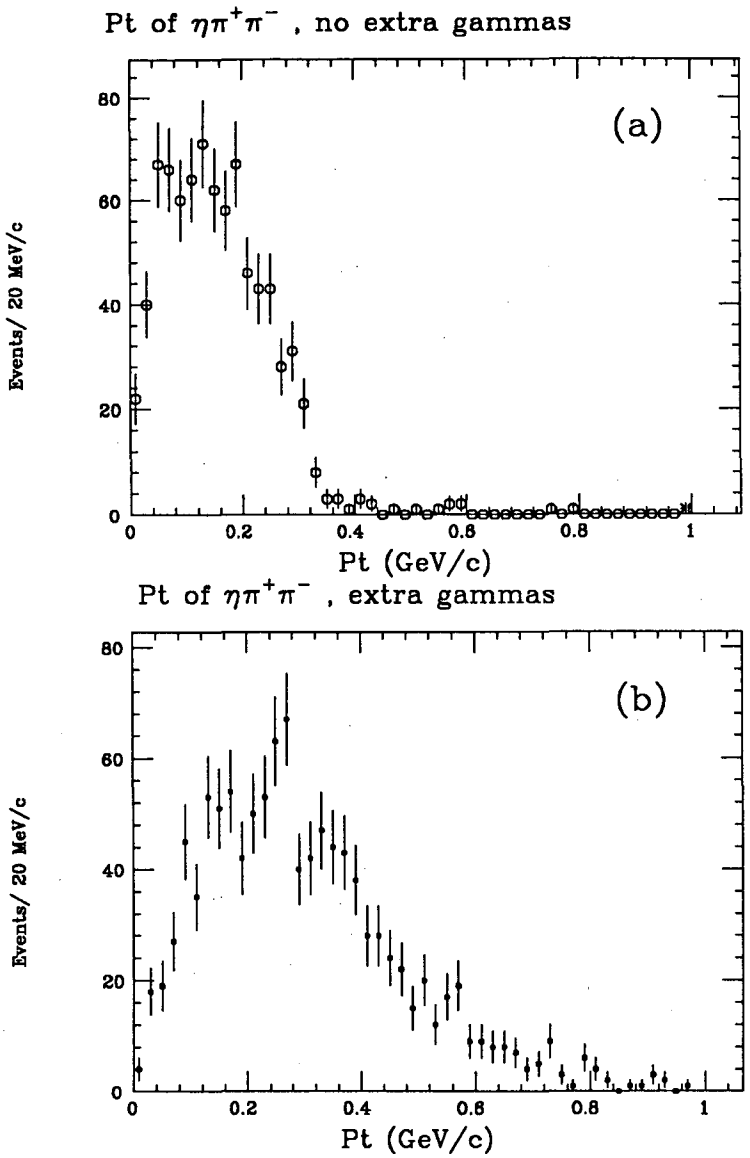

Figure 6.4 *(a) $|\Sigma\overrightarrow{P_t}|$ of $\eta\pi^+\pi^-$ system for events with no "extra" gammas (b) $|\Sigma\overrightarrow{P_t}|$ of $\eta\pi^+\pi^-$ system for events with "extra" gammas*

states is much lower. One would naively expect that each additional radiative gamma would reduce the probability of a radiative event by a factor of $(\frac{1}{\alpha^2})$. A more careful calculation requires a Monte Carlo program to assess the complex details of the two-photon flux, momentum dependent factors and the detector acceptance. Such a Monte Carlo program is no currently available for the Mark II. The radiative two-photon event background presents no serious problem to our measurement of the

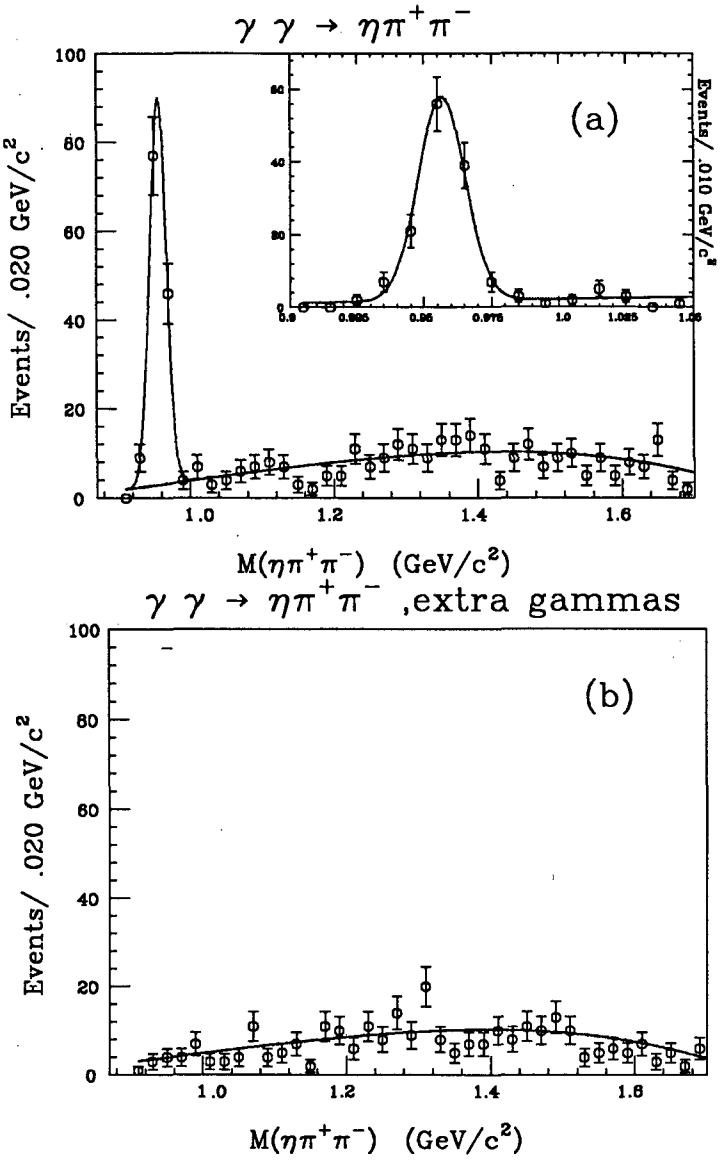

Figure 6.5 *(a) $\eta\pi^+\pi^-$ mass for events with no "extra" gammas (b)$\eta\pi^+\pi^-$ mass for events with "extra" gammas*

η' width however. The radiative background has no mass structure and so can be safely subtracted.

6.2.2 Backgrounds specific to $\eta' \to \eta\pi^+\pi^-; \eta \to \gamma\gamma$

The main difficulties in eliminating background have to do with insuring that we have two and only two real photons in the final state. As mentioned before we have developed criterion for finding extra gammas in events. If an event truly has an extra

gamma we must consider this event as background coming from feed down.

There are in addition to background events removed by the analysis program, backgrounds that require that a human make a judgment as to whether the event is a background event (Hand scanning).

Events in the final $\eta\pi^+\pi^-$ mass histogram were subject to several hand scans. The types of events discarded were:

(1) Events with obvious untracked additional particles in the Drift Chamber , especially low energy tracks. This indicates the presence of unobserved final state charged particles.

(2) Events with obvious cosmic ray tracks. Cosmic ray tracks were easily identified in one event display plots. The most common case involves a high energy cosmic track which crosses the Drift Chamber missing the interaction point leaving hits in the Liquid Argon as it enters and exits. Because the Drift Chamber tracking program only looks for tracks that pass close to the interaction point the energy deposits in the Liquid Argon were classified as coming from two gammas.

(3) False gammas can be found by the tracking program when a track in the Drift Chamber has been poorly tracked. Since the path of the track is poorly known the projected entry point in the Liquid Argon calorimeter may be far enough away from the actual entry position so that the shower found in the Liquid Argon due to the charged track is thought to be due to a photon. A look at the Drift Chamber layer hits (DAZM's) can indicate that the charged track has hard scattered or decayed. The sudden change of direction often makes the fit to the overall Drift Chamber path unreliable.

(4) Events with obvious untracked gamma conversions ($\gamma \rightarrow e^+e^-$) are removed since there is clearly an extra gamma in the event. Gamma conversions are easily identified by the near zero opening angle of the two charged tracks produced, usually at some distance from the interaction point .

The hand scan used to find the two-photon width rejects about 5% of the events in the η' peak mass region. All hand scans are summarized in table 6.2 .

As an indication of the effectiveness of the cuts used to eliminate background events, we can again look at the $|\ \Sigma\overrightarrow{P_t}\ |$ of events in the η' mass peak region. (See Figure 6.6) The excellent agreement between the real data with the Monte Carlo simulation demonstrates that background is not significant. Previously we looked at the $|\ \Sigma\overrightarrow{P_t}\ |$ of all events with no "extra" gammas for all $\pi^+\pi^-\gamma\gamma$ masses (Figure 6.4a).

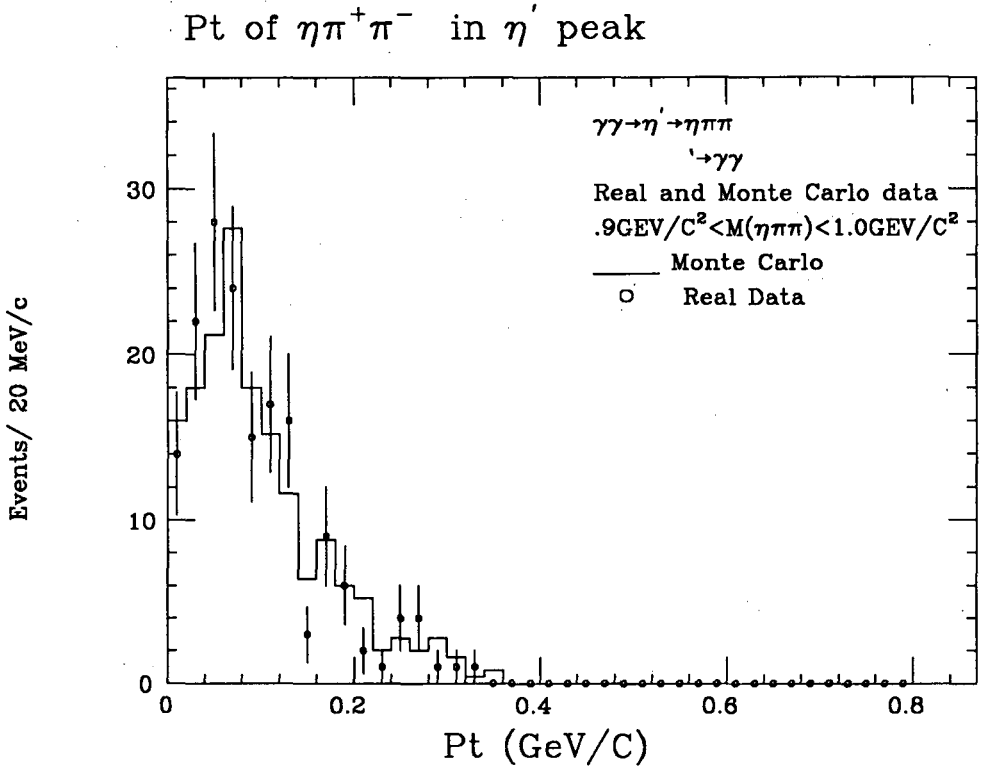

Figure 6.6 *The transverse momentum of the $\eta\pi^+\pi^-$ system for events in the η' mass peak*

6.3 SYSTEMATIC ERROR IN $\Gamma_{\eta'\to\gamma\gamma}$ FOR $\eta' \to \eta\pi^+\pi^-; \eta \to \gamma\gamma$

Some systematic errors that we looked at earlier also apply to the $\eta' \to \eta\pi^+\pi^-; \eta \to \gamma\gamma$ decay mode. In section 5.3.1 we considered the effect of the error introduced in $\Gamma_{\eta'\to\gamma\gamma}$ by the measurement of the e^+e^- luminosity.

In section 5.3.2 we considered corrections for trigger efficiency due to changes in Drift Chamber tracking efficiency. Those corrections are identical for this decay mode since it also has two charged pions in the final state.

6.3.1 Systematic errors due to hand scanning candidate events

To understand the systematic error introduced by the unavoidable subjective judgments in hand scanning events for background, two hand scans were done. Both hand scans were done at times that were months apart. Both hand scans were done while making a conscious attempt at eliminating bias, but as it happened the first was one was done with the desire to maximize the number of events passing and the 2nd was done with the desire to minimize the number of events passing the hand scan.

Using the above two hand scans I constructed 2 sets of events.
(1) Min hand scan: If an event was discarded by either the first or 2nd hand scan it was discarded from this set of events.
(2) Max hand scan: Events were discarded only if discarded from both the first and 2nd hand scan.

As a further estimate of hand scanning extremes more event sets were considered.
(3) Gold plated: Only the cleanest events were kept. Events with more than 2 gammas were discarded even when the extra gammas were consistent with the hypothesis that these gammas were fakes. All the previously mentioned types of background events were also discarded.
(4) All events: All events passed by the analysis program were kept , even the obvious background events.
(5) M.C. events: Monte Carlo events were hand scanned using the same standards as used in the 2nd hand scan.

The change in the two-photon width due to the use of one of the above hand scans is summarized in Table 6.2 .

The changes in two-photon width due to hand scanning methods were found by doing a complete fit to the η' peak and background in the $\eta\pi^+\pi^-$ mass histogram. The fact that the Min hand scan gives a larger two-photon width than the Max hand scan can be accounted for by the details of fitting the η' peak and back ground. This

Table 6.2 *The change in $\Gamma_{\eta' \to \gamma\gamma}$ for different hand scanning methods*

Type of hand scan	Change in $\Gamma_{\eta' \to \gamma\gamma}$
2nd hand scan	0%
Min hand scan	-1.6±9.2%
Max hand scan	-1.8±9.7%
Gold plated	-24.6±8.1%
All events	+5.0±9.7%
M.C. events	+2.0±1.4%

variation is well within the fitting error. A conservative systematic error estimate of hand scan systematic would be +5%, -2% .

6.3.2 Systematic error due to Monte Carlo simulation

Simulation of low P_t trigger efficiency

Because of the low transverse momentum of the charged π's produced in this decay mode, we must also consider the systematic error due to Monte Carlo simulation of the trigger efficiency of low P_t tracks. The trigger efficiency and its systematic error are discussed in chapter 8. The resulting correction to the Monte Carlo simulated efficiency for the $\eta' \to \eta\pi^+\pi^-; \eta \to \gamma\gamma$ decay mode is about 33% . The systematic error introduced is estimated at 4% .

Simulation of gammas in the Calorimeters

The Monte Carlo simulated efficiency for $\eta' \to \eta\pi^+\pi^-; \eta \to \gamma\gamma$ is very sensitive to the correct modeling of the photon interactions in the calorimeters. To estimate the sensitivity to incorrect modeling, the efficiency for observing $\eta' \to \eta\pi^+\pi^-; \eta \to \gamma\gamma$ for Monte Carlo generated using EGS and OVREZY were compared.

EGS is a well know electromagnetic shower simulation program whose results have been verified against real test data (Reference 25). OVREZY is a simulation program that uses sample showers generated using EGS. OVREZY is intended to save

computer time. To save time OVREZY picks a sample shower and uses interpolation in energy and position to produce a shower at the desired energy and position. Unfortunately sample showers generated favor the higher energies produced in annihilation events.

Using OVEREZY has a dramatic effect on the Monte Carlo calculated efficiency. The EGS efficiency is about 70% higher than the OVREZY efficiency. The increased efficiency can be broken down to :

(1) 20% from more gammas passing the initial gamma quality cuts.

(2) 20% due to less scatter in the $\mid \Sigma \overrightarrow{P_t} \mid$ distribution due to a better fit to $\eta \rightarrow \gamma\gamma$ allowing more events to pass the $\mid \Sigma \overrightarrow{P_t} \mid$ of $\eta\pi^+\pi^-$ cut of 200 MeV/c.

(3) 20% from the increase likelihood that if there are more than one pair of gammas, that one of them can be fit to the $\eta \rightarrow \gamma\gamma$ hypothesis with an acceptable χ^2 .

(4) 10% Other differences.

To avoid the systematic errors associated with OVREZY, EGS was used for all the Monte Carlo event simulation in this thesis. To be conservative a $\pm 20\%$ systematic error due to shower simulation in the Liquid Argon seems in order for this decay mode.

Simulation of endcap efficiency

There is another possible systematic error due to the simulation of the endcap efficiency for detecting gammas. The endcaps are more reliable for detecting gammas in that a detected gamma is unlikely to be due to electronic noise, but this says nothing about how efficient the endcaps are. Because an event is rejected for having a detected gamma in one of the endcaps, the simulation of this detection efficiency may introduce error.

To estimate the effect that an error in endcap efficiency in the Monte Carlo simulation would have on the two-photon width, the analysis program was run on Monte Carlo simulated events with and without the veto of events with endcap gammas. No difference in number of events in the final η' peak was found. The events that would be vetoed by the endcaps do not make it to the final histogram. The systematic

error due to endcap efficiency can therefore be neglected. Vetoing events with endcap gammas removes only background.

6.3.3 Systematic errors due to background subtraction

The number of events found in the η' peak varies with fitting method. When a parameter was fixed it was set equal to the value found in a Gaussian fit to the Monte Carlo generated events. Three fit methods were tried:

1) All parameters free.

2) Sigma fixed.

3) Sigma fixed and Center position fixed

The largest variation with fit method was +3.2%. A conservative systematic error would be ±4%.

6.4 RESULTS

The results of all four width measurements are summarized in table 8.2 . The measured decay width of this decay mode is:

$$\Gamma_{\eta' \to \gamma\gamma} = 4.98 \pm \underbrace{.71}_{statistical} \quad \underbrace{\pm 1.10}_{systematic} \; KeV$$

Chapter 7. Event reconstruction for $\eta' \rightarrow \eta\pi^+\pi^-; \eta \rightarrow \pi^+\pi^-\pi^0$, $\pi^+\pi^-\gamma$

This chapter will describe the reconstruction of two-photon events with the final observed particles $\pi^+\pi^-\pi^+\pi^-$.

7.1 THE RECONSTRUCTION OF η' EVENTS

The Mark II detector is exceptional in that its charged trigger is sensitive to charged tracks with transverse momenta as low as 90 MeV/c. The decay mode we are considering produces tracks with P_t s that are almost all less than 200 MeV/c. (see Figure 7.1)

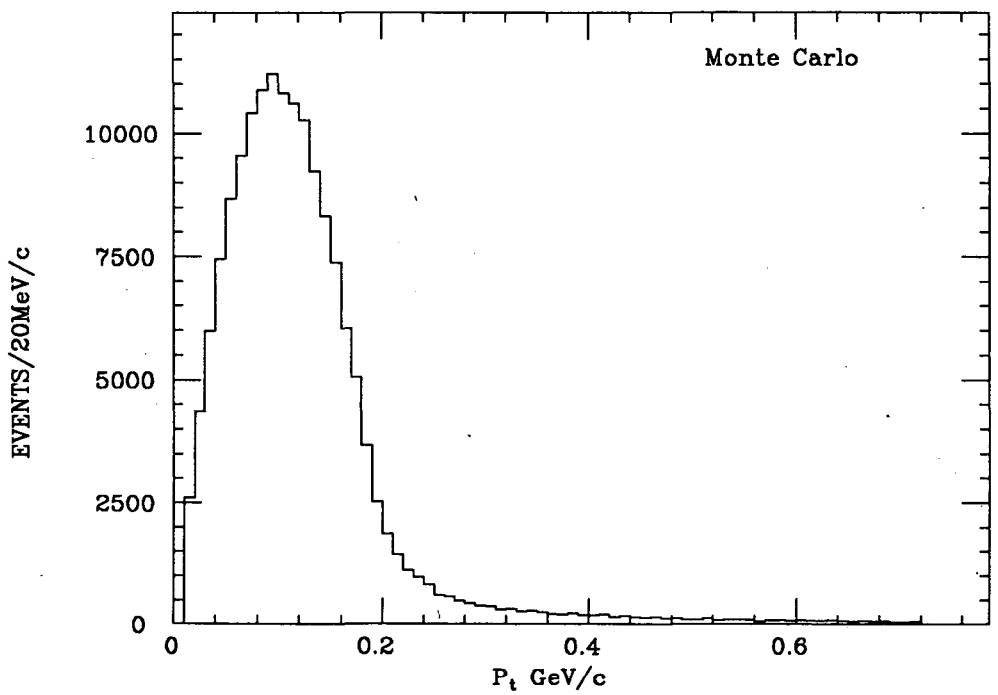

Figure 7.1 *$\pi^{\pm}$ P_t generated by Monte Carlo simulation*

Because this decay mode of the η' has 4 charged particles in the final state, it is not subject to the same kinds of backgrounds considered earlier for the two charged

final state η' decay modes $\eta' \rightarrow \rho\gamma\ ;\rho^0 \rightarrow \pi^+\pi^-$ and $\eta' \rightarrow \eta\pi^+\pi^-; \eta \rightarrow \gamma\gamma$. In adjusting the selection criteria for the $\eta' \rightarrow \eta\pi^+\pi^-; \eta \rightarrow \pi^+\pi^-\pi^0$, $\pi^+\pi^-\gamma$ reconstruction I found that a good signal with relatively low background could be obtained with only the following cuts.

The initial cuts were:

(1) No tagging electrons observed.

(2) The event must be consistent with a primary trigger. Since we have 4 charged tracks in the final state, deciding if an event could have caused a primary trigger is somewhat more complicated. The primary trigger is discussed for 2 charged final states in section 6.1 . For the present decay mode two or more of the charged tracks were required to have a large enough P_t to hit the Time of Flight counters within the fiducial region. More will be said about the correct modeling of trigger efficiency in chapter 8.

(3) The usual charged track visible energy cut to reduce annihilation background was applied.

(4) The total charge of all 4 observed charged tracks was required to be zero. This helps eliminate events where one or more of the charged particles were not observed.

With just the above cuts a clear peak can be seen in a histogram of the 4π invariant mass plot of events. (see Figure 7.2) Because we do not include the contribution to the invariant mass of the π^0 or the γ from the decay of the η, the η' peak in the 4π mass histogram is shifted down in mass from 958 MeV/c^2 to a peak at a mass of about 800 MeV/c^2 .

Note that the above cuts did not involve selection based on observation of gammas by the detector calorimeters. The 4π mass signal is free enough of background events involving neutrals to avoid systematic error introduced into $\Gamma_{\eta' \rightarrow \gamma\gamma}$ by their use in rejection of background events. Further cuts will reduce the background under the η' peak event further.

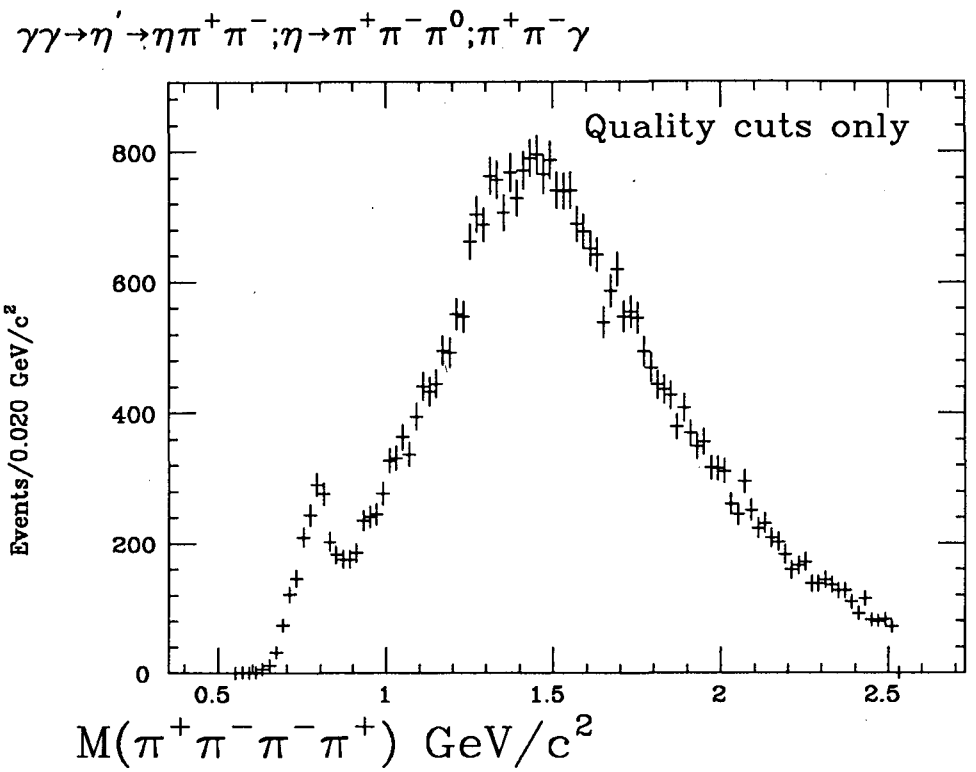

Figure 7.2 *$\pi^+\pi^-\pi^+\pi^-$ invariant mass distribution for events passing "Quality cuts" only*

7.2 BACKGROUNDS FOR $\eta' \to \eta\pi^+\pi^-; \eta \to \pi^+\pi^-\pi^0$, $\pi^+\pi^-\gamma$

We must identify and eliminate specific types of background events to make further progress in background reduction. The following background cuts were made.

7.2.1 QED and other electron backgrounds

Because the desired final state has four charged particles, backgrounds due to QED events are greatly reduced. The direct QED production of four charged prongs is suppressed by the higher orders of α necessary in such Feynman diagrams.

Another way in which QED might produce a four charged particle final state involves radiative QED events with a gamma that pair produces two electrons due to interaction with detector materials.

The gamma conversion background may also come from non-QED sources such as $\eta' \to \rho\gamma$ or any other process producing 2 charged tracks and one or more gammas.

To reduce QED backgrounds and other backgrounds with electrons in the final state two types of cuts are used by the analysis program.

(1) TOF electron cut: Events with any tracks having low momenta and high β are discarded when their β and momentum are within a region of the β-momentum plane where they can easily be identified as electrons. As mentioned in section 5.2.4 TOF particle identification becomes more difficult as track momentum increases. Fortunately the track momenta for this decay mode are low, so TOF identification of electrons is very effective.

(2) e pair from conversion cut: When a gamma converts in a material to form an electron-positron pair the initial momentum direction of the e^+ and e^- are almost the same. This reflects the zero invariant mass of the initial gamma. This angle can be used to reduce conversion background events. Candidate events are required to have an opening angle between all oppositely charged tracks such that $\cos\theta$ is less than .98, where θ is the lab angle made between track momenta.

7.2.2 Backgrounds with K_{short} and $K^{\pm}$

Some production processes involving Kaons (Such as $K^0K^+\pi^-; K^0 \rightarrow \pi^+\pi^-$ and $K^+K^-\pi^+\pi^-$) can produce a four charged final state background.

The K^0 background is reduced by requiring that the invariant mass of all opposite charge combinations be in a range that excludes the K^0 mass of 450 MeV/c^2 $< M_{\pi^+\pi^-} <$ 550 MeV/c^2 . Figure 7.3 shows a distinct peak at the K^0 from $K_{short} \rightarrow \pi^+\pi^-$ as well as a broad shoulder near 770 MeV/c^2 caused by $\rho^0 \rightarrow \pi^+\pi^-$.

The $K^{\pm}$ background is also reduced by requiring that the TOF mass of all tracks with TOF information exclude the $K^{\pm}$ region. The region excluded is 450 MeV/c^2 to 550 MeV/c^2 . Figure 7.4 shows a $K^{\pm}$ mass peak at about 500 MeV/c^2 as well as a π and proton peak. The Time of Flight masses in Figure 7.4 are from all four prong two-photon events before any background cuts have been done.

Once again the low track momenta of events in the η' peak region make TOF mass cuts for $K^{\pm}$ very effective.

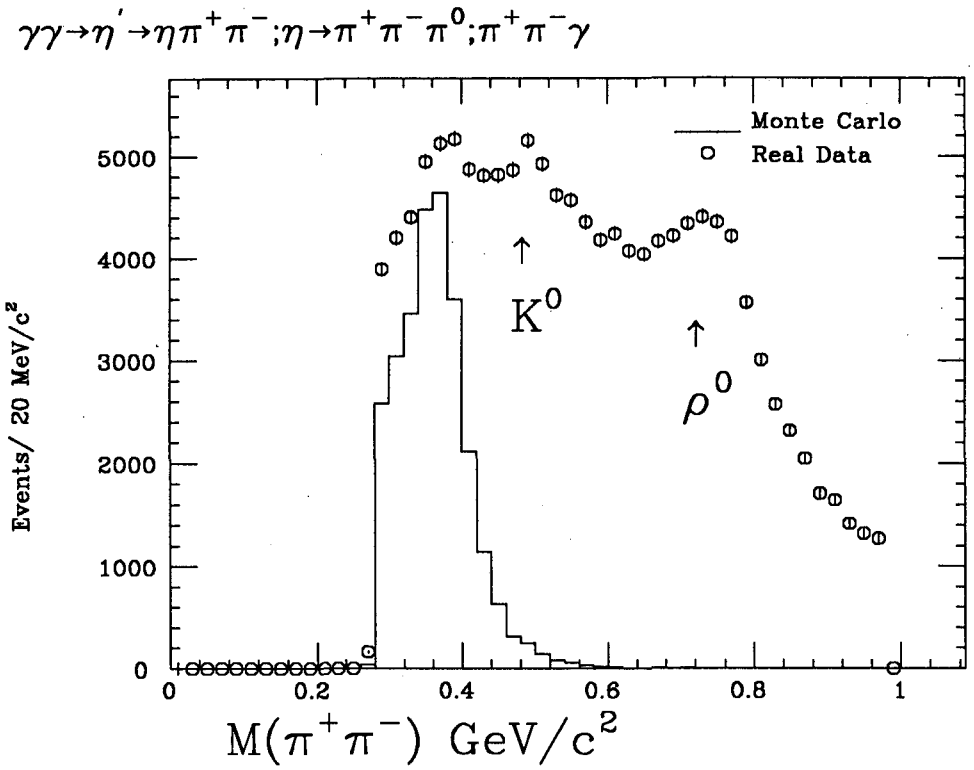

Figure 7.3 *$\pi^+\pi^-$ invariant mass for all oppositely charged track combinations, before background cuts, the corresponding Monte Carlo prediction for the $\pi^+\pi^-$ mass of pions from the η' decay is shown as a solid line.*

7.2.3 Background from $\pi^\pm \to \mu^\pm\nu$ and $\pi^\pm$ scattering

Because of the low momentum of pions produced in the η' decay we are considering, there is a good probability that the produced pions will decay to a muon and neutrino within the detector drift chamber volume. This background is reduced by requiring that the tracking program find a single track fit (track fit is not constrained by the primary vertex position) within a small minimum distance of approach to the beam origin (5 cm radially and 50 cm along the beam axis). This cut also reduces the effect of poorly tracked pions due to scattering within the detector. The single track fit cuts are roughly equivalent to the previous vertex constrained cuts, in that approximately the same fraction of events are removed.

If we keep all the above event cuts, except for the track position cut, we have a 4π mass distribution with 42% more events in the η' peak region when compared

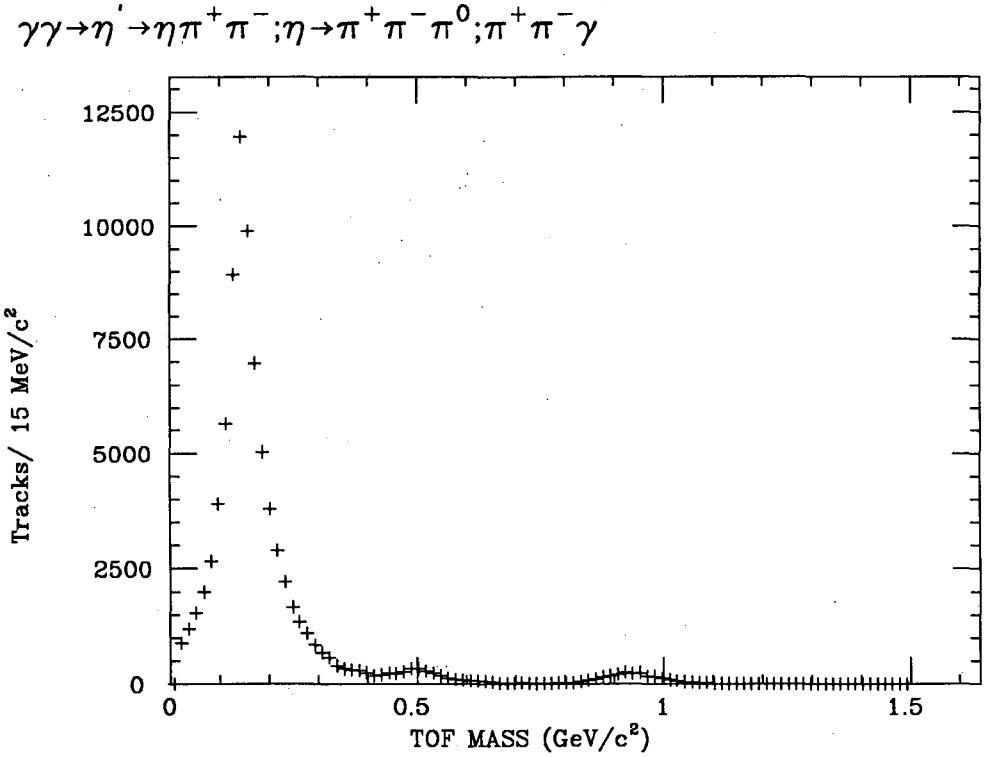

Figure 7.4 *Mass found from Time of Flight of all input four prong events*

to events in the η' peak with no track position cuts. We will not remove the track position cut for events in the final histogram for reasons described latter, even though we would have more events in the η' peak with little increase in background.

7.2.4 Background summary

The 4π mass distribution after all the above cuts is shown in Figure 7.5 .A $\mid \Sigma\overrightarrow{P_t} \mid$ cut is not made, since we know that final state particles are missing. Figure 7.6 shows the $\mid \Sigma\overrightarrow{P_t} \mid$ of all four charged tracks for events in the peak is not peaked at zero because of missing final state particles and matches well with the Monte Carlo prediction of $\mid \Sigma\overrightarrow{P_t} \mid$.

To assess the effectiveness of the Kaon and electron background cuts we can look at the TOF mass and $\pi^+\pi^-$ mass of events in the η' peak region. No significant background is found.

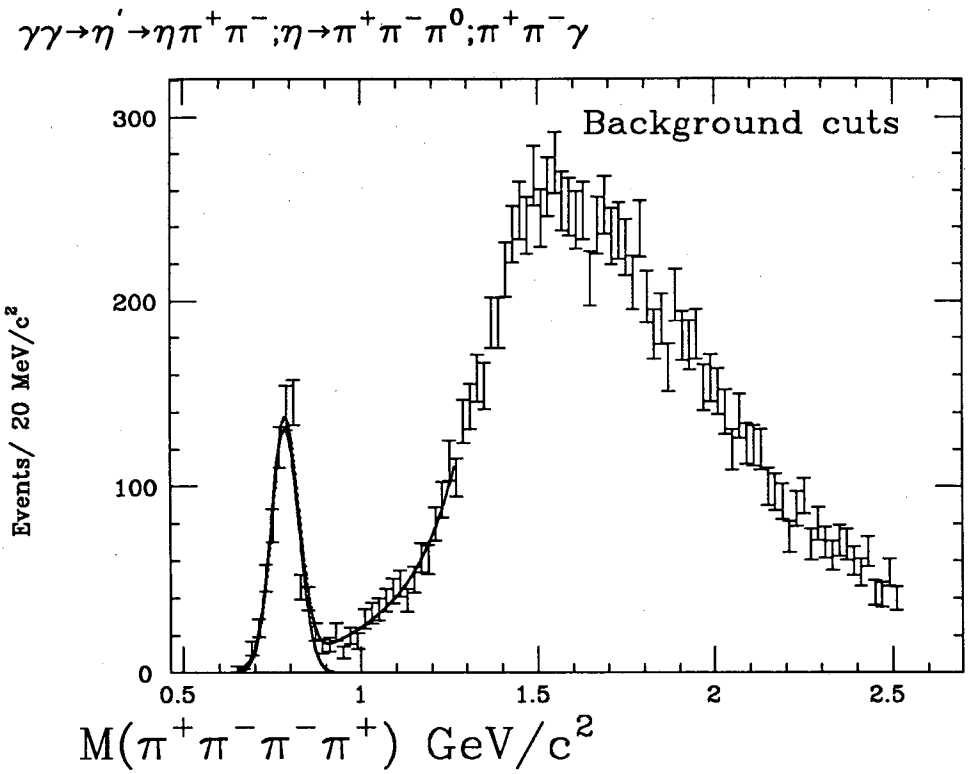

Figure 7.5 *$\pi^+\pi^-\pi^+\pi^-$ invariant mass distribution after all cuts*

7.3 SYSTEMATIC ERROR FOR $\eta' \to \eta\pi^+\pi^-; \eta \to \pi^+\pi^-\pi^0$, $\pi^+\pi^-\gamma$

The systematic error in the e^+e^- luminosity, that we looked at earlier, is of course the same when calculating the $\gamma\gamma$ width.

7.3.1 Systematic error due to background subtraction

The number of events found in the η' peak varies with fitting method. When a parameter is fixed, it is set equal to the value found in a Gaussian fit to the Monte Carlo events. Three fit methods were used:

1) All parameters free.

2) Sigma fixed.

3) Center position of Gaussian fitting η' peak fixed.

The background was fit with both a polynomial and a Gaussian with a large width ($\sigma \approx 350$ MeV). No direct physical significance should be given to the Gaussian helping fit the background.

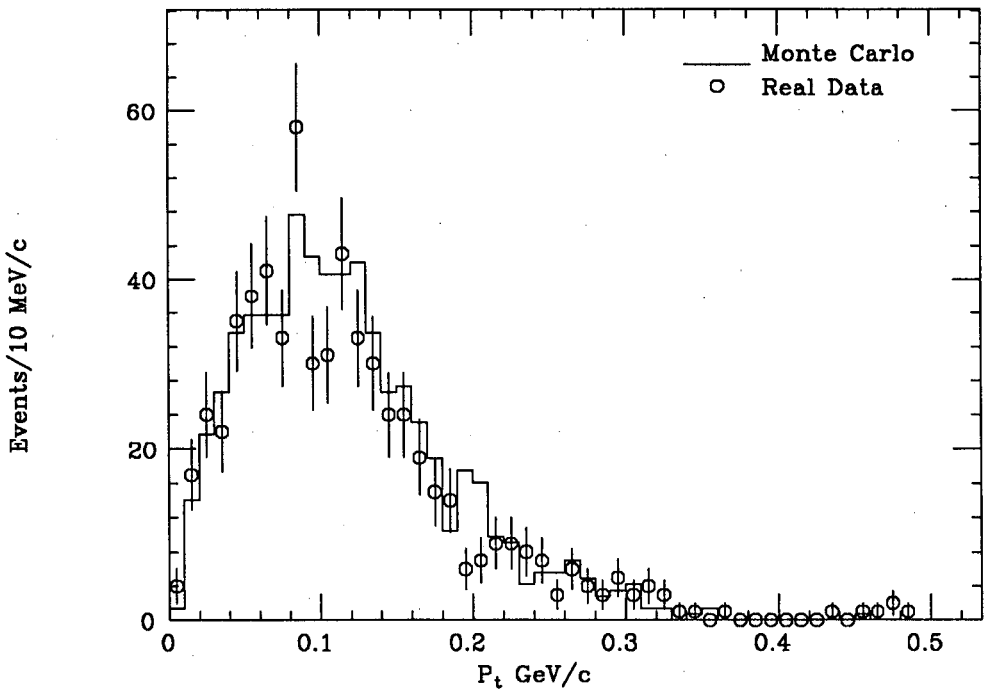

Figure 7.6 *The transverse momentum of the $\pi^+\pi^-\pi^+\pi^-$ system for events in the η' mass peak region*

Since the largest variation with fit method is 3.4%. A conservative systematic error would be ±4%.

7.3.2 Systematic error due to Monte Carlo simulation

Errors in fitting tracks

The detection of the decay mode $\eta' \rightarrow \eta\pi^+\pi^-; \eta \rightarrow \pi^+\pi^-\pi^0$, $\pi^+\pi^-\gamma$ relies only on finding the charged π's in these decay modes. We therefore avoid systematic errors introduced by trying to detect the gammas in the final state. The track finding systematic error is confined to the detection efficiency and measurement errors of charged tracks.

As part of the selection of tracks we required that the position within the detector of the point on the track at the minimum distance of approach to the beam origin be near the interaction point. We require that its Z position (distance along the beam axis) be within 50 cm of the interaction point and its distance away from the beam

axis be within 5 cm. These position cuts are much larger that those for tracks fit with a constraint to the primary vertex position, but the percentage for particles discarded by the cut is roughly comparable.

The track position cut is a source of systematic error in our measurement of $\Gamma_{\eta' \to \gamma\gamma}$ if the Monte Carlo simulation doesn't have the same position distribution as the real events. In this case a number of factors make the modeling of the measured track position crucial.

The larger number of charged tracks (4 as opposed to 2) in this decay mode magnifies systematic error due to modeling the efficiency for finding all the tracks.

The low momentum of the π's in this decay make for larger average multiple scattering angles for π's traversing detector materials. This makes correctly fitting the track position of tracks that undergo large angle scatters difficult.

The low momentum of the π's in this decay also make it more likely that a π will decay within the Drift Chamber volume ($\pi^{\pm} \to \mu^{\pm}\nu$) . The decay μ generally has a momentum different from the π from which it decayed. This causes tracking inefficiencies and errors.

To assess the systematic error associated with tracking, the 4π mass distribution was fit with the track position cut removed and compared to the 4π mass distribution with the cut. Removing the track position cut increased the number of η' events found for Monte Carlo data by 36%. For real data the increase was 42%. This change alone increases $\Gamma_{\eta' \to \gamma\gamma}$ by about 4%. The background under the η' peak increased but is subtracted by the fit.

The above arguments indicate that a cut on track position adds to the systematic error in $\Gamma_{\eta' \to \gamma\gamma}$. We would therefore like to use events without the track position cut to find the two-photon width. This would have the added advantage of giving us 42% more events in the η' peak and reducing the statistical error in our measurement.

But there is a problem when not using a vertex position cut. The problem comes when trying to make a correction for the trigger efficiency of low P_t tracks. The trigger efficiency is very sensitive at low P_t to the vertex cuts made on the tracks

used to find the efficiency. (see chapter 8)

When vertex cuts are removed, the events used to find the trigger efficiency do not have the same vertex position distribution as the tracks for events in the η' peak. This introduces an even larger systematic error into the $\Gamma_{\eta' \to \gamma\gamma}$ measurement than the systematic error introduced by the vertex cut itself. The systematic error from the trigger efficiency correction without a vertex cut is estimated at about 50%; with vertex cuts the error is reduced to about 12%. More will be said about the sensitivity of the trigger efficiency to the vertex position distribution in chapter 8 .

When the $\Gamma_{\eta' \to \gamma\gamma}$ is found using the tight and loose vertex cuts described in Chapter 8, the change in width indicates that systematic error due to the vertex cut is roughly 10%.

Efficiency for finding tracks

In addition to track fitting errors, we face the possibility that the efficiency for finding tracks may be different for Monte Carlo and real events. To check on this possibility the distribution of the angles that tracks make with the beam axis for events with 4π mass within the η' peak region was looked at.(see Figure 7.7)

In the real detector we would expect that track finding efficiency would be lower than that predicted by Monte Carlo , for tracks making small angles with the beam axis, since these tracks pass through fewer Drift Chamber layers. If the real detector is less than ideal (which is always the case) the already small number of measurements of track position for small angle tracks would make small angle track finding efficiency more sensitive to less than ideal tracking efficiencies.

If we compare Monte Carlo simulation to real data, as in Figure 7.7, we do see a small loss of efficiency at small angles when comparing real to Monte Carlo simulated tracks. For the mass range we are interested in we loose about 4% more tracks in the real events than in the Monte Carlo simulation. This implies about a +4% systematic error in $\Gamma_{\eta' \to \gamma\gamma}$ due to poor simulation of tracking efficiency by the Monte Carlo calculation for tracks with small angles to the beam axis. No $|\cos\theta|$ cut is done on all the track momenta since the systematic error introduced is relatively small and the cut would result in a significant loss of events.

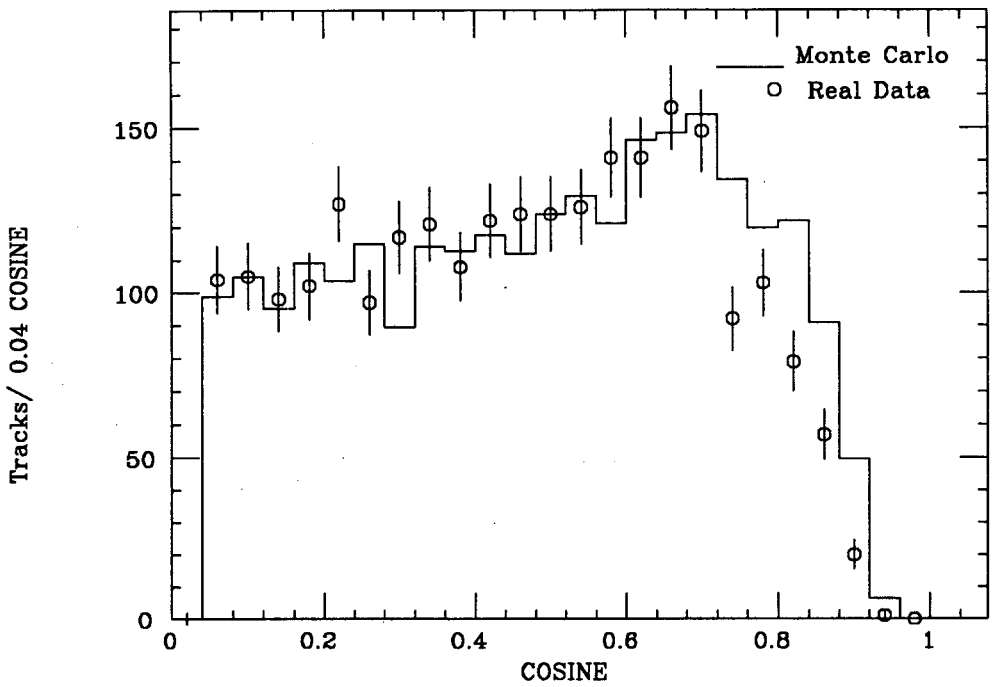

Figure 7.7 *The cosine of momentum of charged tracks with respect to the beam axis of events with a $\pi^+\pi^-\pi^+\pi^-$ mass in the η' peak region*

The tracking efficiency correction found by Rowson (see chapter 8) is about twice as large a correction as for the 2 prong decay modes, so we must reassess the systematic error for the 4 prong case.

As a check on this systematic error for tracking efficiency, the $\Gamma_{\eta' \to \gamma\gamma}$ was calculated using only the "good" data. The "good" data runs represent data taken during a period when there was no significant loss of tracking efficiency due to Drift Chamber hardware problems. Using only events from the "good" data gives a two-photon width which decreases by 23%. If we failed to correct for the tracking efficiency the two-photon width would change by only 15%. Therefore the largest systematic error that can be reasonably attributed to the tracking efficiency correction is -15%.

Trigger efficiency corrections

The trigger efficiency and its systematic error are discussed in chapter 8. The

trigger efficiency correction for the $\eta' \rightarrow \eta\pi^+\pi^-; \eta \rightarrow \pi^+\pi^-\pi^0$, $\pi^+\pi^-\gamma$ decay mode is about 25% . The systematic error introduced is estimated at 17% .

7.3.3 Systematic errors due to background subtraction

The number of events found in the η' peak varies with fitting method. When a parameter was fixed it was set equal to the value found in a Gaussian fit to the Monte Carlo simulated events. Four fit methods were tried:

1) All parameters free.

2) Sigma fixed.

3) Sigma fixed and Center position fixed

4) Center position fixed

The largest variation with fit method was +.6%. A reasonable systematic error would be ±1%.

7.4 RESULTS

The results of all four width measurements are summarized in table 8.2 . The measured decay width of this decay mode is:

$$\Gamma_{\eta' \rightarrow \gamma\gamma} = 5.24 \pm \underbrace{.56}_{statistical} \underbrace{+.77 \ -1.10}_{systematic} KeV$$

Chapter 8. Width calculations

This chapter will describe how measured event rates are used to find the two-photon width of the η' and $a_2(1320)$.

8.1 BASIC $\Gamma_{\gamma\gamma}$ CALCULATION

Calculating the $\gamma\gamma$ width of a resonance requires that the cross-section for producing the resonance when gammas associated with both electron beams collide be measured.

The full width Γ of a resonance is related by the Uncertainty Principle to its average lifetime τ .

$$\Gamma = \frac{\hbar}{\tau} \tag{8.1}$$

Thus all open decay channels for a resonance contribute to reducing its life time and the shorter the resonance's life time the larger it's full width.

The partial width for a given mode of decay is defined as the full width times the probability that the resonance will decay by the desired decay mode (the Branching Ratio).

$$\Gamma_{R\to X} \equiv \Gamma \cdot Br(R \to X) \tag{8.2}$$

To make a connection between the $\gamma\gamma$ partial width $\Gamma_{R\to\gamma\gamma}$ and the cross-section for two photons producing the resonance we can use an equation from Reference 26 which makes use of partial wave analysis and the assumption that the resonance with spin J can be described by a relativistic Breit-Wigner function.

$$\sigma(R \to \gamma\gamma) = 8\pi(2J+1)\frac{\Gamma \cdot \Gamma_{R\to\gamma\gamma}}{(W_{\gamma\gamma}^2 - M_R^2)^2 + \Gamma^2 M_R^2} \tag{8.3}$$

where:

Γ = the full width of the resonance

J = the spin of the resonance

$W_{\gamma\gamma}$ = the two-photon center of mass energy

$\Gamma_{R\rightarrow\gamma\gamma}$ = the two photon partial width of the resonance

M_R = the mass of the resonance

The full width of the η' (.24 MeV) is very small compared to the mass resolution of the detector and the change in $\gamma\gamma$ flux with a change in $W_{\gamma\gamma}$ over the width of the resonance. So we can replace the Breit-Wigner in Equation 8.3 with a δ function. In this case Reference 11 gives:

$$\sigma(R \rightarrow \gamma\gamma) = 8\pi^2(2J+1)\frac{\Gamma_{R\rightarrow\gamma\gamma}}{M_R}\delta(W_{\gamma\gamma}^2 - M_R^2) \tag{8.4}$$

To find $\Gamma_{R\rightarrow\gamma\gamma}$ we must find $\sigma(R \rightarrow \gamma\gamma)$. We can do this with the relation:

$$\sigma(R \rightarrow \gamma\gamma) = \frac{N_{produced}}{\int \mathcal{L}_{\gamma\gamma}dt} \tag{8.5}$$

Where:

$\int \mathcal{L}_{\gamma\gamma}dt$ = the $\gamma\gamma$ integrated luminosity when we use the Equivalent Photon Approximation (EPA).

$N_{produced}$ = the number of resonant states R produced

The number of produced R states is found by way of the relation:

$$N_{observed} = \mathcal{E}_{detector}N_{produced} \tag{8.6}$$

$\mathcal{E}_{detector}$ is the overall detector and analysis program efficiency for finding events in R states and must be found using Monte Carlo to simulate R events.

The functional form of the luminosity function $\int \mathcal{L}_{\gamma\gamma}dt$ has been discussed earlier in chapter 3 and may be used together with Equation 8.5 , Equation 8.6 and Equation 8.4 to solve for the $\gamma\gamma$ width of the resonance in terms of the resonant production

cross-section calculated using the e^+e^- luminosity instead of the $\gamma\gamma$ luminosity.

$$\Gamma_{R\to\gamma\gamma} = \frac{M_R^3 \;\sigma(e^+e^- \to e^+e^- R)}{16\alpha^2(\log(\frac{E_{beam}}{m_e}))^2 \; f(\frac{M_R}{2E_{beam}}) \; (2J+1)(Field\ correction)} \tag{8.7}$$

$$f(X) = (2+X^2)^2 \log(\frac{1}{X}) - (1-X^2)(3+X^2)$$

Where:

m_e= the rest mass of the electron

E_{beam}= the energy of one of the two colliding electron beams (for this case 14.5 GeV).

Field correction= correction to the approximate uncorrelated luminosity expression derived by F.Low (Reference 27). For the $\eta'(958)$ mass the correction is 0.7751, for the $a_2(1320)$ mass the correction is 0.7762 .

For $\Gamma_{\eta'\to\gamma\gamma}$ Equation 8.7 reduces to

$$\Gamma_{\eta'\to\gamma\gamma} = 3.051 \frac{KeV}{nanobarn} \; \sigma(e^+e^- \to e^+e^-\eta') \tag{8.8}$$

For $\Gamma_{a_2\to\gamma\gamma}$ Equation 8.7 reduces to

$$\Gamma_{a_2\to\gamma\gamma} = 1.800 \frac{KeV}{nanobarn} \; \sigma(e^+e^- \to e^+e^- a_2(1320)\ ) \tag{8.9}$$

The η' cross-section for e^+e^- can be found in a similar way to the $\gamma\gamma$ cross-section.

$$\sigma(e^+e^- \to e^+e^-\eta') = \frac{N_{\eta'\ observed}}{\mathcal{E}_{for\ \eta'} \int \mathcal{L}_{e^+e^-} dt} \tag{8.10}$$

Where:

$\int \mathcal{L}_{e^+e^-} dt$= the e^+e^- integrated luminosity

To find $\Gamma_{\eta'\to\gamma\gamma}$ for each decay mode $N_{\eta' observed}$ was calculated using branching ratios published by the Particle Data Group (Reference 28)

$$N_{\substack{\eta' specific \\ decay\ mode}} = Br(specific\ decay\ mode)\; N_{\eta' observed} \tag{8.11}$$

8.2 CORRECTIONS TO $\Gamma_{\eta' \to \gamma\gamma}$

In finding the $\gamma\gamma$ width, a number of corrections to the efficiency as found by the Monte Carlo simulation and to the luminosity as measured by the luminosity monitor must be included. Also the way in which the event data was processed to produce the input data summary tapes must be accounted for when dealing with the detection efficiency of each decay mode. A correction must be made to account for the simulation of trigger efficiency for low P_t tracks by the Monte Carlo program.

In order to include the above corrections in our calculations we will define an effective efficiency and an effective integrated luminosity. As described in section 2.10 the input data is split into 2 sets called "2PHOTSUM data" and "KEEPASS2 data." Each data set has its own integrated luminosity and its own detection efficiency. The effective efficiency and effective integrated luminosity are weighted sums, which combine these distinctly different data sets.

8.2.1 Luminosity corrections

The correction to the integrated luminosity is talked about in section 5.3.1 in connection with the systematic error due to this correction. This correction is a global one and is just a multiplicative factor affecting the width calculation. It need not enter into the weighted sums involving the 2 data sets.

The correction gives a real integrated luminosity that is 6% less that measured by the luminosity monitors.

8.2.2 Summary tape corrections

For practical reasons the input data in our analysis had to be divided into two sets. Section 2.10 describes the nature of these 2 data sets.

Finding the effective integrated luminosity

To find the effective integrated luminosity we must compensate for the relative importance of the 2 data sets (KEEPASS2 and 2PHOTSUM). To do this we run the

analysis program on the 2 data sets separately and divide the number of events found for each set by the integrated luminosity of each set. This gives the number of events per unit of integrated luminosity for each data set. We normalize these two numbers so that their sum is 1 . These are the weights for each data set.

Let:

W_1= KEEPASS2 data set weight

W_2= 2PHOTSUM data set weight

$W_1 + W_2 = 1$

We will define the effective luminosity as

$$\mathcal{L}_{effective} = C_{Lockyer}(W_1 L_1 + W_2 L_2) \tag{8.12}$$

Where:

L_1= KEEPASS2 data set integrated luminosity

L_2= 2PHOTSUM data set integrated luminosity

$C_{Lockyer}$= Luminosity correction of section 8.2.1

Equation 8.12 has the property that if all events come from one of the data sets, the effective luminosity becomes the same as the luminosity of that data set times the Lockyer correction. [21]

The W_1 and W_2 have statistical errors that affect the error in $\mathcal{L}_{effective}$. This error is give by

$$\sigma^2_{\mathcal{L}_{effective}} \approx (L_1 - L_2)^2[\sigma^2_{W_1} W_2^2 + \sigma^2_{W_2} W_1^2] \tag{8.13}$$

Equation 8.13 makes it clear that the statistical error in the effective integrated luminosity will be small in comparison to the statistical error in the $\gamma\gamma$ width. The the statistical error in $\mathcal{L}_{effective}$ vanishes altogether if both data sets have the same luminosity.

Finding the effective efficiency

The expression for the effective efficiency is

$$\mathcal{E}_{effective} = \mathcal{E}_{M.C.}\mathcal{E}_{Rowson}(\mathcal{E}_1 W_1 + W_2) \tag{8.14}$$

Where:

$\mathcal{E}_{M.C.}$= the raw Monte Carlo simulation's efficiency ($\frac{N_{observed\ M.C.}}{N_{generated\ M.C.}}$) The number of Monte Carlo simulated events is corrected for the trigger efficiency of low P_t tracks.

$\mathcal{E}_{Rowson}$= the Rowson tracking efficiency correction, it must be weighted by KEEPASS2 and 2PHOTSUM weights over the different sets of runs. More will be said in the next section.

$\mathcal{E}_1$= the KEEPASS2 efficiency. It corrects for the efficiency of the KEEPASS2 event recovery program discussed in section 2.10 . This is the number of KEEPASS2 events found divided by the number of anti-chukit events found when run on the same data set. The Monte Carlo program can not simulate the hardware data used by the KEEPASS2 summary tape program, so this correction must be made.

The effective efficiencies (see Equation 8.14) for the four two-photon decay widths found in this thesis are tabulated in Table 8.1

Table 8.1 *A summary of effective efficiencies*

Decay Mode	Effective Efficiency
$a_2 \rightarrow \rho\pi$	0.609%±0.035%
$\eta' \rightarrow \rho\gamma$	1.024%±0.028%
$\eta' \rightarrow \eta\pi^+\pi^-; \eta \rightarrow \gamma\gamma$	0.249%±0.027%
$\eta' \rightarrow \eta\pi^+\pi^-; \eta \rightarrow \pi^+\pi^-\pi^0$, $\pi^+\pi^-\gamma$	1.152%±0.152%

8.2.3 Trigger and tracking efficiency corrections

The efficiency for seeing tracks must be corrected for.

The Drift Chamber tracking efficiency correction

The efficiency for finding tracks with the Drift Chamber has changed for different parts of the PEP data collection running. The tracking program can miss

finding tracks when parts for the Drift Chamber are inefficient. This inefficiency was measured by Rowson. [23]

To find this correction to the efficiency, the correction for each set of running is weighted by the effective luminosity of that section of running.

$$\mathcal{E}_{Rowson} = \frac{\sum_{i=subset} (\mathcal{E}^i_{tracking})^n (W_1 L_{1,i} + W_2 L_{2,i})}{\sum_{i=subset} (W_1 L_{1,i} + W_2 L_{2,i})} \tag{8.15}$$

The correction is thought to be independent of track momentum and angle. Where:
W_1= KEEPASS2 data set weight
W_2= 2PHOTSUM data set weight
i = The index for each section of the data which has a different tracking efficiency.
$\mathcal{E}^i_{tracking}$ = The single track efficiency for finding a track
n = The number of charged tracks in the event
$L_{1,i}$ and $L_{2,i}$ = The KEEPASS2 and 2PHOTSUM integrated luminosity for the runs in the i th subset

The hardware trigger efficiency correction

The Monte Carlo program does not do an adequate job of simulating the hardware trigger for tracks with low transverse momentum relative to the beam line.

The Monte Carlo program does a simple and inadequate trigger simulation for charged tracks. For an event to pass the Monte Carlo trigger and have a full simulation done for the event it is only necessary that one "A track" be found by its rough trigger simulation. The single track Monte Carlo simulation's efficiency stays above 90% for P_t 's above 70 MeV/c. Since the real hardware trigger requires 2 A tracks to trigger and since we do not use events with tracks with less that 90 MeV/c, the trigger efficiency for Monte Carlo events is at least 99% for all useful events.

Of more difficulty is the problem of correctly simulating the hardware trigger. To account correctly for the hardware trigger an analysis of real 4 prong events was

done. The trigger efficiency was found for single tracks by looking at the trigger information stored, for a subclass of events.

After making a track vertex position cut I looked at cases where tracks other than the one being considered cause the trigger to be satisfied. For this class of events we can now look at the track being considered and use the stored hardware trigger information to decide if this track also triggered. Using this method the trigger efficiency was found as a function of the P_t with 10 MeV/c histogram bin widths. A fit was done to the resulting histogram. (See Figure 8.1)

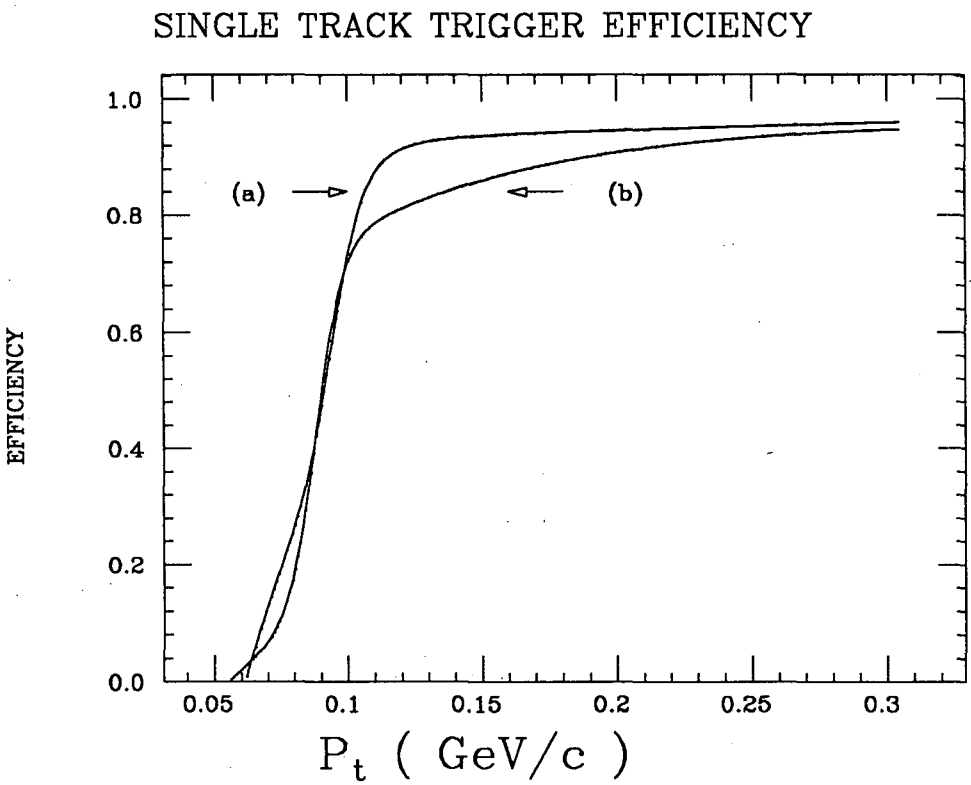

Figure 8.1 *Trigger efficiency of single tracks vs track P_t (a) 2 prong trigger efficiency (b) 4 prong trigger efficiency*

To correct the Monte Carlo events for trigger efficiency the parameters found by fitting the single track efficiency were used to define an efficiency function, which was then applied to the Monte Carlo events. The trigger efficiency at low momenta is strongly dependent on the vertex position cuts used on the subclass of events used to find the efficiency. For this reason the trigger efficiency function used to correct

the Monte Carlo calculation was found using the same vertex cuts used for the decay mode being considered.

For the 2 prong decays the trigger efficiency can be found simply as the product of the two single track trigger efficiencies. This is because 2 tracks are required to trigger for the event to be logged (number of "A tracks" greater or equal to 2). For the 4 prong decay $\eta' \rightarrow \eta\pi^+\pi^-; \eta \rightarrow \pi^+\pi^-\pi^0$, $\pi^+\pi^-\gamma$ the situation is considerably more complex, since 2,3 or 4 tracks can have directions that will allow them to be classified as an "A track" by the trigger hardware logic. For a track to be classified as an A track the hardware curvature modules must find a majority of hits in the Drift Chamber layers (2 of 4 inner VC layers hit, 4 of 8 selected DC layers hit where 2 of these 4 hits were in the outer 6 DC layers) and have a hit in the Time of Flight modules at a position that matches the track's path. Not all tracks make a large enough angle with the beam axis to trigger. (See Chapter 2)

For the 4 prong case the trigger efficiency is found by finding the total probability to trigger for the given set of tracks accounting for all combinations of single track triggers that can satisfy the overall trigger. In addition the fitting error for each track combination is used to find the total error in the trigger total efficiency for the event. This error is included in the fit to the Monte Carlo simulated mass distribution peak.

8.2.4 Systematic error in the trigger efficiency corrections

By finding the single track efficiency for charged tracks using a variety of selection criteria it became evident that the vertex position selection had the largest effect on the low P_t trigger efficiency. (See Figure 8.1) The nominal vertex position cut used for the $\eta' \rightarrow \rho\gamma$ and $\eta' \rightarrow \eta\pi^+\pi^-; \eta \rightarrow \gamma\gamma$ requires that the primary vertex constrained fit for each tracks vertex position have a radius less than 1 cm and a Z position (position along the beam line) of -5 cm to 3.5 cm. For the decay mode $\eta' \rightarrow \eta\pi^+\pi^-; \eta \rightarrow \pi^+\pi^-\pi^0$, $\pi^+\pi^-\gamma$ the nominal vertex position selection is different. The non-primary vertex constrained vertex position must have a radius from the beam line of less than 5 cm and a Z position distance relative to the beam crossing

point of less than 50 cm.

The trigger efficiency correction for the decay modes $\eta' \rightarrow \rho\gamma$ and $a_2 \rightarrow \rho\pi$ is about 8% and so the trigger efficiency systematic error is conservatively no more than about 5%. The smaller trigger efficiency correction for the $\eta' \rightarrow \rho\gamma$ decay is due to the larger P_t of π's coming from the high fraction of the η' rest mass used to create the $\rho(770)$ which decays by $\rho(770) \rightarrow \pi^+\pi^-$. The $a_2(1320)$ also produces higher P_t π's since it has a greater rest mass than the $\eta'(958)$ and so more energy is available to produce large P_t .

The $\eta' \rightarrow \eta\pi^+\pi^-; \eta \rightarrow \gamma\gamma$ and $\eta' \rightarrow \eta\pi^+\pi^-; \eta \rightarrow \pi^+\pi^-\pi^0$, $\pi^+\pi^-\gamma$ decay modes have trigger efficiency corrections of 33% and 25% respectively. The two-photon widths for both decay modes were recalculated using tighter vertex cuts. The vertex radius cut was halved and the trigger efficiency correction recalculated and fit. The trigger corrections for the tighter cuts were then used to correct the Monte Carlo simulated trigger efficiency.

The new $\Gamma_{\eta' \rightarrow \gamma\gamma}$ for $\eta' \rightarrow \eta\pi^+\pi^-; \eta \rightarrow \gamma\gamma$ decreased by 3.3% while the width without the trigger correction decreased by only 1.5%, indicating that the vertex cut itself is not a large source of systematic error for this decay mode.

The new $\Gamma_{\eta' \rightarrow \gamma\gamma}$ for $\eta' \rightarrow \eta\pi^+\pi^-; \eta \rightarrow \pi^+\pi^-\pi^0$, $\pi^+\pi^-\gamma$ decreased by 11.4% while the width without the trigger correction decreased by 6.8%, indicating that the vertex cut itself is a significant source of systematic error for this decay mode.

The above leads to an estimate of 4% trigger efficiency systematic error for $\eta' \rightarrow \eta\pi^+\pi^-; \eta \rightarrow \gamma\gamma$ and an estimate of 12% trigger efficiency systematic error for the $\eta' \rightarrow \eta\pi^+\pi^-; \eta \rightarrow \pi^+\pi^-\pi^0$, $\pi^+\pi^-\gamma$ decay mode.

All the systematic errors related to the four two-photon widths found in this thesis are tabulated in Table 8.2

Table 8.2 *A summary of errors affecting $\Gamma_{\gamma\gamma}$ measurements*

Decay Mode	$\eta' \to \rho\gamma$	$a_2 \to \rho\pi$	$\eta' \to \eta\pi^+\pi^-$ $\eta \to \gamma\gamma$	$\eta' \to \eta\pi^+\pi^-$ $\eta \to \pi^+\pi^-\pi^0$ $\eta \to \pi^+\pi^-\gamma$
Luminosity measurement	±5%	±5%	±5%	±5%
Tracking efficiency	±3%	±3%	±3%	−15%
Background subtraction	±2.7%	±17%	±4%	±1%
M.C. simulation of γ's	±10%	±10%	±20%	
Hand Scan			+5% −2%	
Trigger efficiency	±5%	±5%	±4%	±12%
Vertex cut				±6.8%
Total Systematic error	±13%	±21.2%	22.2% −21.6%	+14.7% −21.0%
$\Gamma_{\gamma\gamma}$ (KeV)	5.26	1.17	4.98	5.24
Statistical error	±.37	±.15	±.71	±.56
Systematic error	±.68	±.25	+1.11 −1.08	+.77 −1.10

Chapter 9. Conclusions

In the introduction we described how $\Gamma_{\eta' \to \gamma\gamma}$ could be used to help resolve the question of the quark and gluonium content of the η' . We will evaluate what our measured values for $\Gamma_{\eta' \to \gamma\gamma}$ say about the above questions and compare our results to those of others.

As a by product of measuring the η' two-photon width using the decay mode $\eta' \to \rho\gamma$ we also found $\Gamma_{a_2(1320) \to \gamma\gamma}$. Table 9.1 and Figure 9.1 compare our $a_2(1320)$ two-photon width measurements to other recent measurements. Table 9.2 and Figure 9.2 compare our η' two-photon width measurements to recent measurements. The weighted averages in both the above figures are weighted by the quoted statistical error only.

Table 9.1 *Recent measurements of* $\Gamma_{a_2(1320) \to \gamma\gamma}$

Experiment	$\Gamma_{a_2(1320) \to \gamma\gamma}$ (keV)	Reference
Crystal Ball (SPEAR)	$0.77 \pm 0.19 \pm 0.27$	39
CELLO	$0.81 \pm 0.19 \pm 0.27$	40
JADE	$0.84 \pm 0.07 \pm 0.15$	41
PLUTO	$1.06 \pm 0.18 \pm 0.19$	42
Crystal Ball (DORIS)	$1.14 \pm 0.20 \pm 0.26$	43
TASSO	$0.90 \pm 0.27 \pm 0.16$	44
TPC/2γ	$0.90 \pm 0.09 \pm 0.22$	45
Mark II	$1.17 \pm 0.15 \pm 0.25$	This Thesis

If we take our three measurements of $\Gamma_{\eta' \to \gamma\gamma}$ and find the weighted average, weighting by only the statistical error we find:

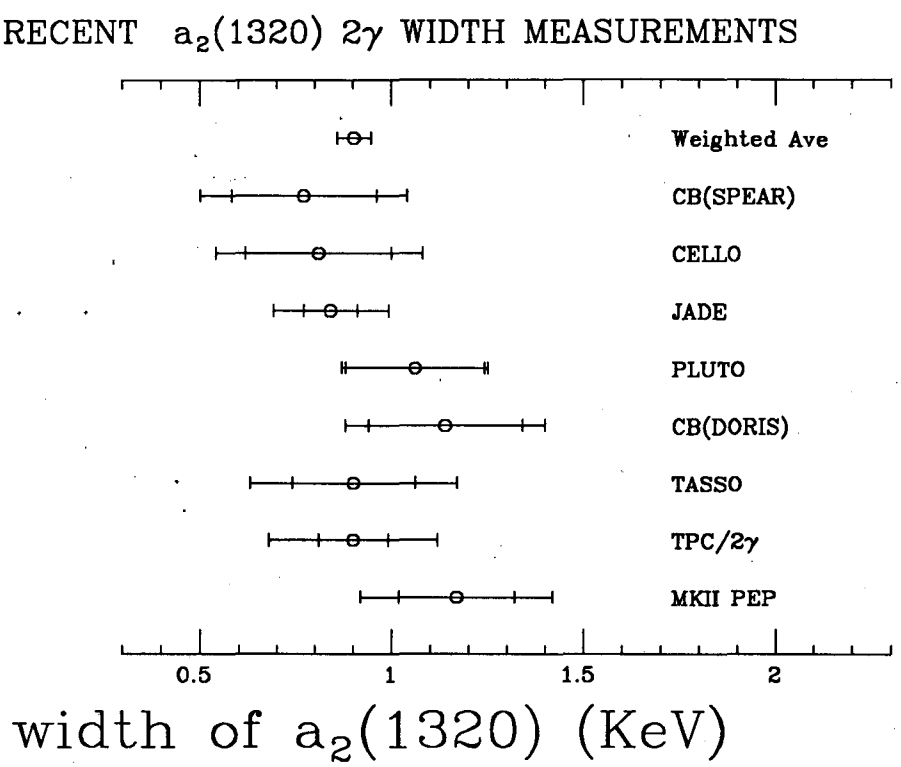

Figure 9.1 *Recent measurements of the $a_2(1320)$ two-photon width*

$$\Gamma(\eta' \to \gamma\gamma) = 5.21 \underbrace{\pm.28}_{statistical} \quad keV$$

This can be compared to the world average width of 4.20 ± 0.091keV. The world average is dominated by the ARGUS result. Without the ARGUS result the world average increases to 4.63 ± 0.13keV. The ARGUS result's statistical error seems unrealistically low. The quoted statistical error of $\pm 3.5\%$ is less than the error in the η' to $\rho\gamma$ branching ratio relative error quoted by the Particle Data Group of $\pm 5.4\%$ [46], which must be used to calculate $\Gamma_{\eta' \to \gamma\gamma}$ from the measured partial width $Br(\eta' \to \rho\gamma) \cdot \Gamma_{\eta' \to \gamma\gamma}$.

The preliminary results of our measurement of $\Gamma_{\eta' \to \gamma\gamma}$ using the decay modes $\eta' \to \rho\gamma$ and $\eta' \to \eta\pi^+\pi^-; \eta \to \gamma\gamma$ gave lower values when compared to our final results. When the trigger efficiency was correctly accounted for the two-photon width was increased by 8% and 33% for the $\eta' \to \rho\gamma$ and $\eta' \to \eta\pi^+\pi^-; \eta \to \gamma\gamma$ decay modes

Table 9.2 *Recent measurements of* $\Gamma_{\eta' \to \gamma\gamma}$

Experiment	$\Gamma_{\eta' \to \gamma\gamma}$ (keV)	Mode	Reference
MARK II(SPEAR)	$5.8 \pm 1.1 \pm 1.2$	$\rho\gamma$	29
JADE	$5.0 \pm 0.5 \pm 0.9$	$\rho\gamma$	30
CELLO	$5.4 \pm 1.0 \pm 0.7$	$\rho\gamma$	31
PLUTO	$3.80 \pm 0.26 \pm 0.43$	$\rho\gamma$	32
TASSO	$5.1 \pm 0.4 \pm 0.7$	$\rho\gamma$	33
JADE	4.0 ± 0.9	$\gamma\gamma$	34
Crystal Ball	$5.0 \pm 0.6 \pm 0.8$	$\gamma\gamma$	35
TPC/2γ	$4.5 \pm 0.3 \pm 0.7$	$\rho\gamma$	36
ARGUS	$3.76 \pm 0.13 \pm 0.47$	$\rho\gamma$	37
Crystal Ball	$4.6 \pm 0.4 \pm 0.6$	$\eta\pi^0\pi^0$	38
MARK II(PEP)	$5.26 \pm 0.37 \pm 0.68$	$\rho\gamma$	This Thesis
MARK II(PEP)	$4.98 \pm 0.71 + 1.11 - 1.08$	$\eta\pi^+\pi^-$	This Thesis
MARK II(PEP)	$5.24 \pm .56 + 0.77 - 1.10$	$\pi^+\pi^-\pi^+\pi^-$	This Thesis

respectively.

The mixing angle Θ, between the η and η' was defined in chapter 1 and can be found by the relation :

$$\frac{\Gamma(\eta' \to \gamma\gamma)}{\Gamma(\pi^0 \to \gamma\gamma)} \frac{m_{\pi^0}^3}{m_{\eta'}^3} = \frac{1}{3}(\sin\Theta + 2\sqrt{2}\cos\Theta)^2 \tag{9.1}$$

Solving for Θ we have :

$$\Theta = \sin^{-1}\left[\frac{1}{3}\sqrt{\frac{3m_{\pi^0}^3}{m_{\eta'}^3} \frac{\Gamma(\eta' \to \gamma\gamma)}{\Gamma(\pi^0 \to \gamma\gamma)}} \right] - \cos^{-1}[\frac{1}{3}] \tag{9.2}$$

Using the weighted average for $\Gamma_{\eta' \to \gamma\gamma}$ from the three decay modes considered in this thesis we find the mixing angle $\Theta = -19.0^o \pm 2.0^o$. The world average mixing angle is $\Theta = -25.8^o \pm 0.6^o$, without the ARGUS result the average mixing angle is

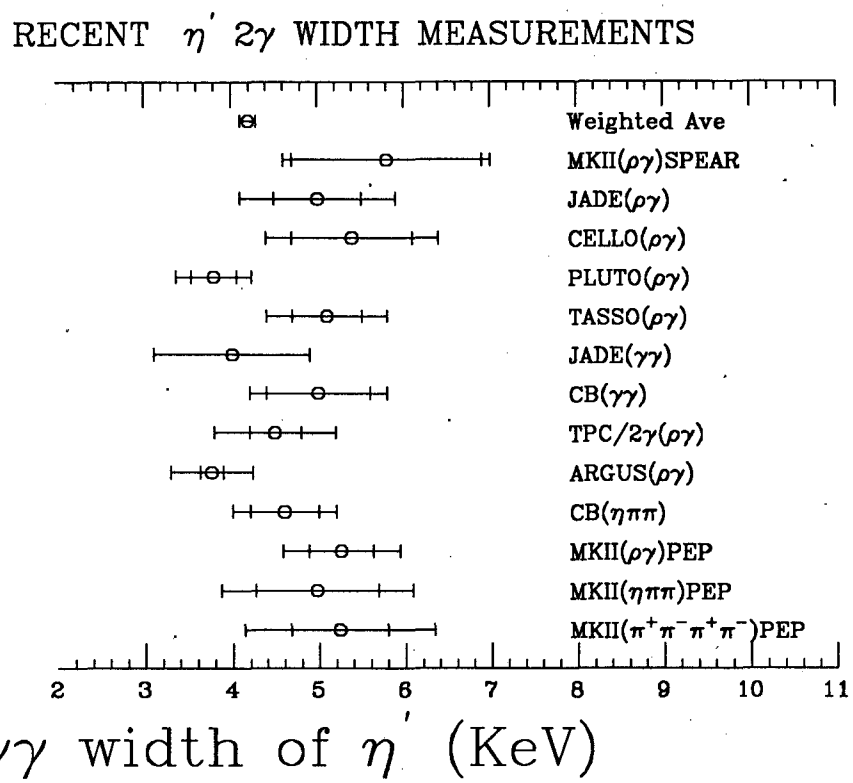

Figure 9.2 *Recent measurements of* $\Gamma_{\eta' \to \gamma\gamma}$

$\Theta = -22.9^o \pm 0.9^o$. The mixing angles found corresponding to the two-photon widths in Figure 9.2 are shown in Figure 9.3 .

As described in chapter 1, for the η' the allowed regions of the $X_{\eta'} - Y_{\eta'}$ plane are restricted by: [4]

$$\frac{\Gamma(\eta' \to \gamma\gamma)}{\Gamma(\pi^0 \to \gamma\gamma)} = \frac{1}{9}[\frac{m_{\eta'}}{m_{\pi^0}}]^3(5X_{\eta'} + \sqrt{2}Y_{\eta'})^2 \tag{9.3}$$

$$\frac{\Gamma(\eta' \to \rho\gamma)}{\Gamma(\omega \to \pi^0\gamma)} = 3\left[\frac{m_{\eta'}^2 - m_\rho^2}{m_\omega^2 - m_{\pi^0}^2}\frac{m_\omega}{m_{\eta'}^2}\right]^3 X_{\eta'}^2 \tag{9.4}$$

Figure 9.4 shows regions of the $X_{\eta'} - Y_{\eta'}$ allowed by Equation 9.3 and Equation 9.4. The allowed regions were calculated using the most recent values of masses and partial width and the average $\Gamma_{\eta' \to \gamma\gamma}$ measured in this thesis. [47] The allowed regions in Figure 9.4 are consistent with no gluonium mixing in the η' . Gluonium mixing is not ruled out however.

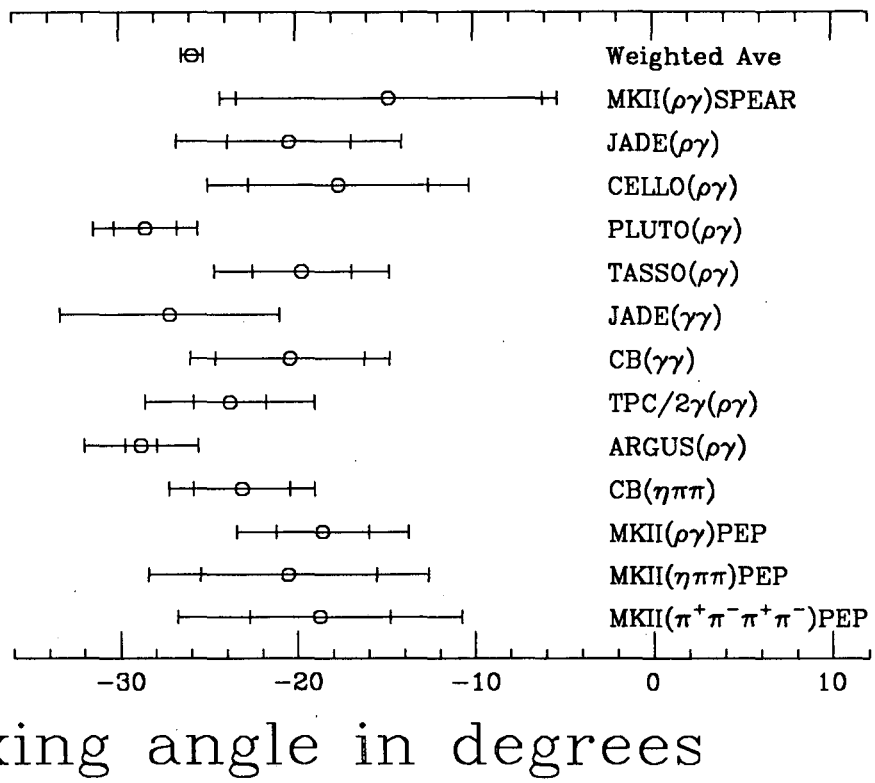

Figure 9.3 *Mixing angle between the η and η' calculated from recent measurements of $\Gamma_{\eta'\to\gamma\gamma}$*

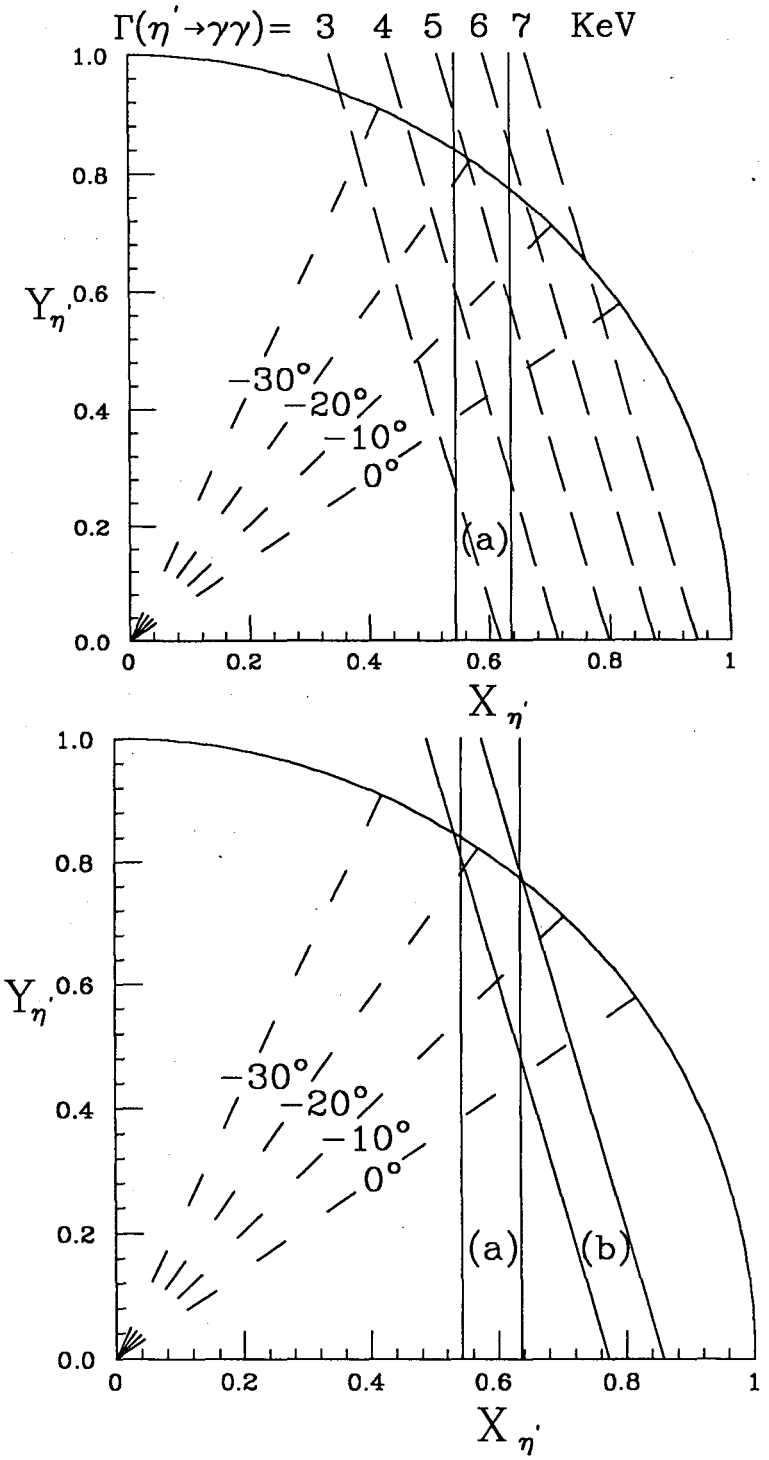

Figure 9.4 *Constraints on nonstrange ($X_{\eta'}$) and strange ($Y_{\eta'}$) quarkonium mixing coefficients in the η' . The circular arcs denote a pure quarkonium η' . The dashed lines from the origin give the corresponding mixing angle Θ for points in the $X_{\eta'} - Y_{\eta'}$ plane. The backward slanted dashed lines are lines of equal $\Gamma(\eta' \to \gamma\gamma)$ (a) is the region allowed by $\Gamma(\eta' \to \rho\gamma)/\Gamma(\omega \to \pi^0\gamma)$. (b) is the region allowed by $\Gamma(\eta' \to \gamma\gamma)/\Gamma(\pi^0 \to \gamma\gamma)$.*

Appendix A. Summary Tape event selection Criteria

To reduce the volume of events that must be stored on tape, a set of summary tapes was made. The summary tape program "2photsum" was used to keep only those events that fell into categories of interest. Events also were required to pass minimum quality selection criteria.

SUMMARY OF 2PHOTSUM CUTS

I) initial cuts on all changed tracks in all events

1) No drift chamber tracks of unknown charge.
2) Must have track identifier for each track
3) Must have charge +/- 1 all charged tracks.
4) Total charge must be zero
5) The primary vertex must have a simple vertex determination by vtxr1,no track parameters varied .
6) Z cut on primary vertex. Z= +/- 10 cm
7) All charged tracks must have at leased a one track fit.
8) Total energy of charged tracks must be less than 40% of total beam energy.
9) number of charged prongs must be 2,4,6 or 8 .

II) Initial cuts on all neutral tracks.

No neutral track cut will throw out event.
only the given neutral track.

1) neutral track must be well identified.
2) neutral track must have calorimeter data available.
   a) must have energy above 150 Mev for LA .
   b) must have energy above 200 Mev for endcap.

Note: If the event includes one or more sat tracks which make the sat cuts given below then the total event pt relative to the beam line is corrected for the sat track momentum. This correction is made on all logged events.

III) Event logging cuts for non 2 prong events.

1) log if event pt**2 of charged tracks less than 0.1 gev**2

2) log for single gamma event if pt**2 less than 0.1 gev**2

IV) Event logging cuts for 2 and 4 prongs.

Before more event cuts are done neutral and charged track cuts are redone.

1) Cuts on charged tracks for 2 and 4 prongs

a) all charged tracks must have identified charge.

b) all charged tracks must have a vertex constrained fix.

c) muon id and TOF data is picked up if of good quality. and used to discard electrons and muons.

2) Cuts on each neutral track 2 and 4 prongs.

No neutral track cut will throw out the event.

a) track has well identified charge. i.e. charge is zero

b) track must have calorimeter data available.

c) track energy must be above 150 mev for LA .

d) track energy must be above 200 mev for end cap.

e) neutral track must not be near charged track (greater than 7 cm at trigger plane)

V) EVENT CUTS FOR 2 AND 4 PRONGS

1) 2 PRONGS WITH LARGE INVARIANT MASS AND SMALL PT

a) require that one track is within fiducial angle for muon and electron identification.

(abs(cos(theta))<.56)

b) nether track must be identified as an electron or muon.

c) both track must have muid and LA id subtypes defined.

d) require low pt**2 (pt**2 < 0.1 gev**2)

e) require high invariant mass (mass > 1.6 Gev)

2) 2 PRONGS WITH ONE GAMMA AND LOW PT

a) only one gamma passing gamma cuts.

b) require low pt**2 (pt**2 < 0.1 gev**2)

3) K,KBAR AND P,PBAR EVENTS

a) require TOF mass**2 of both prongs be larger than a circular cut or radius 0.15 gev**2 if both TOF masses are greater than zero.

b) require that one of the TOF masses is greater than 0.15 gev**2 if the other is negative.

c) require low pt**2 (pt**2 < 0.1 gev**2)

note: constrained gamma pairs are found by taking all combinations of 2 and 3 gammas and constraining them first to an eta, then if the chi square is to large, constraining them to a PI0 . when 3 pairs are used 2 of them are added together to form one gamma. The assumption is that one gamma may have been identified as 2 separate gammas. Gamma pairs are not used which have more than one gamma in the same endcap.

4) 2PI,ETA or 2PI,PI0

a) require visible energy of combination less than 40% of total beam energy.

b) the number of gammas must be 4 or less .

c) require that the pt**2 of only one of the gamma pairs and the 2 charged tracks be low. (pt**2 < 0.1 gev**2)

5) 4PI,ETA or 4PI,PI0

Take all combinations of constrained gamma pairs with the 4 charged tracks.

a) require visible energy of combination less than 40% of total beam energy.

b) the number of gammas must be 3 or less .

c) require that the pt**2 of only one of the gamma pairs and the 4 charged tracks be low. (pt**2 < 0.1 gev**2)

6) 2PI0,2ETA0

Take all combinations of eta constrained gamma pairs, which could be 4 to 6 gammas. Make sure no gamma is used more than once. If the track passes the cuts for any one of the combinations log the event.

a) require 4 or 5 gammas.

b) require chi squared of eta constrained fit to be less than 4.0 for both pairs on gammas used.

c) require visible energy of combination less than 40% of total beam energy.

d) require low pt**2 (pt**2 < 0.1 gev**2)

VI) CUTS FOR SAT TRACKS

1) subroutine SATFIT is called to retrack sat data using raw data. SATFIT calls SADTOK which checks track quality.

   a) sat must point at beam

   b) sat must go through the window in the cone.

2) SATFIT also calls subroutine FILSAT, this routine has been modified to keep sat parameters normally thrown away after sat tracking.

   a) sat energy must be 3.0 to 20.0 Gev

   b) zscale within +/- 0.01

      where zscale=zdifip*(sin(2.0*satzcs)**2)

      zdifip= Z difference between the distance of closest approach to the beam axis and the IP

      satzcs = theta, angle with the z axis

      Zscale scales the Z distribution based on the expected error in Z. This tends to keep the efficiencies for large and small angle tracks the same.

If a track passes all cuts for a good sat track the sat parameters are placed in a new subtype as follows.

TRK(TRKSUB(K,I)+J)

subtype	J	name	contents
11	1	XOSAT	X,Y,Z COORDS OF A POINT THAT IS ON THE
	2	YOSAT	SAT TRACK.
	3	ZOSAT	
	4	USAT	X,Y,Z DIRECTION COSIGNS OF SAT TRACK
	5	VSAT	
	6	WSAT	
	7	XDOCAB	X,Y,Z OF THE POINT ON THE BEAM LINE
	8	YDOCAB	OF THE POINT OF CLOSEST APPROACH OF
	9	ZDOCAB	OF THE SAT TRACK.
	10	XDOCAT	X,Y,Z OF THE POINT ON THE SAT TRACK
	11	YDOCAT	OF THE POINT OF CLOSEST APPROACH.
	12	ZDOCAT	
	13	DOCA	DISTANCE OF CLOSEST APPROACH
	14	SATVDZ	Z DISTANCE BETWEEN THE SAT POINT OF CLOSEST APPROACH ON THE BEAM LINE TO THE Z POSITION OF THE INTERACTION POINT.
	15	ISATGD	TOTAL NUMBER OF GOOD SATS,NOTE THIS IS REDUNDANT SINCE ONLY GOOD SAT TRACKS HAVE SUBTYPE 11 DEFINED i.e. TRKSUB(K,I) NOT 0
	16	ESATTP	SAT TRACK ENERGY IN GEV
	17	XDF	SAT TRACKING FIT CHI SQUARE PER DEGREE OF FREEDOM

REFERENCES

1. F.-M.Renard, Electron-Positron Collisions, Edition Frontière, Gif sur Yvette, France, 1981
2. Stephen L. Adler, Physical Review Volume 177, Number 5, , 25 January 1969,pages 2426-2438
3. M. Chanowitz, "Resonances in Photon Photon scattering", Proceedings of the VI^{th} International Workshop on Photon-Photon Collisions, Lake Tahoe, Sept. 10-13 1984, Edited by R.L.Lander.
4. J.L.Rosner, "Quark content of neutral mesons" Phys. Rev. D27,1101(1983)
5. C.Edwards et al., Phys.Rev.Lett. 49(1982) 259
6. R. H. Schindler et al., Phys. Rev. D 24, 78 (1981)
7. J. Jaros in Proceedings of the International Conference on Instrumentation for Colliding Beam Physics, SLAC-Report 250, edit by W. Ash, Stanford CA, 29 (1982)
8. T. Himel, thesis, Stanford University, SLAC-223 (1979)
9. J.A.M. Vermaseren, Proceedings of the intern. Workshop on $\gamma\gamma$-Collisions, Amiens, ed. G Cochard and P.Kessler, Lecture Notes in Physics Vol.134, Springer Verlag (1980); N.Arteaga-Romero, A.Jaccarini, P.Kessler and J.Parisi, Phys.Rev. D3 (1971) 1569;
10. Bonneau,Martin, Nuclear Physics B54(1973) 573-597
11. THE TWO-PHOTON PARTICLE PRODUCTION MECHANISM. PHYSICAL PROBLEMS. APPLICATIONS. EQUIVALENT PHOTON APPROXIMATION, V.M. Budnev et al., Physics Reports(Section C of Physics Letters)15, no.4 (1975)181-282.
12. J. H. Field, Nuclear Physics B168 (1980) 477-494
13. Properties of the η' Meson. By Alan Rittenberg (LBL,Berkeley), UCRL-18863 June 4, 1969. 127pp. Ph.D. Thesis
14. J. D. Jackson NUOVO CIMENTO 34 (1964) 1644
15. GELL-MANN and WATSON Rev of NUCL SCI 4,219 (1954)
16. J. E. Olsson, Proceedings of the 5th Intern. Colloquium on $\gamma\gamma$ Interactions,

Aachen, ed. Ch.Berger, Lecture Notes in Physics Vol.191, Springer Verlag (1983)

17. Hermann Kolanoski,Bonn Univ,BONN-HE-84 Feb 1984 issn-0172
18. First Observation of $\pi_2(1680)$ in $\gamma\gamma$ reactions at Crystal Ball, B. Muryn et al., Submitted to the VII international Workshop on Photon-Photon Collisions, Shoresh, Jerusalem Hills, Israel, April 24-28, 1988
19. BNL workshop on Glueballs, Hybrids and exotic Hadrons, Michael Feindt, Aug 27, 1988
20. Inclusive Lepton Production in Hadronic Events From e^+e^- Annihilation at 29 GeV. By M.E. Nelson (LBL, Berkeley), LBL-16724, October 1983. 191pp. Ph.D. Thesis.
21. Nigel Lockyer,Mark II memo,21 June 1984
22. Dean Karlen,Mark II memo,13 October 1987
23. Peter C. Rowson,SLAC MEMO,TG note 379 February 21,1984
24. Differential cross sections for $\gamma\gamma \rightarrow p\bar{p}$ in the C.M. energy range from 2.0 to 3.1 Gev,ISSN 0428-9833 DESY 83-064 July 1983
25. W.R. Nelson and T.M. Jenkins(Eds.), *Computer Techniques in Radiation Transport and Dosimetry* (Plenum Press, New York,1980)
26. V.M.Budnev, I.F.Ginzberg, G.V.Meledin andV.G.Serbo, Phys.Rep. 15 (1975) 181
27. J. H. Field, Nuclear Physics B168 (1980) 477-494
28. Review of Particle Properties 10 April 1986, Particle Data Group Physics Letters ISSN 0370-2693 Volume 170B, pylba 170,1-350
29. MARK II Collab., G.S. Abrams et al., Phys. Rev. Lett. 43 (1979) 477; MARK II Collab., P. Jenni et al., Phys. Rev. D27 (1983) 1031.
30. JADE Collab., W. Bartel et al., Phys. Lett. B113 (1982) 190.
31. CELLO Collab., H.J. Behrend et al., Phys. Lett. B114 (1982)378; B125 (1983) 518(E).
32. PLUTO Collab., Ch. Berger et al., Phys. Lett. B142 (1984) 125.

33. TASSO Collab., M. Althoff et al., Phys. Lett. B147 (1984) 487.
34. A Measurement of the η Radiative Width $\Gamma_{\eta\to\gamma\gamma}$, JADE collaboration (W. Bartel, et al.),Phys Letters 160B (1985)421
35. Recent Results From the Crystal Ball Experiment, Stephen T. Lowe, Proceedings of the SLAC Summer Institute on Particle Physics, July 28-Aug 8, 1986
36. TPC/2γ Collab., H. Aihara et al., Phys. Rev. D35 (1987)2650
37. Measurement of $\eta' \to \pi^+\pi^-\gamma$ in Collisions. ARGUS Collaboration (H. Albrecht, et al.), Phys. Lett. 199B:457,1987 .
38. Measurement of the properties of the η' and search for other resonances in $\gamma\gamma \to \eta\pi^0\pi^0$, Crystal Ball Collaboration (D. Antreasyan, et al.) Phys.Rev.D36:2633,1987.
39. Crystal Ball Collaboration, C. Edwards et al., Phys. Lett. 110b, 82 (1982)
40. CELLO Collaboration, H. J. Behrend etal., Phys. Lett. **114B,** 378 (1982); **125B,** 518(E) (1983)
41. J. E. Olsson (JADE Collaboration), in Photo *Photon Photon Collisions,* Proceedings of the Fifth International Workshop on Photon Photon Collisions, Aachen, 1983, edited by C. Berger (Lecture Notes in Physics, Vol. 191) (Springer, Berlin, 1983), p. 45
42. **PLUTO** Collaboration, Ch. Berger et al., Phys. Lett. **149B,** 427 (1984).
43. Crystal Ball Collaboration, D. Antreasyan et al., Phys. Rev. D33: 1847 (1986).
44. **TASSO** Collaboration, M. Althoff et al., Z. Phys. C - Particles and Fields 31,537-543 (1986)
45. **TCP/2γ** Collaboration, A Measurement of $a_2^0(1320)$ Formation in Photon-Photon Collisions, H. Aihara et al., Submitted to 1987 International Europhysics Conference on High Energy Physics, Session P14
46. Review of Particle Properties 10 April 1986, Particle Data Group Physics Letters ISSN 0370-2693 Volume 170B, pylba 170,1-350
47. Reviews of Particle Properties, Particle Data Group, December 1988 (no yet

published)

LAWRENCE BERKELEY LABORATORY
TECHNICAL INFORMATION DEPARTMENT
1 CYCLOTRON ROAD
BERKELEY, CALIFORNIA 94720